Western Australian School of Mines (WASM): Minerals, Energy and Chemical Engineering

3D Analytical/Numerical Simulations of Reservoirs Considering Poroelasticity

Hossein Salemi

0000-0003-2347-4308

**This thesis is presented for the Degree of
Doctor of Philosophy
of
Curtin University**

April 2021

Declaration

To the best of my knowledge and belief, this thesis contains no material previously published by any other person except where due acknowledgement has been made.

This thesis contains no material which has been accepted for the award of any other degree or diploma in any university.

Signature:

April 2021

Abstract

Geotechnical and geomechanical investigation in the current fast developing era is very vital and challenging in oil and gas development strategies. Within the petroleum sector, this particular investigation has become more important in terms of various environmental issues such as compaction, subsidence, fault reactivation. The main parameter that must be deliberately assessed in the geomechanical analysis is the pore pressure changes as a result of stress changes along with their associated effects on the petroleum and geological related properties of the reservoir formations within hydrocarbon reservoir. The accurate assessment of these changes is one of the key elements for environmentally safe carbon dioxide storage applications. This analysis is mainly performed via developing three-dimensional (3D) analytical and numerical solutions, to determine these aspects within the large-scale reservoir. To be able to address the fluid pressure and different types of stress development in the analysis, Terzaghi (1923) presented the idea of 'poroelasticity' and a few years later was industrialized by Biot (1941) for heterogeneousness and complicated reservoir shape and complex boundary condition. A substantial objective of this thesis is to assess the influence of poroelasticity theory throughout the reservoir formation and the faults as a result of carbon dioxide injection, considering the parameters affecting pore pressure and stress coupling magnitude such as Biot's coefficient. This is performed via analytical and numerical calculations considering reservoir geometry and pore pressure and stress propagation within reservoir layers.

In this study, an extensive overview is presented on the origin of poroelasticity; also, an attempt is made to measure pore pressure and stress evolution and coupling ratio along with the fault stabilities using the real reservoir case study. Additionally, the study details a numerical simulation investigation that was performed to evaluate the coupling of fluid pressure with effective stresses in a real reservoir base, along with analytical validation. In the first case study, the impact of pore pressure variation on normal stress regime has been discussed for a periodical carbon dioxide injection project in the Bergermeer gas field. The results of this study presented well arrangements that match the results provided from the prior analytical studies and numerical researches. In the second case study, a similar approach was made together with a 3D numerical attempt to assess and calculate the pore pressure and stress evolution for a long-term continuous carbon dioxide injection in the Harvey area located in Western Australia. The results of the numerical investigation verify that the target reservoir has the potential for carbon sequestration application.

During the analysis, it is found that Biot's coefficient is a significant element in fluid pressure and stress coupling calculation and also that the precise evolution estimation in regards to the stress and fluid pressure depends mainly on both; the time and the distance to the origin of injection. Inaccurate calculation of the stress and pore pressure in poroelastic modelling occurs due to assuming and including the unity number of Biot's coefficient into the analysis. Besides, the strength of the coupling ratio is determined to be insensitive to variations in Biot's coefficient too, while a lower coupling ratio is detected under a reduced degree of coupling. Therefore, the main focus of this work is on the laboratory approaches to accurately determining the Biot's coefficient.

Among all the existing techniques in the oil and gas industry, the constant volumetric strain methodology has been selected to test the core samples taken from Gosford Quarry, NSW in Australia. The results match well with relevant laboratory test carried out by other researchers. Additionally, the new dynamic technique based on acoustic measurements is introduced along with a unique micro-CT methodology to simplify the complex laboratory setting. The proposed X-ray micro-CT technique shows promising results in the estimation of Biot's coefficient. Most importantly this method is capable of mapping the anisotropy of the Biot coefficient in three dimensions.

Acknowledgements

I am thankful for the contribution and support made by my supervisors Mohammad Sarmadivaleh, Stefan Iglauer, Alireza Rezagholilou, and the discipline of Petroleum Engineering at Curtin University.

I would like to acknowledge contributions to the South-West Hub Flagship project by the Western Australian Department of Mines, Industry Regulation and Safety, the Western Australian Royalty for Regions Program, and the Commonwealth Department Industry and Science.

I also would like to acknowledge the contribution made by the National Geosequestration Laboratory (NGL) to the progress of this research work and for providing access to the X-ray microscope VersaXRM-500 (XRadia-Zeiss Ltd). Some of the analyses and measurements performed in this work were carried out using the laboratory facility housed within the NGL in CSIRO (ARRC building) in Perth, Western Australia.

Part of this work is also was supported by resources provided by the Pawsey Supercomputing Centre with funding from the Australian Government and the Government of Western Australia.

Table of contents

List of figures

List of tables

Nomenclature

α	Biot's effective stress coefficient	κ	Logarithmic bulk modulus
r	Distance (m)	λ	First Lamé parameter (MPa)
q	Fluid volume per unit area and time (m/s)	λ_u	Undrained first Lamé parameter (MPa)
B	Skempton's coefficient	μ	Second Lamé parameter (MPa)
c	Diffusivity (m^2/s)	ν	Poisson's ratio
k	Permeability (m^2)	r	Resultant applied force
t	Time (s)	τ	Resultant applied torque
C	Cohesion (Pa)	ρ	Density
E	Young's modulus (MPa)	t	Applied traction
G	Shear modulus (MPa)	B	Body of element
Kd	Drained bulk modulus (Pa)	r_s	Resultant forces of solid
Kf	Fluid bulk modulus (MPa)	r_f	Resultant forces of fluid
Kg	Grain bulk modulus (MPa)	r_B	Resultant body force
Ku	Undrained bulk modulus (MPa)	Ωt	The surface of the element
Pp	Pore pressure (MPa)	UCS	Uniaxial compressive strength
ρf	Fluid mass density (kg/m3)	Ax	Area of the element
fρ	Fluid mass density (kg/m3)	Vx	Volume of the element
ρS	Solid mass density (MPa) kg/m3)	S	Cauchy stress
τ	Shear stress (Pa)	N	Unit length for the direction vector
ϕ	Porosity	X	Deformation Gradient
Φ	Fluid mass per time (kg/s)	P_f	Fluid pressure
η	Viscosity (Pa·s)	I	Identity matrix
σ_1	Maximum principal stress (MPa)	A_B	Total area
σ_2	Intermediate principal stress (MPa)	As	Grains contact surface areas
σ_3	Minimum principal stress (MPa)	S'	Cauchy effective stress
σh	Minimum horizontal stress (MPa)]	A_C	Cross-sectional area
σH	Maximum horizontal stress (MPa)	L_C	Cross-sectional length
σV	Vertical stress (MPa)	LB	Bounding length
σn	Normal stress (MPa)	$\Delta\varepsilon$v	Volumetric strain variation
δij	Kronecker delta	Pc	Confinement stress
ε	Strain	ϵa	Axial strain
ζ	Increment of fluid content	ϵL	Lateral strain

Chapter 1

1. Poroelastic contribution to the reservoir

1.1 Introduction

This chapter looks at the origin and the importance of poroelasticity during continues gas injection and explores the impact of the coupling ratio on a reservoir rock formation. The main objective of this work includes an assessment of the fault reactivation process as a result of carbon dioxide injection into various stress regimes. This is assessed based on the location and distance to the origin of injection are also taken to account to better assess the failure criteria. The chapter concludes by analytically applying the coupling impact into a real reservoir setting.

Many petroleum-related operations such as reservoir stimulation or carbon storage applications involve injecting fluid and gases into different types of geological formations which cause reservoir pore pressure changes within the boundary of the reservoir and its surroundings (Zoback, 2010). Reservoir fluid pressure increases rapidly near the injection origin and gradually declines while the distance from sources is increasing. Increase pore pressure might cause faults and wellbore instabilities as well as fault reactivation. Besides, target reservoirs and their vicinity might experience expansion during injection, which could damage the deposition of seal rocks. Altering the integrity of the reservoirs and in situ stresses results in fault reactivation in the surroundings. Therefore, a proper injection process demands a correct assessment of stresses and pore pressure evolution within geological formations.

One dimension (1D) poroelasticity philosophy was first presented by Terzaghi (1923) and then advanced by Biot (1941) who considered the coupling interaction of fluid and solid within rock mechanics during the consolidation process. Later, Geertsma (1957) applied the poroelasticity theory to evaluate the environmental/geomechanical responses of reservoirs during oil and gas production. The poroelastic coupling during hydrocarbon extraction and fluid injection from and into the reservoirs considering their impact on the variation of the state of stress and fluid pressure has been addressed by various authors (Cheng et al., 1993; Detournay & Alexander, 1993; Engelder & Fischer, 1994; Rice & Cleary, 1976; Risnes et al., 1982; Ruistuen et al., 1999; Yin et al., 2009).

In this section, a brief overview is given in regards to the important parameters of poroelasticity and tends to assess the poroelastic behaviour of homogeneous hydrocarbon reservoirs during continuous gas injection. The first objective of this work is to evaluate the failure criterion as a result of carbon dioxide injection into a normal stressing regime. The location and distance to the source of injection are also taken to account to better assess the failure criteria.

1.1.1 Stress and strain analysis

Since the 1980s, when oil and gas production emerged as a major requirement in energy sectors, the impact of geomechanical response of the reservoir formations has become an important environmental issue. This is due to the challenging location of the hydrocarbon reservoirs within the underground layers. For this reason, this study focuses on stress, which is fundamental within rock mechanics applications. Due to its importance to this work, this chapter considers this parameter and related parameters such as shear stress, minimum, maximum horizontal stress, pore pressure, and effective stress. Applied force on a solid material causes complex mechanical resistances (stress) with no sensible acceleration.

Within layers of earth, applied forces are divided into weight overlying force and surface force. These forces generate two stress components called shear and normal stress. The stress magnitude within the earth layers is tensor representative, which defines how at a certain point the density of load applies on its surface. As seen in Figure 1, in three-dimensional (3D) studies, the stress is detailed with nine components, where three of them are normal stresses and applying on the surface, and the rest of them are parallel to the surface and called shear stress (Schön, 2011). Considering an extremely small volume of solid material, all the applied stresses (shear and normal) define the state of stress at this tiny volume. For a 3D coordinate arrangement with three axes s, the state of stress is typically represented mathematically as a stress tensor. Using subscripts of "i" (the surface that stress is being applied) and "j" (the direction that stress is being applied), when "i" is equal to "j" the stress is known as normal and shear when "i" and "j" are unequal. The stress tensors can be displayed in the 3D matrix form as:

$$\sigma_{ij} = \begin{bmatrix} \sigma_{xx} & \sigma_{xy} & \sigma_{xz} \\ \sigma_{xy} & \sigma_{yy} & \sigma_{yz} \\ \sigma_{zx} & \sigma_{zy} & \sigma_{zz} \end{bmatrix}$$

Rock stresses are categorized into two core areas, being induced and in-situ stresses. Induced stresses occur as a result of mining, drilling, injection, and excavation activities. In contrast, in situ stresses are existing stresses within the rocks and reservoir boundaries where external forces could activate them. Gravitational stresses or vertical load, tectonic stresses are the main in situ stress categories (Hoek & Brown, 2019). In situ stresses are normally applied vertically (one component) and horizontally (two components). With the increase in depth, the vertical load (σv) increases. In general, the vertical stress (σV) is calculated by multiplying the bulk density (ρ) of the above formations, height (H) from the surface and gravity (g) (Yu, 2000). The estimation of horizontal stress magnitude is customarily determined as a percentage of the vertical stress (Amadei, 2013).

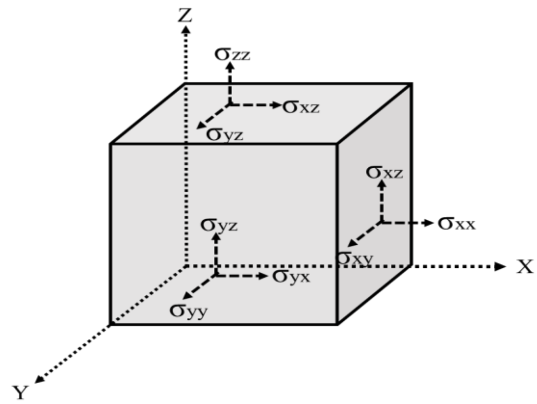

Figure 1: 3D schematic view of all stress components.

According to Ljunggren et al. (2003) in real life, there are many ways to measure stresses via two key categories Firstly, is to study rock behaviour via acoustic methods, database, strain recovery methods and some other methods, which do not require any physical activities in the ground. The second is to disturb the rock formations by applying hydraulic methods and mini fracture operation. Assuming a small cube at any depth, which has stresses that could be normal to each surface, and considering the strain along any axis (Figure 1). Applying force from any surface causes normal stress in that direction as well as strain in all directions. Using Hooke’s law, strain from each direction could be as:

$$\mathcal{E}_V = \frac{\sigma_V}{E} - \upsilon\frac{\sigma_H}{E} - \upsilon\frac{\sigma_h}{E}$$

$$\mathcal{E}_H = \frac{\sigma_H}{E} - \upsilon\frac{\sigma_V}{E} - \upsilon\frac{\sigma_h}{E}$$

$$\mathcal{E}_h = \frac{\sigma_h}{E} - \upsilon\frac{\sigma_V}{E} - \upsilon\frac{\sigma_H}{E}$$

The term 'υ' denotes Poisson's ratio, 'σ' denotes stress, 'E' denotes Young moduli of rock and 'ε' denotes the strain.

Now if we assume that the value of σH *and* σh are equal and assuming no horizontal deformation (imagining that the rock is restrained by other earth materials in the ground), the horizontal stress is calculated as; $\sigma_H = \upsilon / [(1-\upsilon)\ \sigma_V]$, Therefore, the relationship between horizontal and vertical stress mainly depends on Poisson's ratio.

1.1.2 Tectonic stress regimes

A broad understanding and knowledge about stress regimes are extremely beneficial for geotechnical analysis along with reservoir rock mechanical properties and production/injection strategies (Haimson, 1975). Tectonic regimes are mainly characterized by the status of the faults and the 3 main stresses.

A fault is defined as a brittle shear fracture that has a narrow layer where one side of it has been relatively moved to the other side in a different direction parallel to the surface. Principally, a fault is a shear fracture that displaces or extends on a large scale, and if it is small a few centimetres are called shear fractures. To measure the displacement of faults, the direction and stress magnitudes need to be identified.

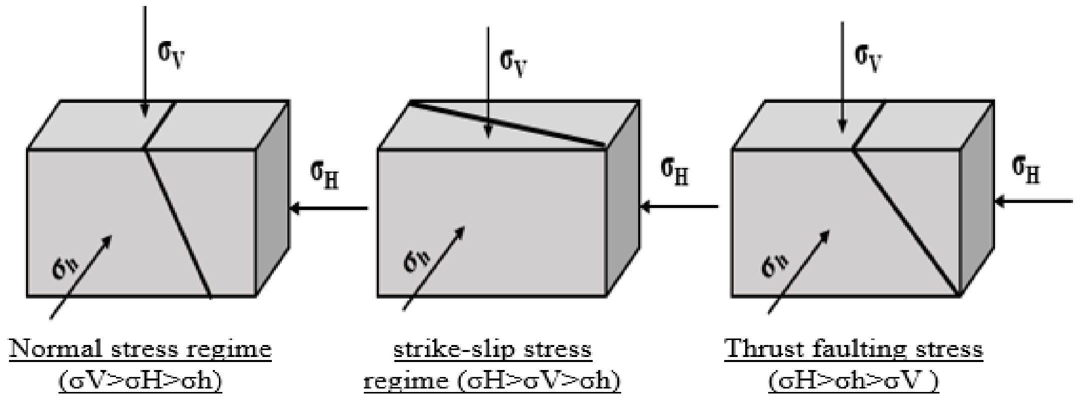

Figure 2: The principal stresses status for various tectonic regimes (Scholz, 2019).

Characterization of stress regimes can be performed by the strength and the size of principal stresses (σV, σH, σh). Figure 2 shows the arrangements of principal stresses for various tectonic regimes. Generally, a fault's strength is determined by the degree of friction factor. For instance, the friction coefficient of the strong fault is normally in the range of 0.6 to 0.8. The weakness (instability) and reactivation of faults is the most important concern in geomechanics studies.

1.1.3 Mohr principle

The Mohr failure principle is a mathematical tool to demonstrate the brittleness of rocks to normal principal stresses and shear stress (Kaliakin, 2017; Labuz & Zang, 2012). The Mohr circle demonstrates shear and normal stresses on a failure envelope (Figure 3). Initially, Mohr developed a linear equation to show how shear failure occurs due to shear stress on a failure plane. The Mohr failure principle graphically shows the variation of principal effective stresses against shear stress. According to the linear formula that shear stress is equal to added to mean stress. cohesion added to mean stress. The diameter of the Mohr circle will change with the change of principal stresses which cause shear stress variation. Therefore, any changes to the Mohr diagram indicate how close the rock is to failure.

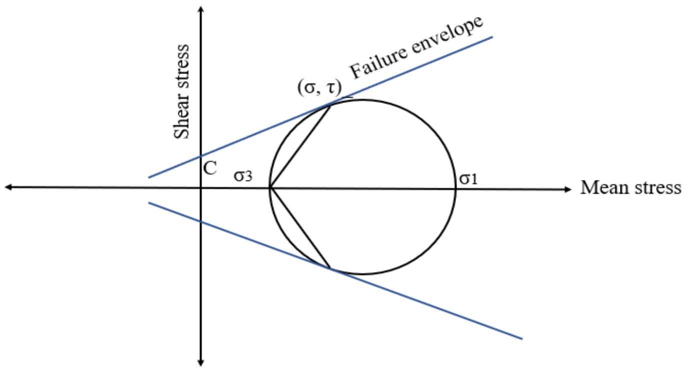

Figure 3: Schematic view of the Mohr diagram (Labuz & Zang, 2012).

1.2 Effective stress

The main difference between rock and soil is the particle size and the orientation of grain joints. The stability of the rock frame depends mainly on which way pore pressure acts within the pores and grain's contact points. In rock mechanic analysis and stress analysis, it is always assumed that fluid pressure acts throughout the rock in a similar way to the soil, which ignores the nature of effective stress. Therefore, these incorrect assumptions can end up in misleading stress analysis, especially in numerical modelling.

Interference caused by pore pressure acts mainly on rocks frame and total in-situ hydrostatic stresses. Total stress is the only parameter that could be altered by fluid pressure variations, not shear stress. Considering Terzaghi (1943) theory, effective normal stress is the difference between mean normal stress and existing fluid pressure within grains. The effective normal stress is mainly the applied load per unit area being transferred by solid particles that control the rocks' strength and their volume (Aadnøy & Looyeh, 2011).

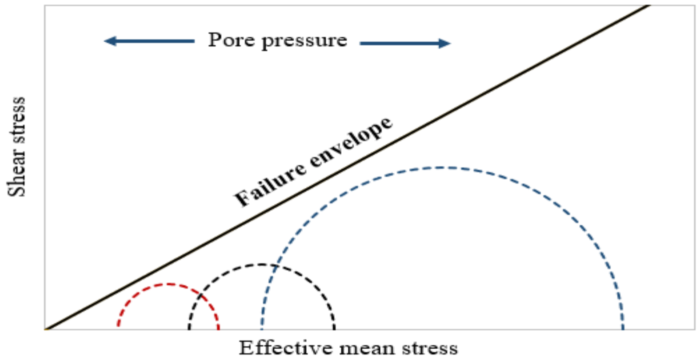

Figure 4: The effect of pore pressure in Mohr circle.

For instance, due to fluid pressure dropdown, the effective normal stress becomes stronger as the grain's connectivity becomes less within the soil or rock skeleton. Consequently, the differential stress (mean stress) remains unchanged due to the effect of fluid pressure on the principal stresses from three directions except for shear stress. In other words, effective stresses vary due to pore pressure variations. In hydrocarbon production when the fluid pressure decreases the effective normal stress becomes lower than its initial value. Mohr's diagram clearly shows these changes. As shown in Figure 4, the movement of circles verifies the effect of fluid pressure on the stress condition and whether it reaches the failure envelope. Generally, the theory of effective stress helps one to identify the rock failure behaviour during injection/production. Inside the geological structures, the effective stress law is shown in equation 1. Principally as it is shown in Figure 5, the normal effective stress (σ') is the pore pressure (*Pp*) value subtracted from principle stresses (σ) in any direction (Biot, 1941).

$$\sigma' = \sigma - \alpha . Pp \tag{1}$$

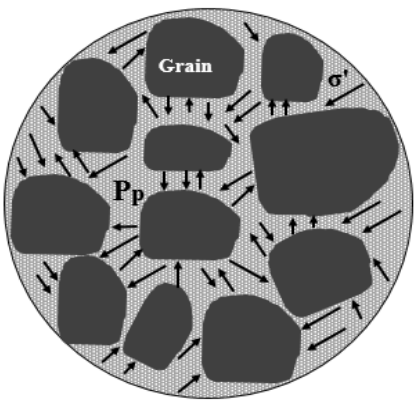

Figure 5: Schematic view of fluid pressure (Pp) and effective normal stress (σ') within the rock's grains.

Note that, Biot's coefficient, which will be fully discussed later in chapter 3 and chapter 4. Additionally, near the borehole, the effective stress is defined under three components, which are radial, tangential, and vertical stress.

1.3 Poroelasticity

1.3.1 Background

Inimitably Terzaghi (1923) developed the one-dimensional (1D) soil consolidation model when it is under influence of fluid pressure. Biot (1941) later developed Terzaghi's model to the three-dimensional (3D) theory of poroelasticity considering the effectiveness of the rock's anisotropy and introduced linear constitutive formulation. Rock's anisotropy in rock mechanical applications is extremely important. Factually, significant stress and deformation analysis error could occur when one assumes anisotropic rocks to be isotropic and vice versa (Barla, 1972). Mcnamee and Gibson (1960) continued Biot's work by applying the effect of the Poisson's ratio and bulk modulus of the rocks including both drained and undrained conditions into their analysis.

Poroelasticity is a measure that shows how the porous rock deforms while its body is under the effect of fluid movement and external forces as stated by Rice and Cleary (1976). Applied stresses to a porous rock directly affect the pores and how the fluid in it tends to move. Therefore, the solid material deforms elastically. To model poroelasticity in any real application, two main aspects must be addressed, Darcy's law and the displacement theory of porous materials represented by Biot (1941). Darcy's law mainly expresses how fluid motion and applied pressure interact within a porous rock for a certain distance and fluid viscosity. Porous rock deformation is a significant aspect in identifying various environmental and petrophysical issues within the earth layers and in petroleum science such as estimating hydrocarbon productivity and forecasting surface compaction and subsidence during oil and gas production and any other injection applications. Deformation analysis is another important factor in the estimation of rocks failure such as tectonic movements in the region where induced pressure exists. The importance of Porous rock deformation was first addressed by Biot (1941) and later developed by Kümpel (1991). According to their achievements, fluid pressure is the main reason for the changes in minimum horizontal stress (σh) where they describe how rocks deform when their porous media is occupied with fluid while under pressure. The variation of σh under the influence of Pp represents the poroelastic behaviour of rocks, or poroelasticity (Wang, 2000). In other words, fluid pressure changes have a big impact on the state of stress.

Ignorance of this phenomenon endangers oil and gas projects with an explosion in wells, landslides and seismic activities.

1.3.2 Coupling behaviour of rocks

During injection/depletion, reservoirs encounter pore pressure changes together with in situ stress changes, and it is known as coupling. The term coupling ratio here corresponds to the ratio of σh change to the Pp change (Zoback & Zinke, 2002). Knowledge of this phenomenon is extremely important and has been identified in terms of, hydraulic fracturing, compaction, surface subsidence, and so on. Additionally, formation pressure changes during production and injection could cause wellbore instability as well as fault reactivations. Therefore, knowing the coupling effect and the variation of in situ effective stress is very important before any field developments. Applying poroelastic theory and analytical solutions in the early stages of any field investigation and field development is a very cost-effective and risk-free procedure (Laurent et al., 1993).

Induced seismicity in many different industries has been an advanced issue in the last few years (Foulger et al., 2018). As stated by Zoback and Gorelick (2012), hydrocarbon production, injection of carbon dioxide (sequestration), hydraulic fracturing and wastewater injection are the main reasons behind induced seismicity. The most recent induced earthquake (5.4 magnitudes) occurred in South Korea as a result of incorrect fluid injection plans and ignorance of accurate implementation of coupling ratio into their risk analysis (Kim et al., 2018). Relatively, a decrease in reservoir fluid pressure as a result of production is the primary mechanism accountable for the unexpected slip on the faults within reservoir boundaries and earthquakes (Suckale, 2009). The induced poroelastic stressing due to hydrocarbon production might also cause earthquakes outside of reservoir boundaries (Segall, 1989). The large degree of coupling could cause reservoir rock volumetric, lateral and radial strain changes and associated effective normal stress variation within the production field. Reservoir rock poroelastic and elastic parameters are the key factors affecting the status of fluid pressure and resultant coupling magnitude. The reservoir geometric characteristics and type of injection/production wells are also important aspects to be considered when assessing rock stability. As stated by Josh et al. (2012) due to the complex geometry of hydrocarbon reservoirs and the stresses faulting regimes, the coupling analysis needs more and broad investigation to be validated. Nevertheless, they are important when assessing the integrity of caprock and predicting the fault reactivation risks (Ruistuen et al., 1999).

Biot's linear expression was restated by Rice and Cleary (1976) and the Biot's coefficient was replaced via elastic factors such as Poisson's ratio and bulk modulus. This investigation was carried out under undrained and drained test settings. In the meantime, many researchers endeavoured to solve geomechanical complications such as disorientation and displacement of faults and unexpectedly forced cavities (cylindrical and spherical) via the implication of the poroelastic consolidation theory introduced by Biot. Consequently, applying Biot's approach and the poroelastic behaviour of rocks has been employed extensively to analyse the consolidation of the poroelastic medium. The evolution of coupling ratio during hydrocarbon production was studied by Bell and Nur (1978) where they presented how different types of faults respond when pore pressure and stresses are subjected to any change within reservoir rocks and porous medium. Applying the pore pressure/stress coupling methodology, Booker and Randolph (1984) studied the effect of vertical stress on the coupling ratio numerically. They stated that the rock's deformation as a result of vertical stress mainly depends on time.

Rudnicki (1986) derived spatiotemporal coupling changes in the event of fluid injection into the boundless consistent poroelastic medium. His derivations led to the determination of location and time-dependent coupling ratio. However, his analytical approach is restricted to infinite homogenous porous media. Applying Rudnicki's approach, Tarn and Lu (1991) proposed a systematic solution for the longer consolidation process along with identifying the coupling ratio evolution during hydrocarbon production. Note that in their investigation it was assumed anisotropy of permeability and Biot's coefficient. Engelder and Fischer (1994) also derived analytical expressions showing the relation between the effects of pore pressure changes on minimum horizontal stress assuming that there is no influence on vertical stress during reservoir depletion. Teufel et al. (1991) carried out a wide analysis of several fields in the U.S by providing data in regards to the coupling ratios of abandoned hydrocarbon fields. For instance, they calculated a coupling ratio of 0.57 for the Travis Peak formation in East Texas and 0.48 for the Vicksburg formation in South Texas. According to their observation through various reservoirs, during reservoir depletion with a decrease in fluid pressure, effective normal stress increases linearly. Addis (1997) offered 3D analytical solutions of the coupling response of the reservoir for the longer consolidation time for various hydrocarbon production fields. His coupling response to depletion was based on equation 2. Where the coupling ratio significantly affected by the poison's ratio (υ) and Biot's coefficient (α).

$$\frac{\Delta\sigma_h}{\Delta P_p} = \alpha \frac{1-2\upsilon}{1-\upsilon} \tag{2}$$

1.3.3 Analytical approach to stress/pore pressure coupling

For an environmentally safe injection operation, it is highly important to assess reservoir stress variation due to pore pressure variation and calculate the geomechanical related fault and well instability in the target basin foundation. The stress variation could potentially reactivate the existing faults within the geological formations (Soltanzadeh & Hawkes, 2008). Biot's diffusivity method is expressed with either analytical or numerical solutions for poroelasticity investigations. Applying the poroelasticity theory to rock mechanics, Geertsma (1957) originally derived a systematic approach to show the coupling process to petroleum-related production and injection. Rice and Cleary (1976) took this further and developed the basic methodology for stress measurements for various shape (e.g., cylindrical) cavities for fluid-filled rocks. Rudnicki (1986) reworked the earlier governing calculations considering the point loads in the circular medium under the assumption of plane strain. His approach mainly proposed how the radial and tangential stress evolution occurs due to fluid pressure changes. Including the period of injection and intervals into the governing equation, Detournay and Cheng (1988) managed to calculate coupling magnitude. They also added the compressibility of fluid and rock to their analysis.

Defining rock as a porous media filled and saturated with brine, Risnes et al. (1982) proposed a methodology to solve governing equations for tangential and radial stresses around the wellbore. Their proposed analytical solution provided a complete set of coupled poroelastic impact around the borehole to assess instability and predict fault reactivation inside the reservoir formation. Similarly, Han and Dusseault (2003) proposed a 2D analytical solution, taking into account the effect of porosity and permeability into poroelastic medium and discovered they have no significant impact on pore pressure changes.

Zoback and Zinke (2002) have carried out an extensive investigation and derived an analytical and numerical approach to the coupling behaviour of rocks. They cited that in the case that pore pressure decreases, maximum horizontal stress declines when poroelasticity is included in the assessment. Moreover, within a normal fault and stress regime, σh varies twice as higher as the Pp causing the instability of the existing faults with the normal friction coefficient. Goulty (2003) introduced various methodologies that deliver coupling strength applying the governing diffusivity expressions to monitor and minimize the risks related to reservoir compaction. Using Mohr criteria, he linked the reservoir coupling ratio with the standard coefficient of friction to the variation of pore pressure.

Coupling studies mainly assists researchers in finding suitable target reservoirs for carbon dioxide injection applications. Where reservoirs with a higher magnitude of the coupling ratio benefit from stronger and more stable faults (Rutqvist et al., 2016). In the case of carbon dioxide injection, more criteria are affecting the firmness of faults. One such parameter is temperature, as stated by Grigoli et al. (2018), based on their investigation of the magnitude 5 earthquake that occurred in South Korea due to carbon dioxide sequestration activities.

In this chapter, the combination of Wang (2000) and Rudnicki's (1986) methodologies are applied to analyse the coupling strength around the injection wellbore. Note that this model is applicable for fault stability analysis. This will show how *Pp* and other principal stresses vary when the distance and direction from injection origin are taken into calculations. This method is applied to the Bergermeer gas storage field in the Netherlands. A complex numerical investigation has been already carried out by Orlic and Wassing (2012) to monitor the impact of different productivity and injectivity rate on the stability of the main faults. The approach to analytically determine coupling magnitude has been extensively reported in the literature (Atefi Monfared, 2015; Detournay & Cheng, 1988; Fjær et al., 2008; Hillis, 2000; Segall, 1989; Teufel et al., 1991; Wang, 2000; Zoback, 2010).

Rudnicki's and Wang's approaches are briefly highlighted here to demonstrate the alterations in the *σh* along with *Pp*. The analytical investigation primarily originates from the Beltrami and Michell expression as shown in equation 3 and *Pp*-induced stress approach as shown in equation 4 as it was proposed by Wang (2000);

$$\nabla^2\sigma_{ij} + \frac{1}{1+\upsilon}\frac{\partial^2\sigma_{kk}}{\partial x_i \partial x_j} + \alpha\left(\frac{1-2\upsilon}{(1-2\upsilon}\right)\left[\frac{1-\upsilon}{1+\upsilon}\frac{\partial^2 P}{\partial x_i \partial x_j} + \delta_{ij}\nabla^2 P\right] = \frac{-1}{1-\upsilon}\delta_{ij}\vec{\nabla}.\vec{F} - \frac{\partial F_i}{\partial x_i} - \frac{\partial F_j}{\partial x_i} \qquad (3)$$

$$Q = \frac{1}{k_d B}\left[\frac{B}{3}\frac{\partial\sigma_{kk}}{\partial t} + \frac{\partial p}{\partial t}\right] - \frac{k}{\mu}\nabla^2 P \qquad (4)$$

The term Q represents the injection rate, the term *Kd* is drained bulk moduli, B is Skempton coefficient, μ is the viscosity, F is applied force, υ denoted the Poisson's ratio, σkk stands for mean stress and α is the Biot's coefficient.

From Darcy's law we know that;

$$\vec{q} = \frac{k}{\mu}\vec{\nabla}\left(P + \rho_f g z\right) \qquad (5)$$

The term k stands for permeability, ρ_f stands for the density of passing fluid, and g represents gravity.

Applying the continuity calculation (equation 6) and the constitutive law (equation 7) solved by Wang (2000) to Darcy's law (equation 5) for the fluid increment content is obtained as shown in equation 8. This is used to solve the stress and *Pp* variation or the poroelastic complexity of the different type of rocks.

$$\frac{\partial \zeta}{\partial t} + \frac{\partial q_x}{\partial x} + \frac{\partial q_y}{\partial y} + \frac{\partial q_z}{\partial z} = Q \tag{6}$$

$$\zeta = \frac{\alpha}{k_d}\frac{\partial \sigma_{kk}}{3} + \frac{\alpha}{k_d\, B} P \tag{7}$$

$$\frac{\partial \zeta}{\partial t} = \frac{k}{\mu\, S}\ \nabla^2 \zeta + \frac{k}{\mu}\ \frac{\lambda_u - \lambda}{\alpha(\lambda_u + 2G)}\ F_{kk} \tag{8}$$

Where the parameter G is the shear modulus, λu represents an undrained lame module, and λ is the drained lame module.

The undrained bulk modulus (*Ku*) is also obtained using equation 9:

$$k_u\ = \lambda_u + \frac{2G}{3} = \left[k_g + k_d\, \varphi\left(\frac{k_g}{k_f}\right) - \varphi - 1\right] / \left[1 - \varphi - \left(\frac{k_d}{k_g}\right) + \varphi\left(\frac{k_g}{k_f}\right)\right] \tag{9}$$

Rudnicki rederived the equation of poroelasticity presented by Biot and proposed the methodology to measure pore pressure and stress evolution attributable to continuous gas and fluid injection. Taking into calculations the diffusivity parameters, Rudnicki also introduced the solutions for pore pressure (equation 10) and stress (equation 11) changes when the duration of injection (t) and the location of injection point (x) are the key elements for the analysis.

$$Pp(X,t) = \frac{q}{4\pi r\, \rho_f\, c}\left[\frac{(\lambda_u - \lambda)(\lambda + 2G)}{\alpha^2(\lambda_u + 2G)}\right] erfc\left(\frac{1}{2}\xi\right) \tag{10}$$

$$\sigma_{ij}\,(X,t) = \frac{-\,q}{\rho_f c}\frac{(\lambda_u - \lambda)G}{4\pi r \alpha(\lambda_u + 2G)}\sigma_{ij}\ \left[\left[erfc\left(\frac{1}{2}\xi\right) - \frac{2}{\zeta^2} g(\xi)\right] + \frac{\chi_i \chi_j}{r^2}\left[erfc\left(\frac{1}{2}\xi\right) + \frac{6}{\xi^2} g(\xi)\right]\right] \tag{11}$$

Where ξ is Boltzmann variable and calculated as; $\zeta = r/(\sqrt{ct})$, c stands for the diffusivity or and is a function of the permeability of the rock as shown in equation 13. Gravity as a function of Boltzman($g(\xi)$) is attained employing equation 12 as per Altmann et al. (2014).

$$g(\xi) = \frac{1}{2\sqrt{\pi}}\int_0^{\xi} s^2\, exp(-\frac{1}{4}\, s^2)ds = erf\left(\frac{1}{2}\xi\right) - \frac{1}{\sqrt{\pi}}\xi\, exp\left(-\frac{1}{4}\xi^2\right) \quad (12)$$

$$c = \left[K(\lambda_u - \lambda)(\lambda + 2\mu)/\right]/[\alpha^2(\lambda_u + 2\mu)] \quad (13)$$

It worth noting that along with the orientation of X in the 3D system, σ_{xx} becomes radial stress and σ_{yy} and σ_{zz} are tangential stresses. Thus, to calculate the radial stress x_ix_j becomes r^2 so the radial stress evolution becomes equation 14 and to calculate the tangential stress x_ix_j becomes zero which results in equation 15.

$$\sigma_{xx}(X,t) = -\frac{4}{\zeta^2}g(\xi) - 2\frac{q}{\rho_f c}\frac{(\lambda_u-\lambda)G}{4\pi r\alpha(\lambda_u+2G)}erfc\left(\frac{1}{2}\xi\right) \quad (14)$$

$$\sigma_{zz}(X,t) = -\frac{2}{\zeta^2}g(\xi) - \frac{q}{\rho_f c}\frac{(\lambda_u-\lambda)G}{4\pi r\alpha(\lambda_u+2G)}erfc\left(\frac{1}{2}\xi\right) \quad (15)$$

Where q stands for the injection rate and λu denotes the undrained Lame parameter.

The equation derived for the stress distribution as shown above (equations 14 and 15) are effective for points when the observation point is considered on the horizontal x-direction with the injection origin in the centre of the coordinate system. Though, considering the point of observation in the orientation of Y, the results for σxx and σyy are differing. Specifically, equation 14 aids to measure the radial stress variation and equation 15 defines the tangential stress changes in the radial direction. Accordingly, the stress changes expressions enable us to identify the stress condition for complex locations at various injection time.

For a very long period of injection, coupling evolution is calculated via equations 11 divided by equation 10 as of equation 16. This expression is used in the case of long-term continuous injection and depletion scenarios.

$$\frac{\Delta\sigma_{ij}(x,t)}{\Delta Pp(x,t)} = \frac{G(\delta_{ij}\left(erfc((0.5\xi)-(2/\xi^2)g(\xi)\right)+{}^{x_ix_j}/_{r^2}\left(erfc(0.5\xi)+\frac{6}{\xi^2}g(\xi)\right)}{(\frac{\lambda+2G}{\alpha})erfc((0.5\xi)} \quad (16)$$

1.4 Case study

The focus of this attempt is to assess the fault stabilities along with monitoring the stresses and pore pressures variation for the Bergermeer field in the Netherlands. The hydrocarbon production started in early 1971 and due to the occurrence of few seismic activities, the production was stopped in late 2010. In order to stop the risks related to seismic events along with supplying enough backpressure to increase production rate, cushion gas injection was injected periodically into the reservoir (seasonal) between 2010 and 2012. From this time onward, the field has a cyclic production plan that has gas production in wintertime and carbon dioxide injection during the less demanding period (Orlic et al., 2013).

This section takes into account the effects of a cushion gas injection with the properties shown in Table 1 (Muntendam-Bos et al., 2008). The appraised variation of stresses and pore pressures are obtained to analyse the stability of the main faults during the injection process. Based on the project's reports carried out by Toksöz (2009), there are seven major faults in the field and the normal stress regime is dominant.

1.4.1 Analytical approach

In this part, the changes in the *Pp* and stresses due to continuous gas injection are calculated based on equations 10, 14, and 15. This assessment is based on the petrophysical and material properties (Table 1) of the field according to Orlic and Wassing (2012). The coupling ratios are measured to monitor their impact on the stability of the field faults for the year 2010. In order to evaluate the coupling impacts, the changes of the *Pp* and stress considering the distance and time from the observation point needed to be monitored.

The observation location is assumed to be 200 m away from the central fault. For calculations, three injection times (one month, three months and six months) are chosen to check the central fault's stability assessments. Table 1, provides the mechanical and material used for the calculations based on equations 14, 15, and 16.

As it was explained in section 1.3, the coupling strength directly affects fault firmness. In a normal regime as has been explained in section 1.1.2, the σV is not affected due to fluid pressure changes, therefore, when fluid pressure increases the effective vertical stress declines. Note that in this type of fault regime the stress changes are measured by the degree of σV and σh.

In the case of depletion, the *Pp* in the direction of σh raises the effective σ*h* by 1/3, because σh is a radial element, in contrast to the σV which is the tangential element and increased by twice as the value of effective σ*h*. Therefore, the reduction in *Pp* results in a rise in differential stress. No significant change occurs along the direction of σH which cause the development of shear stress during depletion. Taking to account the coupling of σh and *Pp*, σh increases when the *Pp* increases. Therefore, the coupling ratio is the main factor affecting minimum effective horizontal stress to decrease not only *Pp*. Thus, effective stress is directly affecting the coupling strength.

Table 1: Analytical approach material and petrophysical properties.

Injection volume (Bm^3)	1.88
No. well	10
Poisson's ratio	0.18
λ (MPa)	3050
α	0.76
E (GPa)	18
λu (MPa)	4290
Distance (m)	200
C (m^2/s)	0.006
Injection rate (Mm^3/day)	10.4
Injection period (months)	6

Bear in mind the coupling response of rocks, when *Pp* changes the effective normal stress changes as is denoted by $\Delta p'_p, \sigma'_{veff}$ *and* $\sigma'_{h,eff}$ which is shown in equations 17 and 18 cited by Altmann (2010).

$$\sigma'_{\mathrm{veff}} = \sigma_{\mathrm{v,eff}} - \Delta \mathrm{p}'_{\mathrm{p}} \tag{17}$$

$$\sigma'_{\mathrm{h,eff}} = \sigma_{\mathrm{h,eff}} + \frac{\Delta\sigma_{\mathrm{h}}}{\Delta \mathrm{p_p}} . \Delta \mathrm{p}'_{\mathrm{p}} - \Delta \mathrm{p}'_{\mathrm{p}} \tag{18}$$

When poroelasticity is not included in the rock stability analysis, the coupling ratio is assumed to be zero which is matching the initial Terzaghi (1943) limit of one-dimensional consolidation theory. For instance, when *Pp* increases (Figure 4), the Mohr circle becomes smaller (red dotted line) which leads to faults stability. In contrast, when *Pp* declines the diameter of the Mohr circle increases and probably touches the failure line which leads to fault instability (blue dotted line). This is because of the decrease in effective σ*h* and an increase in effective σ*V*.

1.4.2 Time-dependant fluid pressure and radial/tangential stress variation

As shown in Figure 6 within 600 m distance from the injection origin, the *Pp* declines more sharply than the radial/tangential stresses. The *Δσr* is similar to the *Pp* variations. Tangential stress change is, though, shows more reduction than the radial stress change and becomes zero beyond 800 m from the injection point. In such circumstance, near to the injection source, tangential stress is small in this instance. The coupling changes (*Δσr/ΔP and Δσt/ΔP*) against distance to the origin of injection is illustrated in Figure 7. After six months of continuous injection, closer to the injection point, coupling ratios for both stresses increases. Likewise, higher the distance from the injection source, both ratios change rapidly, while *Δσr/ΔP* increases (2.2), *Δσt/ΔP* decreases (-0.5).

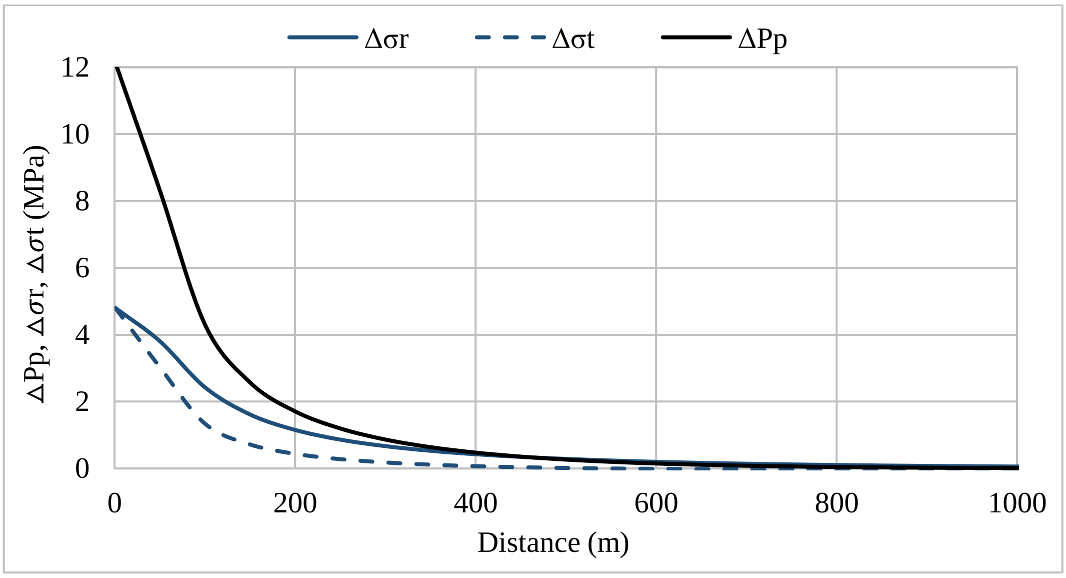

Figure 6: The variation of fluid pressure and radial/tangential stresses during six months of continuous gas injection.

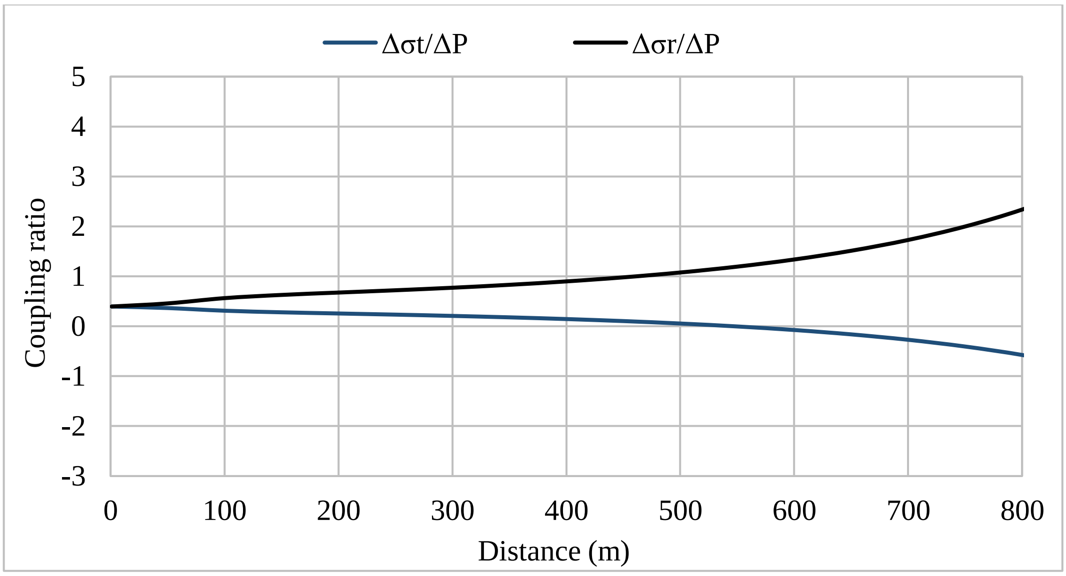

Figure 7: Coupling evolution during six months of continuous gas injection.

1.4.3 Location dependant fluid pressure and radial/tangential stress variations

Figure 8 illustrates temporary variations of *Δσr, Δσt and ΔPp* inside 200 m from the gas injection origin is shown. According to the figure, within the first week of injection both stresses changes instantly and pore pressure remains untouched. This is due to the distribution of stress inside the porous medium when is compared to fluid pressure that shows some inertia prior to dissipating within the porous rock. Additionally, it is observed that the $\Delta\sigma r$ is greater than the $\Delta\sigma t$.

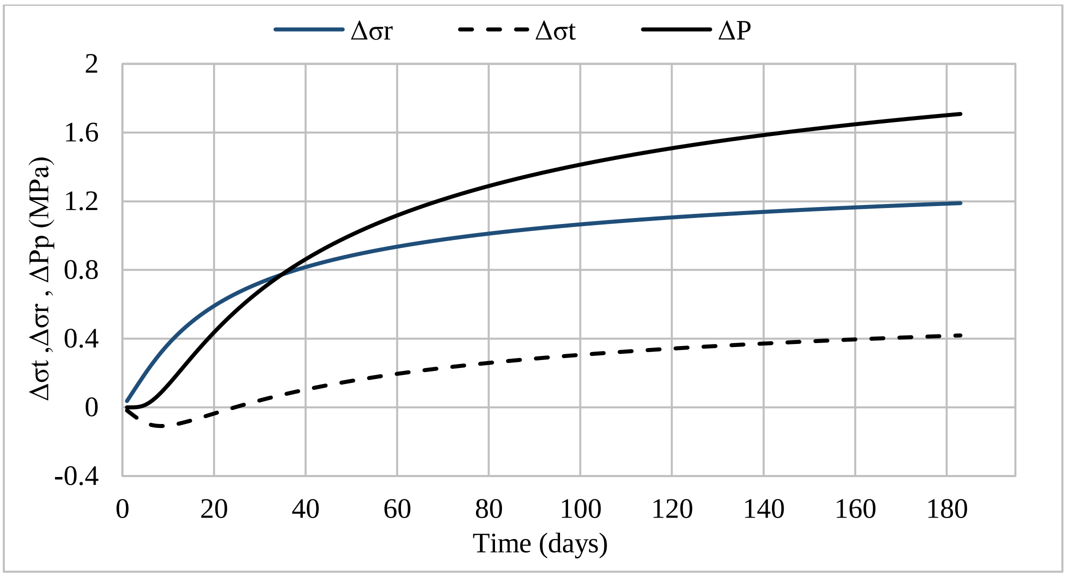

Figure 8: The variation of fluid pressure and radial/tangential stresses for 200 m distance from gas injection origin.

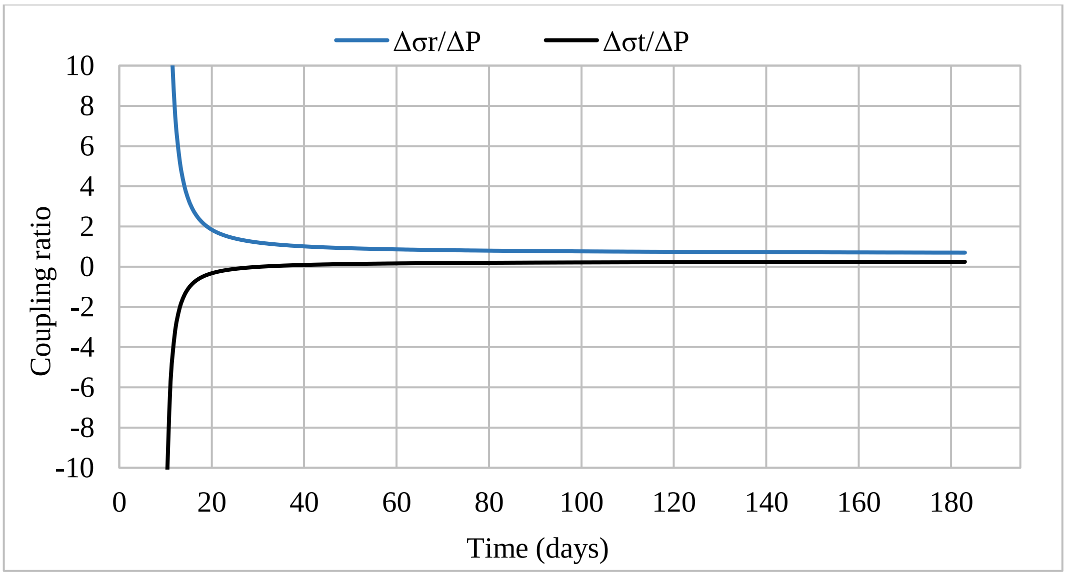

Figure 9: Coupling variation within 200 m from injection source.

Assuming the point of injection within the sphere of 200 m, the coupling ratios are calculated (Figure 9). In either stress conditions, the coupling magnitude tends to rapidly become zero after almost three months from the beginning of the injection.

1.4.4 Fault reactivation analysis

In this section, a precise investigation was carried out on the firmness of the main faults and an attempt was made to determine the geological response of the reservoir rock to the various injection scenarios. Figure 10 demonstrates the position of the central fault (current case) and the location-scale of the observation point which is expected to be in the depth of 2125 m and 200 m away from the central fault. Bear in mind the observation point is to be found inside the reservoir.

Cited by Orlic et al. (2013), to calculate *σh*, the mini fracture technique was performed and the vertical stress was measured by the weight formations above the reservoir. Therefore, at the observation point, *σh* is measured to be 15 MPa acquired from the mini fracture test along with the gradient of force that measured to be 22.6 MPa/km. Besides, the pore pressure was calculated at 13 MPa right before the gas injection commencement. This was calculated having the stress ratio (k) of 0.35 and fluid pressure of 23 MPa measured initially in 1971. As shown in Table 2, the input parameters and pressure values are shown at the beginning of production in 1971 and when the operation was shut down in late 2006.

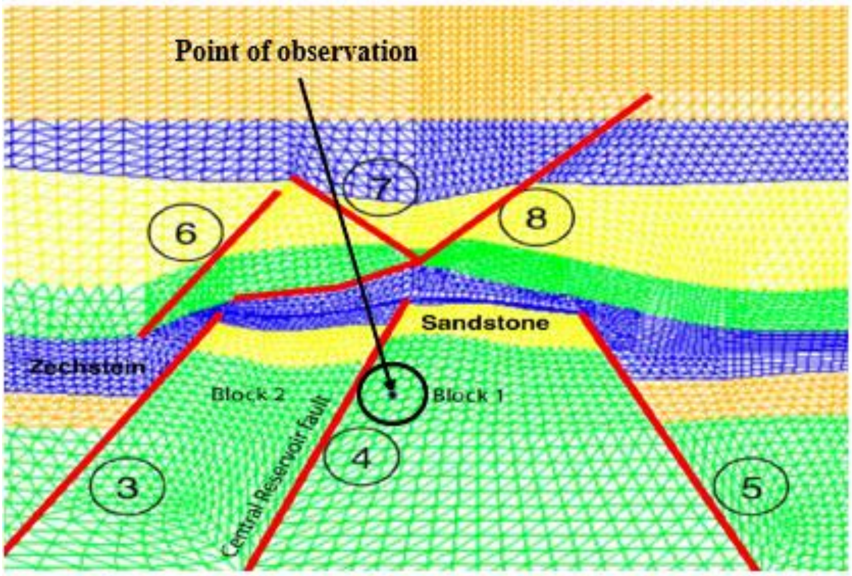

Figure 10: The schematic view of the central reservoir fault as well as the location of other faults (red lines) from the point of observation (Hager & Toksoez, 2009).

Biot's coefficient and other material properties acquired from Table 1 and for the stress analysis in 2006, the coupling ratio is assumed to be 0.77 which is taken from the report prepared by Muntendam-Bos et al. (2008). The fault stability analysis underwent investigations using the Mohr-Coulomb criteria for the cohesionless fault (friction angle of 33°). Following the stability analysis, the impact of coupling now undergoes analysis to evaluate the central fault stability because of seasonal cushion gas injection. This will be achieved by applying two scenarios. Assuming the observation point fixed on the σh-axis (2125 m depth) and 200 m far from the origin of injection, firstly no coupling impact is and secondly the coupling impact included in the calculations.

Table 2: Stress and pore pressure status before and after depletion (1971 and 2006).

Year	1971	2006
σ_V (MPa)	48	48
Effective σ_V (MPa)	25	47
σ_h (MPa)	32	15
Effective σ_h (MPa)	9	14
Pp (MPa)	23	21

Figure 11 shows the original state of stress at the start of the seasonal injection in 2010. Based on equations 14 and 15, the variation of the radial and tangential stresses is measured, and shown in the graph. Table 3 and Figure 11 confirms the effective stress variation after 100 and the end of the injection period (six months). According to the figure, the Mohr diagram shifts toward the Mohr-Coulomb failure line in case of longer injection time. This is because of higher Pp changes than total stresses. The longer injection time might result in reaching the failure envelope and reactivation of the main middle fault.

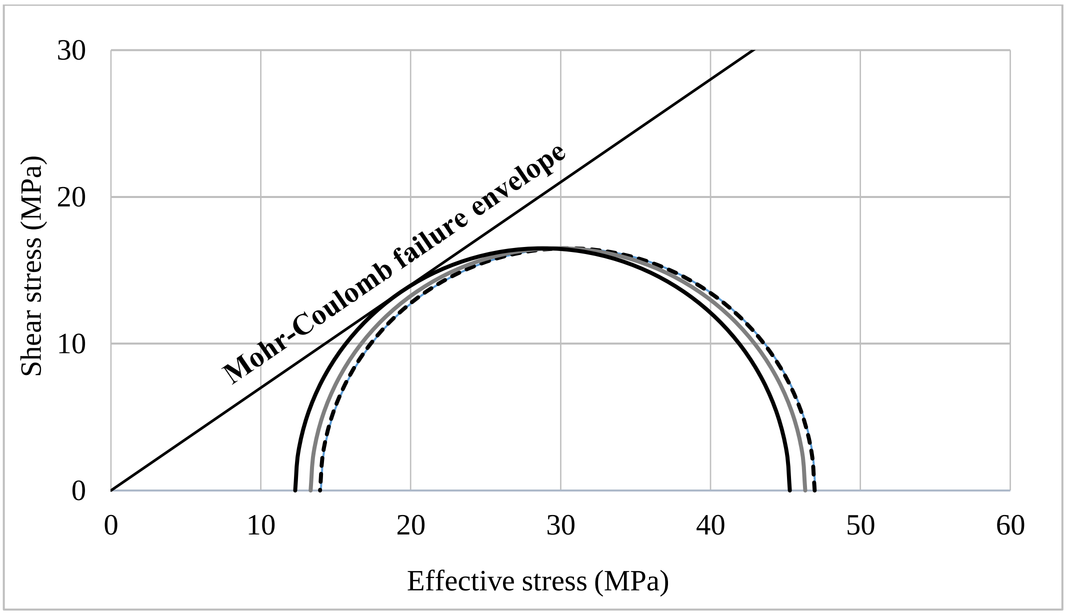

Figure 11: The changes of effective stress considering the effect of coupling (the dashed black line depicts the initial status of effective stress, grey and black lines are showing the effective stress afterwards 100 days and six months of injection, respectively).

Through the inclusion of coupling (poroelasticity) into the analysis, we can accurately monitor the stress variations. Tangential and radial stress changes at various times are calculated as shown in Table 3. Likewise, Figure 12, validates the notable move of the Mohr diagram when the coupling factor is included. As determined earlier, the injection process influences the effective stresses in various ways. Based on equations 14 and 15 outputs, σh is rising more than σV, and thus, effective σV appears to decrease further than effective σh. By itself, injection leads the Mohr diagram to shrink while it shifts toward the failure line.

Table 3: The radial/tangential stress and fluid pressure changes in different injection periods (Salemi et al., 2017).

Period of injection (Days)	**ΔPp (MPa)**	**Δστ (MPa)**	**Δσr (MPa)**
30	0.68	0.04	0.72
100	1.41	0.3	1.065
183	1.7	0.42	1.19

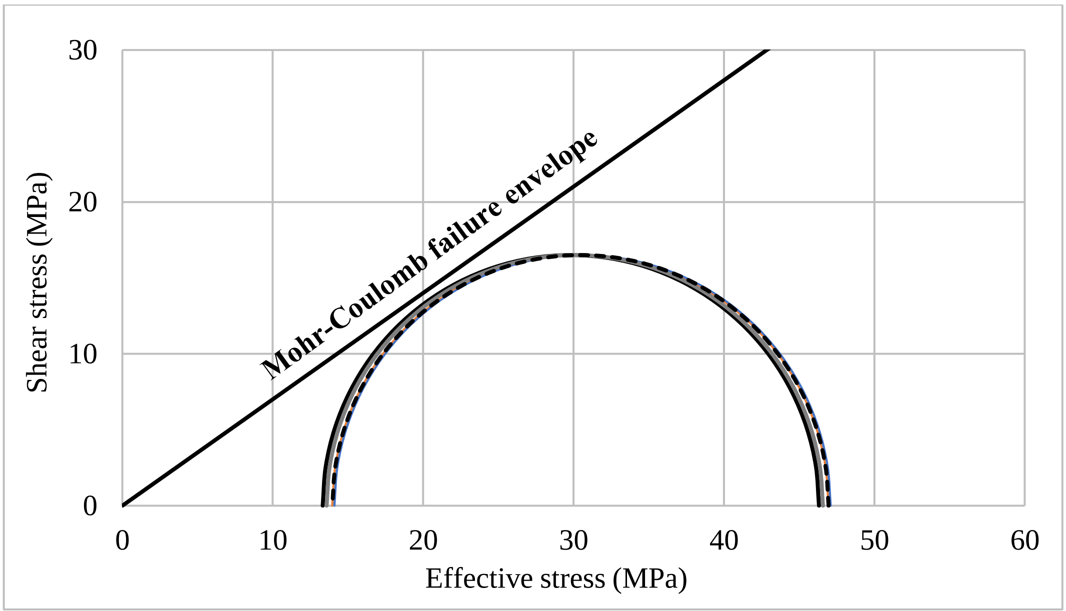

Figure 12: The changes of effective stress with considering the effect of coupling (the dashed black line depicts the initial status of effective stress, grey and black lines are showing the effective stress afterwards 100 days and six months of injection, respectively.

1.4.5 Biot's coefficient sensitivity analysis

One of the main noteworthy facts of the earlier analytical and numerical analysis is the practice of unity number for the Biot's coefficient as it was believed has no substantial impact on the geomechanical approaches to any fields. Here, through the sensitivity practices, we observed that the precise estimate of Biot's coefficient is tremendously valuable to evade any seismic events and fault reactivation. To conduct the sensitivity analysis, the Biot's coefficient of unity is applied to our calculation to establish the plots and diagrams previously shown.

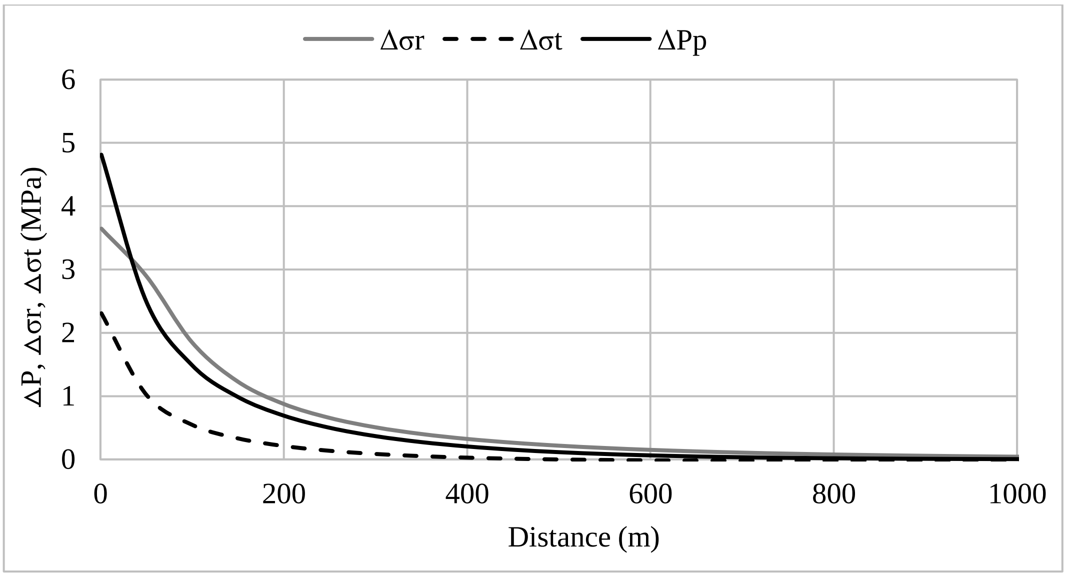

Figure 13: Stress and pore pressure evolution after six months of injection considering Biot's coefficient of unity.

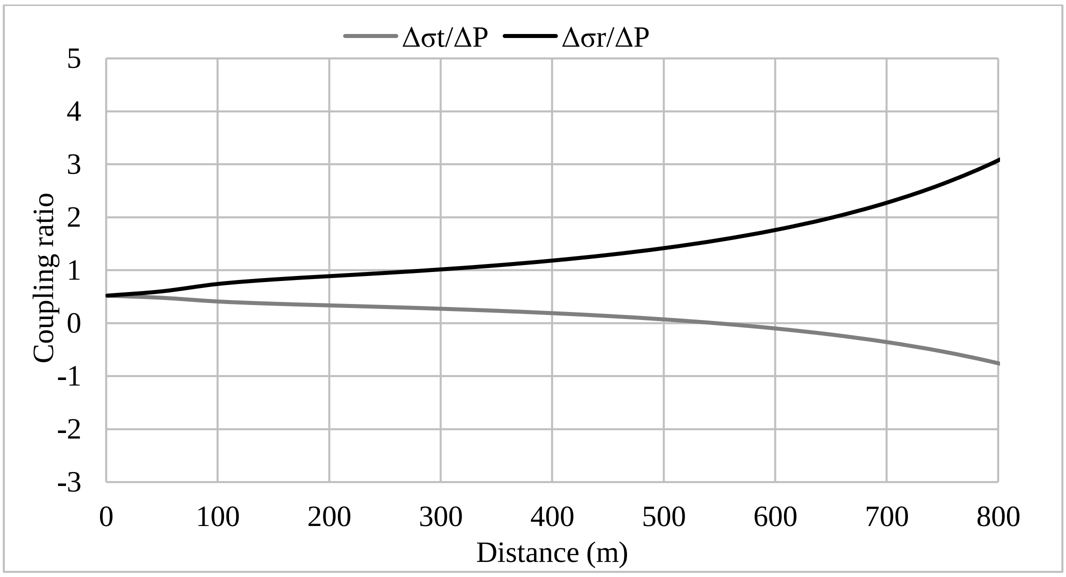

Figure 14: Coupling ratio after six months of gas injection considering Biot's coefficient of unity.

Due to the importance of the rock failure and central fault reactivation as of the current case study, the changes of the Mohr diagram are shown here. The resultant graphs show the trend of coupling ratio with the evolution of $\Delta\sigma r$, $\Delta\sigma t$ *and* ΔPp are shown in Figures 13, 14, 15 and 16 concerning Biot's coefficient of unity showing significant differences in the results.

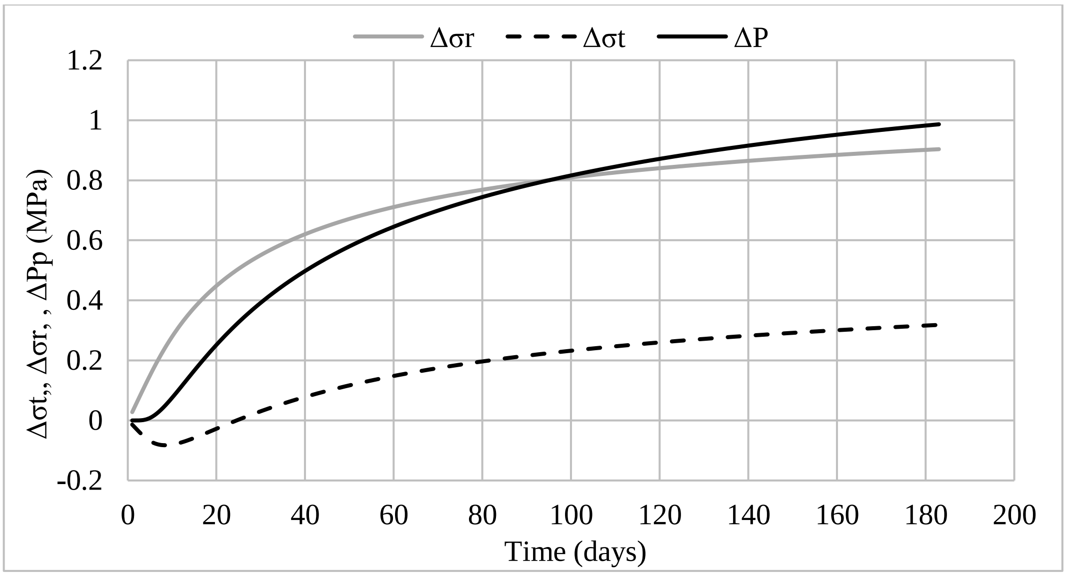

Figure 15: Radial and tangential stress and pore pressure evolution at 200 m distance from the injection point considering Biot's coefficient of unity.

It is can be seen that an accurate Biot's coefficient led to a different result in this situation (Figure 17). After 183 and 100 days of gas injection and considering the effect of poroelasticity, it appears the Mohr diagram shifts toward the failure line and increases the risks of instability in the central fault. This magnifies the impact of accurate estimation of Biot's coefficient which will be fully discussed in chapter 2 and chapter 3.

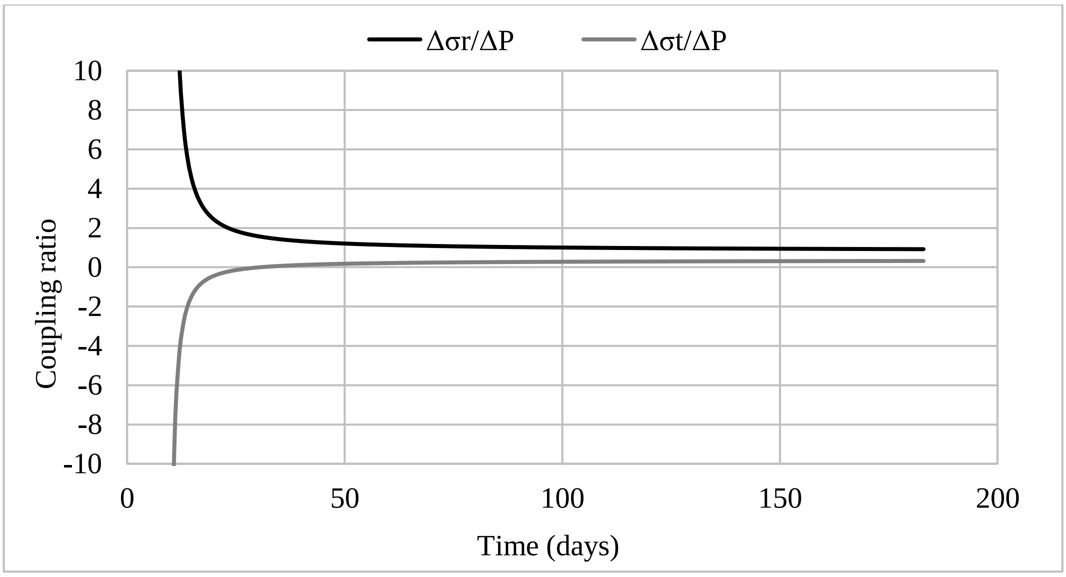

Figure 16: The evolution of coupling ratios within six months of continuous gas injection considering Biot's coefficient of unity.

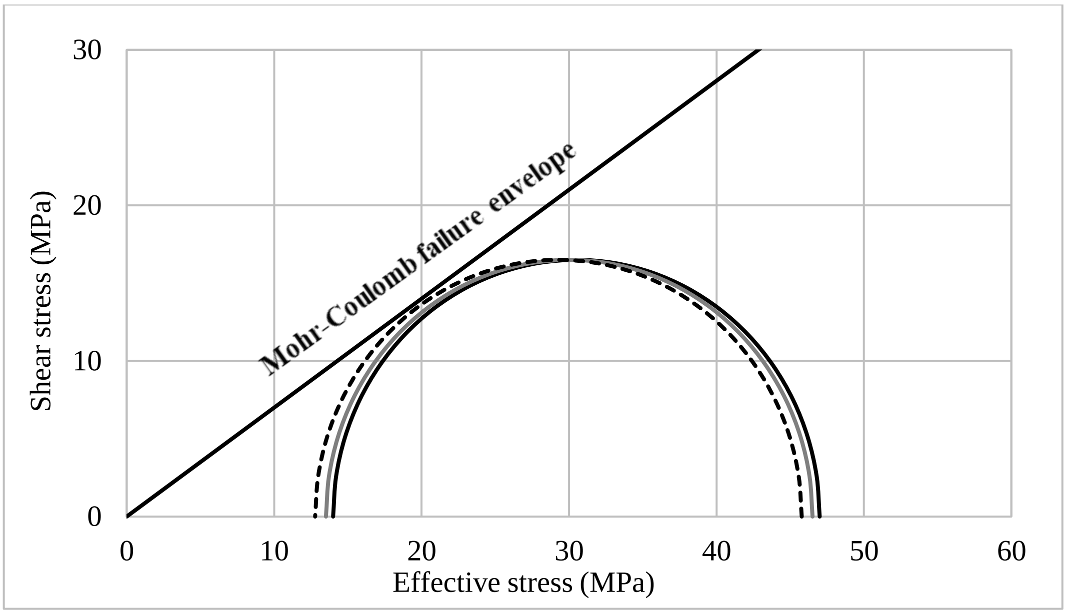

Figure 17: The variation of effective minimum horizontal stress and vertical stress with considering the effect of coupling and α=1, where the black line shows the status of initial effective stress after injection, grey and dashed black lines are the effective state of stress in 100 days and six months of injection respectively.

1.4.6 Discussion

Growing pore pressure within reservoir formation when is being subjected to continuous injection causes instability in nearby faults. The degree of effective stresses develops pore pressure changes which are known as 'coupling'. Implementing this coefficient into stress analysis and its relevant calculations is very fundamental to evaluating the possibilities of fault reactivation during the injection processes. This case study focused on the main fault stability considering poroelasticity elements in the seasonal carbon dioxide injection process to recover pressure loss during the high-demand time of the year in a Bergermeer field in the Netherlands. The initial field stress, geometry and rock properties were collected acquired from reports provided from the operation field. Subsequently, the poroelasticity modelling scenarios were employed to calculate the variation of σr, σt, *and* Pp at various time stages. The sensitivity analysis has been conducted to address the effects of periodical gas injection and distance on the instabilities of the faults. The findings of this study presented decent arrangements that match the results provided from the analytical studies and numerical investigations carried out by Hager and Toksoez (2009), de Pater et al. (2020), Berentsen et al. (2019) and Teatini et al. (2019). Furthermore, the outcomes of our investigation verified that the possibility to fix the injection point closer to the main fault if necessary, taking into consideration the accuracy of Biot's coefficient.

1.5 Conclusions

The current chapter has reviewed the specific details of time-dependent coupled geomechanical processes and considered their importance in regards to the calculation of stress and pore pressure variation during carbon dioxide injection. It has provided an overview of the previous methodologies carried out on the poroelastic behaviour of reservoirs rocks when they are subjected to injection processes. The impact of poroelasticity on a normal faulting regime has been assessed considering a relevant case study. Additionally, through applying sensitivity analysis it has been found that the accurate estimation of Biot's coefficient is extremely beneficial in preventing probable fault reactivation as well as other seismic events. In fact, applying Biot's coefficient of unity showed no satisfactory match for the case study field.

Additional accomplishment was demonstrating the variation of the effective stress during carbon dioxide injection which is mainly dependent on the distance to the faults and duration of injection. In a normal faulting regime, rock failure is amplified when the observation point is in the σV direction and weakened when the observation point is in the σh direction. Regardless of the type of faulting regime, along with maximum effective stress in case of injection, the rock becomes more unstable without considering the coupling effect. Adding to what has been found so far, the coupling magnitude throughout the reservoir varies. This agrees with the investigations by Zoback and Zinke (2002), where they analysed the coupling ratios at oil reservoirs in the North Sea (Valhall field). The coupling ratios they measured ranged from 0.70 at the crest and 0.88 at the edge of the basin.

Evidence strongly supports the fact that Biot's is a foremost characteristic in Pp and stress coupling, in relation to the distance to the injection origin and time. It is also extremely important for the rock stability analysis, which exists between the porous medium and fluids. The shape of the coupling is found to be very dependent on Biot's coefficient variation. For instance, to reactivate the fault, higher injection rates required under weaker coupling magnitude. Additionally, linear poroelastic effective stress law is often used to connect the in situ total stresses to pore pressure in underground formations. The indirect estimations of effective stress coefficient based on porosity-permeability are often not accurate. Therefore, the coefficient can be identified on retrieved samples using different laboratory settings such as the constant volumetric deformation approach. Hence, the next two chapters will mainly address the methods and protocols of accurate estimation of this factor.

Chapter 2 will now consider the importance of Biot’s coefficient and provide an overview of the origin and the application of Biot’s coefficient to the current study and petroleum industry. This will be accompanied by an introduction of a new technique in chapter 3 that is mainly based on X-ray micro computerized tomography (XRCT).

Chapter 2

2. Laboratory measurement of Biot's coefficient

2.1 Introduction

As it has been explained in chapter 1 section 1.4.5, The coefficient of Biot is a key important element for coupling analysis. Hence, chapter 2 looks at the importance of this coefficient within the petroleum industry and provides a broad investigation on its origin and its application. This is carried out through a standard literature review and analysis. chapter 2 concludes by introducing a novel approach to acoustically and dynamically measuring Biot's coefficient on the cubic sandstone samples.

Pore pressure variation during injection or production impacts the spreading process of stress (distribution) and linked strains within the reservoir rocks. Considering the poroelastic application, the coupling of *Pp* and principle stresses as discussed earlier is signified by the degree (ratio) of stresses over *Pp* variation. Similarly, the coupling factor is related to the coefficient of Biot along with the elastic properties (dynamic and static) of reservoir rocks, the existence of the immediate faults, and the status and shape of the reservoirs. Through analytical, experimental, and numerical methodologies, the interconnectivity ratio between various pressure and stress components can be assessed.

As it already has been investigated by Geertsma (1966) and Wang (2000) and as of the basis of this study, sequestration operation significantly alters the pore volume (*Vp*) in the formations. These variations are very important strategically as they may cause fault reactivation and other related environmental risks (Biot, 1954; Chen & Nur, 1992; Y Zhang et al., 2015). Hence, a clear understanding of the elastic and poroelastic response of the rock during/after any operations, particularly in relation to rock and wellbore stability and CCS projects is an important aspect of carbon dioxide injections (Biot, 1941, 1954; Biot, 1962; Detournay & Alexander, 1993; He et al., 2016; Wang, 2000).

The fundamental aspect of effective stress is vital for the prediction of poroelastic rock behaviour. The key factor in this approach is the coefficient of Biot, which is the key variable essential in order to forecast *Pp* propagation within the formation and its geological structure and also to calculate how this affects the state of stresses. Therefore, the effective stress principle (Biot theory) accordingly defines the process of *Pp* altering the rock and formation response under external loads (Cheng et al., 1993; Geertsma, 1957; Streit & Hillis, 2004; Wang et al., 2019; Yin et al., 2009). Therefore, from this point forward various practice and testing schemes will be introduced to precisely compute the Biot’s coefficient. This will be accompanied by the presentation of a new dynamic technique on a cubic sandstone sample. We also have tried (and failed) some commercially approved techniques in the industry, such as the one-step and two-step testing procedure stated by Franquet and Abass (1999).

It should be noted that this investigation has been published and presented in the APPEA journal by Salemi et al. (2018).

2.2 Background

Effective stress calculation is critically vital in determining the estimation of deformation and failure of a rock mass. The rock response to poroelasticity is beyond the existing considerations of linearity and isotropy. In fact, rocks reveal nonlinear elastic behaviour as of the fractures within their skeleton; and in the case of induced external force, they experience variation in contact size and area among grain to grain contacts (Nur & D. Byerlee, 1971; Teufel et al., 1991). Therefore, due to the micro-cracks and their bedding surface, they show anisotropic response to the external loads (Todd & Simmons, 1972; Wang, 2000; Winkler & Nur, 1982).

In the petroleum engineering scale, numerous methods are offered to evaluate the coefficient of Biot. Biot’s coefficient is calculated applying dynamic and static methodologies. From a static point of view, the matrix compressibility (C) and bulk compressibility of the specimen obtained separately via two different test laboratory tests. Notably, according to the experimental investigation carried out by Franquet and Abass (1999) when the rock matrix has an extremely low value of porosity, bulk and matrix compressibility as demonstrated through equation 19 are equal and the coefficient of Biot (α) turns into nought.

$$\alpha = 1 - \left(\frac{C_{\text{Matrix}}}{C_{\text{Bulk}}}\right) \tag{19}$$

In the dynamic approach presented by Todd and Simmons (1972) which will be discussed fully in the next section of this chapter, the numerator is the gradient of compressional travel time (*Vp*) and pore pressure curve when the degree of pressure difference is kept constant. The denominator in contrast is the gradient of compressional travel time and differential pressure (*Pd*) curve when the *Pp* remains untouched (equation 20).

$$\alpha = 1 - \left[\left(\frac{\partial V_p}{\partial P_p}\right)_{P_d}\right] / \left[\left(\frac{\partial V_p}{\partial P_d}\right)_{P_p}\right] \tag{20}$$

Where *Vp* denotes compressional travel time, *Pp* stands for pore pressure, *Pc* denotes the confining hydrostatic pressure and *Pd* stands for differential pressure and obtained from the differentiation between *Pc* and *Pp*.

The most conventional procedure was introduced by Biot and Willis (1957), where a cylindrical rock sample was placed into a metal jacket. The rock compressibility was measured by applying various confining pressures under drained (fluid cannot leave the specimen) and undrained (fluid can freely move while pressure applied) experimental condition. For this purpose, two independent experiments are required to be carried out to firstly measure *K* (bulk moduli) and secondly *Ks* (matrix bulk moduli) which theoretically can be shown by equation 21 presented by Franquet and Abass (1999).

$$\alpha = 1 - \left(\frac{K}{K_s}\right) \tag{21}$$

In order to calculate *K*, the hydrostatic compressive pressure is being applied on a jacketed specimen under no pore pressure. Consequently, confining stress is raised by pre-defined increments to obtain volumetric strain (ϵ_v) values. The ratio of *Pc* over volumetric strain changes gives *K*. *K*s can also be calculated by applying the sample hydrostatic compressive pressure. In this stage, the *Pp* must be equal or slightly less than confining pressure (*Pp=Pc*) to let the particles transfer the confining pressure. Right after the accurate measurements of the *Ks* and *K*, Biot’s coefficient can be calculated via equation 21. Note that compressibility of injected fluid and pore pressure alterations throughout the experimentations have no significant influence on the calculations.

Nevertheless, Biot’s coefficient could be determined more easily with only a one-step procedure, as per Skempton (1961). To perform this, the expelled volume (*ΔVp* of the fluid from the sample while the specimen is under hydrostatic external force is required to be measured. The ratio of *ΔVp* over the volumetric strain changes (*ΔV*) of the sample then gives Biot's constant. Franquet and Abass (1999) suggested another process, which involves "hydrostatic draining and depletion experiments". First, the rock bulk moduli measurements need to be calculated as a function of effective stress (draining test); then and there the volumetric strain (depletion test) as a function of effective stress and pore pressure. The obtained results from both tests are then plotted and the coefficient of Biot is identified via the resultant graphs.

Alternatively, rock permeability variation due to effective stress changes is another strategy to Biot's coefficient (Kümpel, 1991). According to Qiao et al. (2012), a precise calculation of permeability especially on tight formations could assist us to determine the coefficient of Biot (equation 22).

$$\frac{\Delta K_p}{\Delta K_c} = \alpha \tag{22}$$

Where *ΔKp* stands for the permeability variation when pore pressure varies from applied constant hydrostatic confining stress. On the contrary, *ΔKc* stands for the permeability variation while hydrostatic confining stress changes when pore pressure remains is kept constant.

Furthermore, He et al. (2016) proposed a new approach where they tested cylindrical Bakken shale specimens (cored from North Dakota) and measured radial and axial strain changes via strain gauges when confining stress varied. They stated in the event when *Pp* increases, the sample encounters a decline in radial and axial strains (volumetric), hence, the required hydrostatic stress to recovering the original volumetric strain needs to be recorded to calculate the coefficient of Biot. In other words, the ratio of *Pc* over Δ*Pp* as it is shown in equation 23 deliver the coefficient of Biot.

$$\frac{\Delta P_C}{\Delta P_P} = \alpha \tag{23}$$

2.2.1 Sample's preparation and properties

For this investigation, five Gosford cylindrical sandstone samples with an average 38 mm diameter and 64 mm length (Figure 18) from Gosford Quarry, NSW in Australia been chosen (Salemi et al., 2018). They are ideal for ultrasonic studies as of their homogeneity and the regular grain shape. According to the X-ray diffraction (XRD) investigation carried out by Roshan et al. (2016), these samples mainly contained quartz (83.7%), illite (8.1%), kaolinite

(7.7%), and pyrite (0.5%). Mechanical properties of the samples were measured and Young's modulus was 77 MPa with the Poisson's ratios between 0.18 and 0.21. Testing the sample via AP-608 porosimeter-permeameter, the permeability was measured and ranged between 48 mD and 50mD and the porosity was ranged between 18.25 and 19.6%.

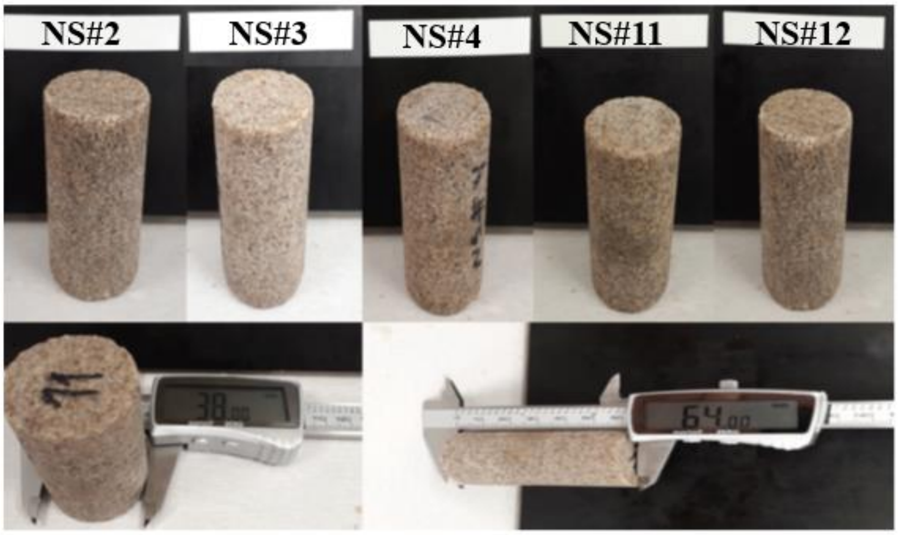

Figure 18: Gosford sandstone samples used for hydromechanical tests (Salemi et al., 2018).

2.2.2 Experiment apparatus and procedure

A stiff triaxial loading apparatus was chosen for this test. As shown in Figure 19, it is necessary to use a PC controller as a servo system for the applied axial and radial stresses. This triaxial setup could provide, sustain, record and regulate pore pressure as well as external associated with recording directional strains accurately (radial and axial displacements). The strains in each direction and other variables are required to be tested for each sample. The Hoek cell (jacketed cell) equipped with three pumps to regulate required confinement stresses. Hydrostatic pressure was applied using 260D Syringe pumps (ISCO) to deliver vertical and confining pressure separately. Through a hydraulic jack (cylindrical area of 103 cm^2) known as "Enerpac RC-756", the axial pressure is being applied (Salemi et al., 2018).

For fluid injection, the Vinci pump is known as "BTSP 250-10" was carefully used due to its precision and quiet operation. The injection fluid (brine) is composed with distilled water (95 wt%), NaCl (4 wt%, $CaCl_2$ (0.5 wt%), MgCl (0.25 wt%), and KCl (0.25 wt%). To identify pressure variations three Siemens Pressure sensors were utilized with the identification name of SITRANS P310 and accuracy of $\leq$ 0.075% and a measuring range of 0 to 70 MPa. Besides, to acquire data and record deformation during the tests, we have employed LabVIEW and a data logger (NI cDAQ-9174) as this method involves very precise volumetric strain measurements. Hence, to calculate strain alteration we used linear variable displacement (LVDT) with the commercial ID of RDP D6/02500ARA (accuracy range of ± 2.5 mm sensitivity of 160.01 mV) and two radial strain gauges are used as is shown in Figure 20. To eliminate incorrect axial deformation and calibration of LVDTs, the endplates axial strain was obtained by applying various axial pressures and plotting data to acquire the linear formula for future strain measurements. These results are deducted from the axial displacement of the sample to contribute to correct axial strain measurements.

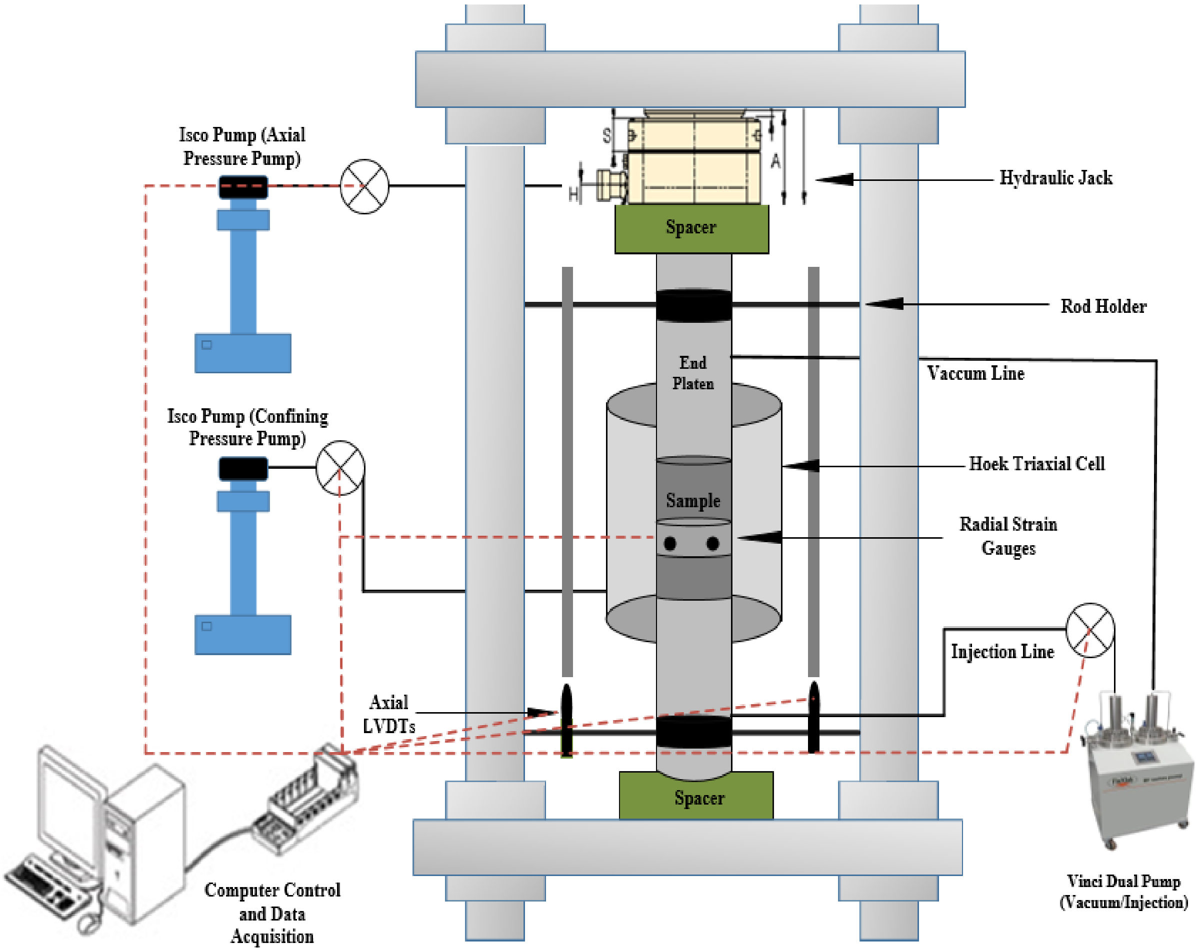

Figure 19: Schematic view of a triaxial test apparatus used for the constant constraint technique.

The constant deformation procedure represented by He et al. (2016) was applied for this experimentation. Assuming that samples are homogeneous along with the occurrence of no variations in rock properties as a result of external loads. When the volumetric strain of rock remains constant, the alteration in applied pressure and the alteration in hydrostatic stress is equal. The variable quantity namely pore pressure, confining pressure, radial, and axial strains were recorded and monitored throughout the experimentations. To calculate the volumetric strain the equation 24 have been used.

$$\epsilon_v = \epsilon_a + 2\epsilon_r \quad (24)$$

Where ϵ_a denotes the axial strain, ϵ_r denotes the radial strain and ϵ_r is the volumetric strain.

Firstly, the sample was positioned into the jacketed cell accompanied by the installation of other strain measurements gears as shown in Figure 20. The entire setup including the samples was vacuumed for a day and then saturated with brine. Due to the high salinity of the brine used and the relatively low amount of clay in the samples, no significant clay swelling is expected (Laurent et al., 1993). During the saturation stage of the test, liquid permeability for each sample is calculated and shown in this section to better understand the rock properties of the samples applying Darcy's law. For the actual test, the initial pore pressure in each experimentation was set to almost 17 MPa and confining pressure to almost 28 MPa. Then, pore pressure was increased (flow rate of 3 mL/min) gradually by the increments of 3.5 MPa and the applied confining stress to restore the strain (volumetric) to its initial status was recorded.

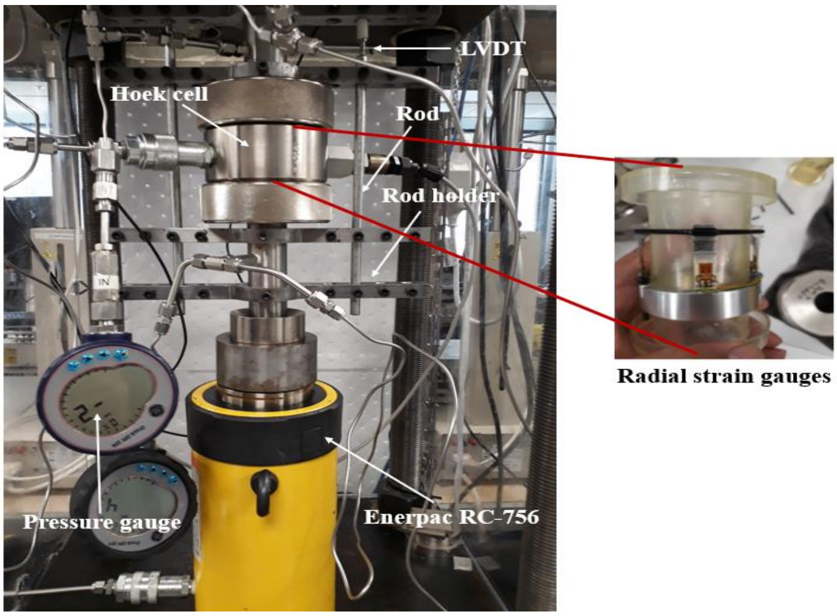

Figure 20: Test stress and measurement arrangements.

2.2.3 Results

The zero constraint (deformation) model was used as published by Salemi et al. (2018) for the current investigation. For the so-called samples, we managed to acquire the permeability that ranged between 7 and 11.5 mD and the coefficient of Biot which reached between 0.86 to 0.89. The outcomes of the performed laboratory approach agree with other experiments performed by Blöcher et al. (2014) and Qiao et al. (2012) on sandstones with identical mechanical and petrophysical properties. This matches relevant laboratory test carried out by other investigators where they measured the effective stress coefficients ranged between almost 0.65 and 0.9.

For better clarification of the experiment and the procedure explained in previous section, Table 4 and Figure 21 are showing the detailed procedure and results of the test for one Gosford specimen (NS1 #2) in three different hydrostatic confining pressures. Accordingly, Table 5 shows the coefficient of Biot of the entire specimens. The results are changing between the range of most identical sandstones investigated by other studies (Chen et al., 2004; Franquet & Abass, 1999; Qiao et al., 2012).

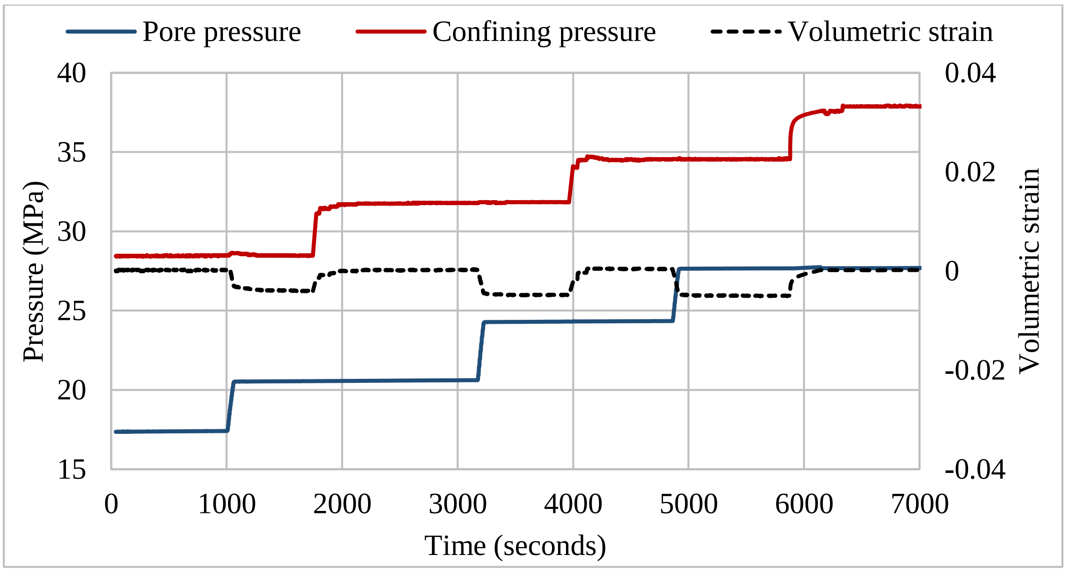

Figure 21: Experiment results for NS1#2 specimen (volumetric strain remains constant for different pore pressure and confining pressure conditions).

Table 4: Experiment results for NS1 #2 Gosford specimen.

Pp (MPa)		**Pc (MPa)**		**Biot's coefficient**
Before	After	Before	After	
17.21	20.7	27.53	30.7	0.91
20.7	24.16	30.7	33.8	0.89
24.16	27.65	33.8	36.87	0.88

To be able to monitor the relationship between permeability and the coefficient of Biot, Figure 22 is plotted for two samples (NS1 #2 and NS1 #3). According to the figure, both variants are decreasing while the specimens facing higher hydrostatic stress. This verifies that hydrostatic pressure is a significant factor resulting in the coefficient of Biot variation. The entire results range between 0.84 and 0.90.

Table 5: Complete experiment results.

Sample ID	Permeability (mD)	Porosity	Biot's coefficient
NS1 #2	10.01	18.1	0.89
NS1 #3	9.54	18.3	0.86
NS1 #4	8.03	79.5	0.88
NS1 #11	7.45	17.6	0.89
NS1 #12	10.94	19.6	0.87

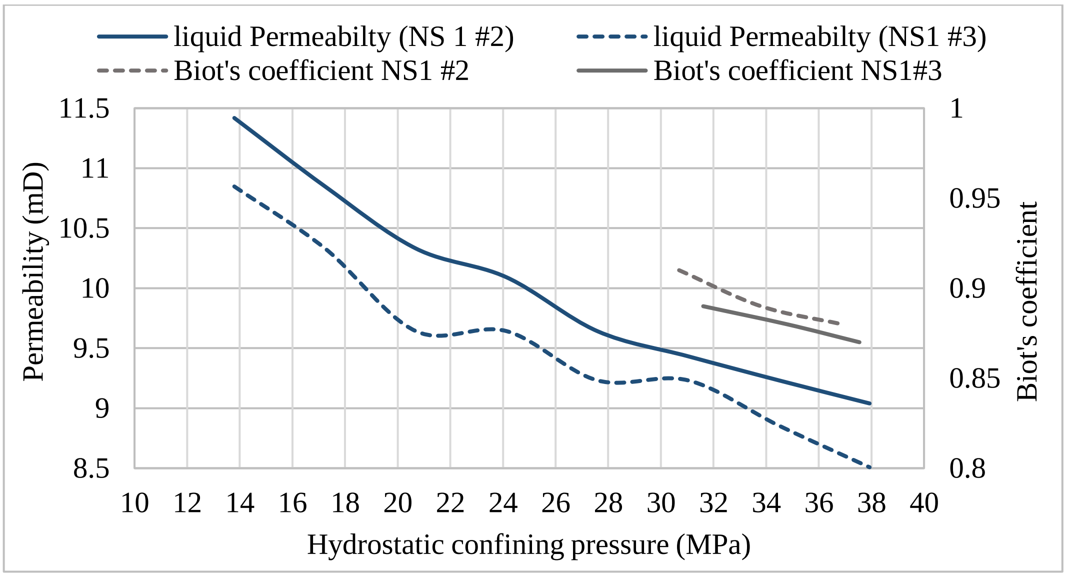

Figure 22: Biot's coefficient and permeability results against hydrostatic effective stress.

In section 2.5, the acoustic methodology will be discussed using identical Gosford cubic sandstone specimen via the True Triaxial Cell (TTSC) on a larger scale. This testing was carried out applying Todd and Simmons (1972) proposition, i.e. using acoustic velocity. According to the outcome of the TTSC acoustic tests, Biot's coefficients ranged between 0.92 and 0.98. Considering acoustic experiment as a constant deformation test is a static experiment; the results are somewhat high. For that reason, further analysis is necessary to acquire the Biot's coefficient under different anisotropic conditions.

2.3 Failures

As we mentioned earlier in section 2.1, we showed a different type of conventional techniques for acquiring Biot's coefficient. In a one-step procedure using the triaxial test apparatus that is introduced earlier, the accurate drained volume measurement is essential when the sample is subjected to an increment of confining stress. Besides, for the indirect measurement test (two-step technique), two separate calculations (equation 21) must be applied to first obtain the value of *K* and the second the value of *Ks*. It is assumed that the rock properties encounter no changes during the test and the sample is isotropic and homogenous (Biot, 1954; Franquet & Abass, 1999; Ljunggren et al., 2003).

2.3.1 Indirect measurement

This method requires two separate tests. First, we measured the bulk modulus of the sample by applying hydrostatic stress on a jacketed sample when no fluid pressure is applied. *K* will be the proportion of confining pressure variation over volumetric strain variation. The volumetric strain is measured via equation 24.

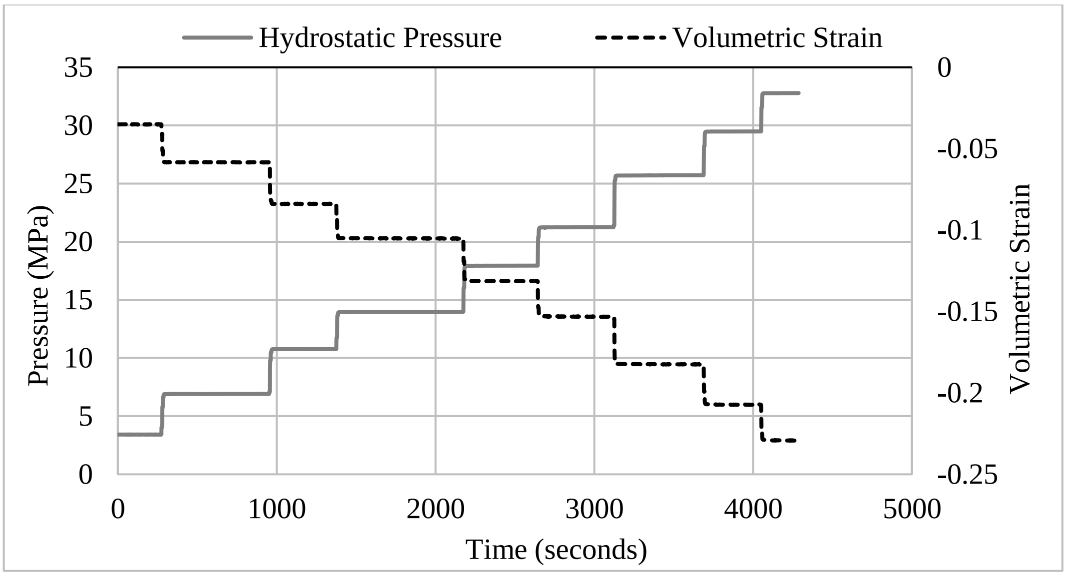

Figure 23: Hydrostatic pressure versus volumetric stress changes when Pp=0.

For the purpose of this test, the NS1 (Gosford sandstone) specimen is used with the physical properties explained in section 2.2.1. Figure 23 presents the results of the first step of this test. Along the lines of the previous test, the sample prior to the test was subjected to 24 hours vacuum and left under 4 MPa of hydrostatic pressure for another day. The hydrostatic pressure was increased by increments of 3.5 MPa and continued to almost 34 MPa. The second step of the test followed the same procedure, but the main difference was in maintaining equal pore and hydrostatic pressure (*Pp=Pc*). This actively stimulates the variation of hydrostatic pressure and volumetric strain in an unjacketed rock sample. Figure 24 demonstrates the results of this test. Note that, in this approach when the hydrostatic pressure reached almost 18 MPa, leakage occurred through the sample which called for the test to be stopped.

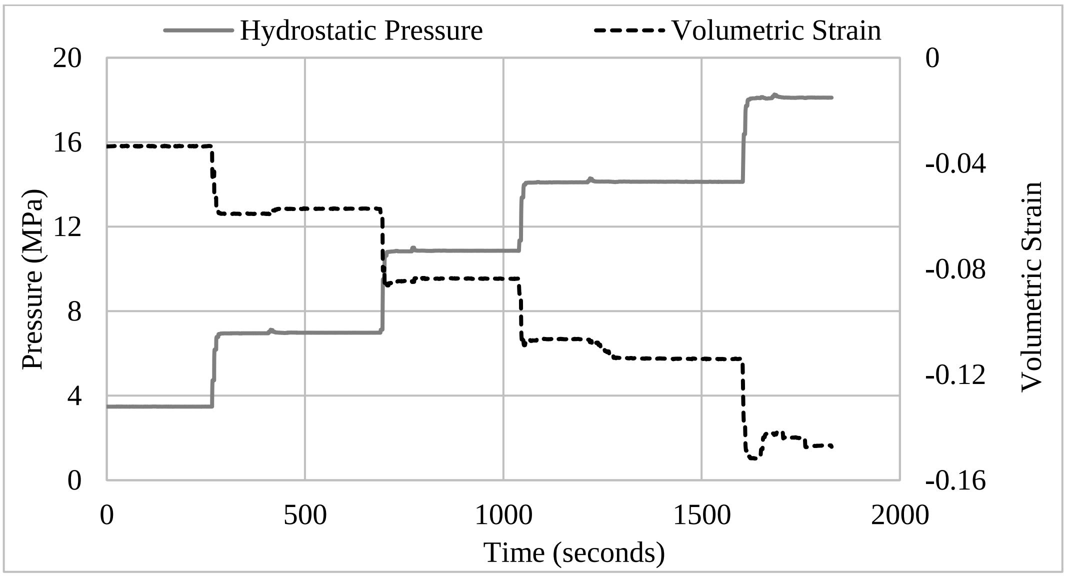

Figure 24: Hydrostatic pressure versus volumetric stress changes when Pp=Pc.

Table 6: The calculated Biot's coefficient (in red) through indirect measurement technique for Gosford sandstone specimen.

ΔPc (MPa)	**When Pp=0**		**When Pp=Pc**		**α=1-K/Ks**
	Δεv	K=ΔPc/Δεv	Δεv	Ks =ΔPc/Δεv	
3.5	0.039697		0.035112		
7	0.059933	174.3383137	0.057236	156.8722576	**-0.1113394**
10.5	0.090744	123.3283718	0.083597	146.8407905	**0.1601218**
14	0.105164	228.5845064	0.114064	106.2730444	**-1.1509171**
18	0.131295	152.2132524	0.147345	118.0871415	**-0.2889909**

Table 6 shows the intended Biot's coefficient (highlighted in red) via indirect measurement technique for the Gosford sandstone sample. Consequently, the Biot's constant is not within the range of zero to unity and came out completely off the range as it is not within the range of 0 to 1. The same procedure was applied on various samples with different physical properties and still achieved no promising results. This is due to the need for highly advanced gears (servomechanism) or accurate estimation of volumetric strain (perhaps via strain gauges). An attempt was carried out to adhere strain gauges (radially and axially) to the sample instead of LVDTs and then perform the test. This attempt was a failure too as the fluid started to leak through the sleeve inside the Hoek cell.

2.3.2 Direct measurement

Despite the indirect test, this application only requires one approach. The volume of fluid drained from the specimen due to applied confining pressure increase is needed to calculate Biot's coefficient. This must be performed in a drained condition (fluid can enter and exit within the porous media) while pore pressure is kept constant. This idea of volume measurement instead of bulk modulus measurement essentially originated from equation 21 ($\alpha = 1 - \Delta Vp/\Delta V$). Therefore, the coefficient of Biot is one minus the ratio of pore volume variation (ΔVp) over the total volume changes (ΔV), as derived from and explained by Franquet and Abass (1999).

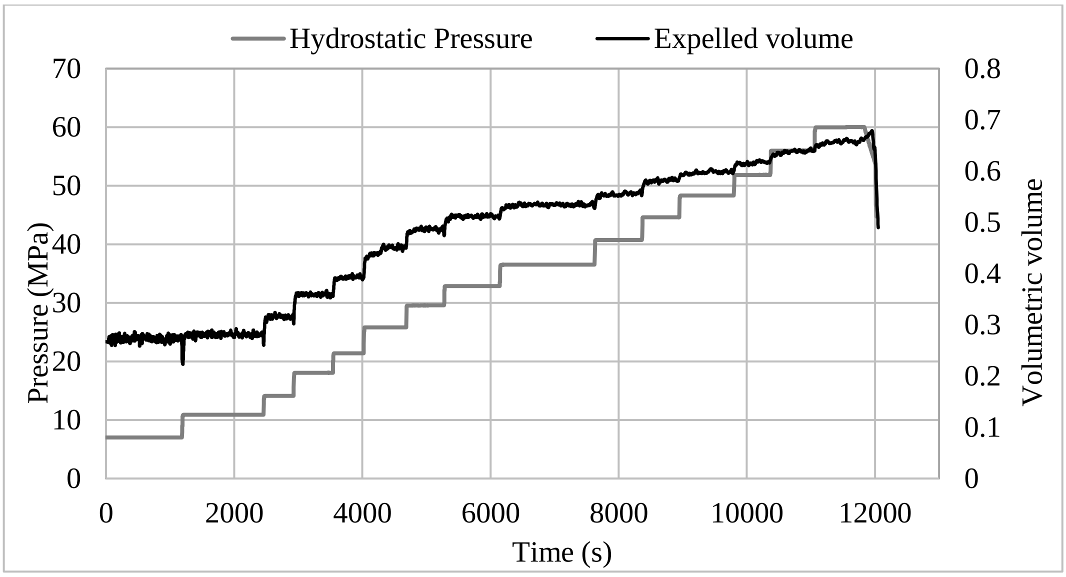

Figure 25: Hydrostatic pressure versus expelled volume when pore pressure was kept equal to hydrostatic pressure (direct approach).

For this study, a Gosford sample with similar characteristics explained in the zero-constraint method were used, along with some other attempts on different samples. We used the Vinci pump (Figure 19) and also the resultant graph (Figure 25) to accurately measure the expelled fluid volume from the sample, and managed to maintain servo conditions for better results. Figure 25 along with Table 7 present the result of this attempt (highlighted in red). Clearly, the graph shows the hydrostatic stress carried out until 55 MPa with various increments. After each increment, a few minutes were allowed to give the setup and the measurement devices time to provide the precise values. Accordingly, when the pressure rose the results became unreliable and off the range. Our investigation showed no matching result to the previous hydromechanical tests either. There are many reasons why this test becomes invalid. The main one is that it is very challenging to simulate the ideal reservoir hydrostatic conditions within the laboratory setup. The second is the inaccurate measurement of volume expelled from the sample, as this might include some of the fluid left inside the pipelines or fluid evaporation errors could occur. Therefore, this test has deemed a failure, despite a great deal of time and effort being into it and despite the very sophisticated procedure and tools that were employed.

Table 7: The result for the one-step approach toward Biot's coefficient calculation.

Hydrostatic pressure (MPa)	Bulk volume variation (cc) (ΔV)	Expelled volume (cc) (ΔVp)	Biot's coefficient ($\alpha = 1 - \Delta Vp/\Delta V$)
6.90			
10.34	0.25	0.25	1.00
13.79	0.30	0.16	0.53
17.24	0.34	0.13	0.39
20.69	0.43	0.10	0.23
24.14	0.51	0.10	0.20
27.59	0.53	0.10	0.20
31.03	0.55	0.09	0.17
34.48	0.59	0.08	0.13
37.93	0.60	0.07	0.11
41.38	0.63	0.07	0.11
44.83	0.60	0.06	0.10
48.28	0.62	0.05	0.09
51.72	0.63	0.06	0.09
55.17	0.65	0.05	0.08

2.4 Findings

Amongst accessible conventional methods for determining the coefficient of Biot, the constant constraint deformation procedure was the only method with promising results chosen for this experiment, which was presented earlier by He et al. (2016). The conventional procedures significantly alter the rock properties (e.g., one-step/two-step methods) as they need to be executed in two different stages, or they require very precise pore volume estimation during confining pressure changes (Franquet & Abass, 1999). In contrast, upholding the zero-volumetric strain technique simply involves a single approach with less complexity.

2.5 Acoustic method to ascertain Biot's coefficient (TTSC)

So far, we have shown the existing methods within the scale of industry and laboratory to measure the Biot's constant. In this section, an acoustic attempt is considered, using a cubic sandstone specimen to measure Biot's coefficient via true triaxial cell (TTSC). Historically, nearly the majority of the earlier attempts were performed on cylindrical samples. However, in this case, the test was applied for the first time on a 50 mm cubic sample. Rock dynamic properties were measured via fixed ultrasonic acoustic sensors inside the TTSC cell in a dried and brine-saturated condition before the actual test, to grasp the anisotropy and homogeneity of the sample (Kraaijpoel et al., 2013; Salemi et al., 2020). We mainly aimed to classify the effect of *Pp* on dynamic properties and compressional wave velocity of the rock under hydrostatic stress (reservoir condition).

2.5.1 Sample dynamic properties

The olden times of transducers application using electro-mechanical transducers at a laboratory-scale go back to Kaufman and Roever (1951). The earliest seismic sources were introduced by Hilterman (1970) who used electro-mechanical transducers and their sparks, although piezoelectric transducers are considered as receivers and source at the same time. Consequently, the ultrasonic outputs are assumed to be trustworthy and similar to actual field measurements (Riznichenko, 1966; O'Brien and Symes, 1971). To obtain dynamic properties of the cubic sample the ultrasonic study was carried out.

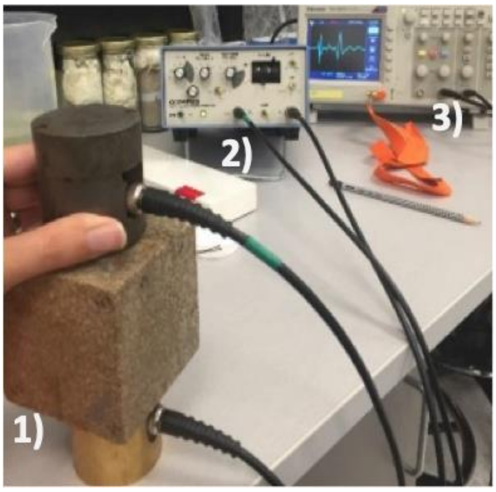

(a) ***(b)***

Figure 26: The sample divisions for each dimension (a), and the test arrangement (b) which involves a pair of S-wave transducers (1), pulser (2), and oscilloscope (3).

The 50 mm^3 cubic specimen chosen for this study was identical to the sample used in section 2.2.1 (equivalent mechanical and physical properties). The Gosford specimen was cut with an accuracy of 0.02 mm and was refined for smoother edges. As shown in Figure 26a, the centre of each face was marked to attach the transducers for compressional wave and shear wave velocity measurements. An ultrasonic pulse transmission consists of "1 MHz S-wave Olympus transducers, pulser/receiver 5077PR, and digital oscilloscope HS-4 (50 MHz)" (Salemi et al., 2020). To calibrate the transducers and transmission tools, the wave travel time with the presence of no specimen (dead-time) was noted, which later will be included in the analysis. For better signal transmission and connection between Olympus transducers, the transmission tools and oscilloscope, the SWC-2 is considered and applied to the setup. Figure 26b shows the transducers, pulser and oscilloscope used for the test and below the steps toward *Vp* and *Vs* calculations are shown.

- Dead-time calibration
- No pressure to be applied to the dry specimen
- Calculate the first arrival for each face
- Velocity calculation (first arrivals divided by the length of each face)
- Calculation of dynamic properties via provided formulas

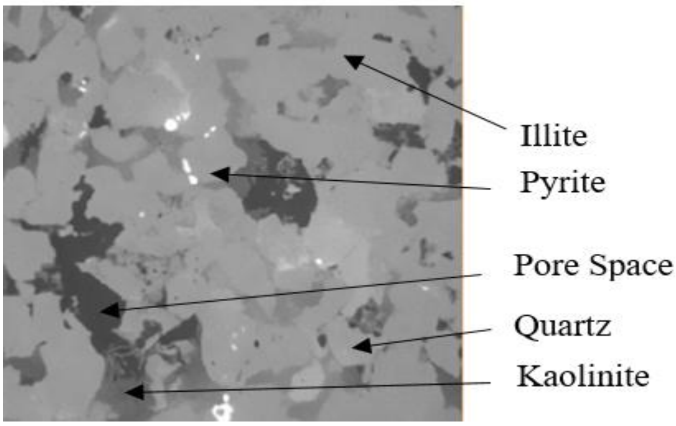

Figure 27: The Micro-Ct image of the sample showing the anisotropy (Salemi et al., 2020).

Table 8 shows the dynamic properties of the sample. The results confirm the anisotropy of the sample with variations of 12% in compressional wave velocity and 6 % in shear wave velocity. Note that the microstructure of this specific rock specimen is a key element affecting the accuracy of the result and related anisotropy. To assess the anisotropy of the rock we performed a micro-CT imaging technique as shown in Figure 27 (the grain level) to verify the results. To reduce anisotropy and idealize the sample for the acoustic measurements, the cubic rock was exposed to hydrostatic stress to minimize the microstructure and the pores within the porous media. So far, we carried the acoustic measurement to calculate the dynamic properties of the Gosford sandstone specimen. This was necessary to acquire a brief understanding of the rock behaviour during Biot's coefficient measurements. The Ct scan images showed that the grain size in this type of rock varies. The anisotropy of the rock mainly originates from the grain sizes. Besides when no pressure applied to the sample, the main parameter affecting the wave transmission and its related accuracy is the microstructure of the rock. The wave transmission and propagation within the grains in each face of the cubic sample are shown in Figure 28. As shown in the figure, the rock's anisotropy is apparent in either *Vp* and *Vs*.

Table 8: Variation of Vp, Vs and dynamic properties in different faces.

Face	**A**	**B**	**C**
V_p (m/s)	2980	2780	3160
V_s (m/s)	1990	1987	2110
V_p/V_s	1.5	1.4	1.5
E_d (GPa)	19.15	16.96	21.50
K_d (GPa)	8	5.4	8.9
υ_d	0.1	0.02	0.09

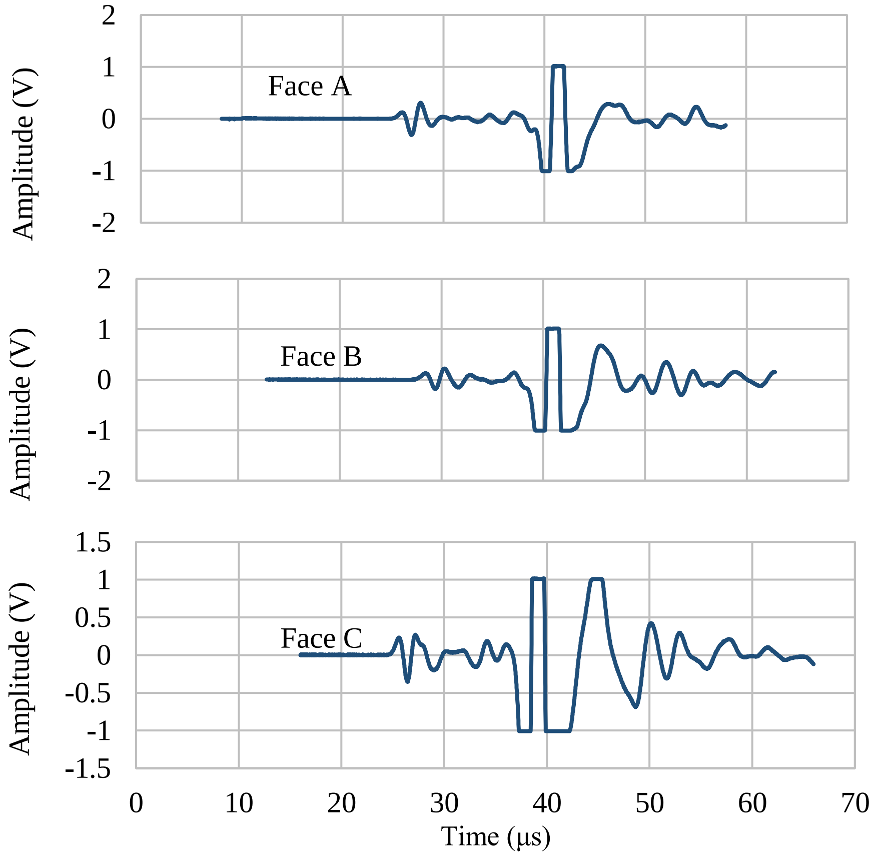

Figure 28: Variation of Vp and Vs first arrivals for the dry specimen.

2.5.2 Acoustic background

Before entering the methodology and the apparatus used for this test, it is appropriate to look into the history of effective stress measurements acoustically. The influence of effective stress variation on compressional velocity in various types of rock specimens has been studied widely in the literature. However, the impact of fluid pressure within the rock skeleton is infrequently studied. Christensen and Wang (1985) studied the fluid and hydrostatic pressure effect on the elastic wave velocities for a different type of sandstone, especially, water-saturated Berea sandstones (U.S). They identified that when pore and confining pressure are raised with similar increment, *Vp* rises and *Vs* drops accordingly. In addition to their outstanding results, they derived a set of dynamic elastic constants too.

A decade later, Prasad and Manghnani (1997) proposed an advanced technique and measured a series of dynamic poroelastic parameters (e.g., Biot's coefficient). They proposed that *Vp* is a function of *Pc*. Relative to the topic of our research they managed to acquire Biot's coefficient for Berea sandstone. Their results showed the coefficient is declining when hydrostatic confining stress is increasing. They also have verified that under a constant fluid pressure condition, when differential pressure is increasing, the compressional velocity increases. Similarly, Siggins et al. (2001) calculated the dynamic properties for the samples cored from the Carnarvon Basin located in the Australian Northwest Shelf, employing. They studied and showed that compressional wave velocity variation depends on the microstructure of the sample (rock skeleton) and the existing fluid pressure within grains. Their Biot's coefficient ranged between 0.66 and 0.77.

2.5.3 Experiment apparatus and procedure

The True Triaxial Cell (TTSC), as shown in Figure 29 was chosen for this experiment with mounted ultrasonic transducers to monitor compressional velocity on a 50 mm^3 cubic Gosford sample. The pumps used to apply stresses and pore pressure are the same as the ones used for the previous test. The Keller pressure transducers were chosen to regulate and monitor the hydrostatic stress; and to apply pore pressure, the high-pressure syringe pump was used. As shown in Figure 29, the cell with the mounted 24 transducers was placed inside the oven to control and maintain the constant temperature and avoid thermal effects on the entire setting, wiring and test results. The transducers are mounted to each face of the sample (four transducers at the centre of the six faces). The electric signals (pulses) are recorded via four transducers that attached to the end of each face. Once the pulses are sent from one side of the sample, the travel time is recorded with five transducers on the other side (opposite) of the sample. The accuracy of the data depends extremely on the status of the applied hydrostatic stress, fluid pressure, and sample size (RezaGholilou et al., 2019).

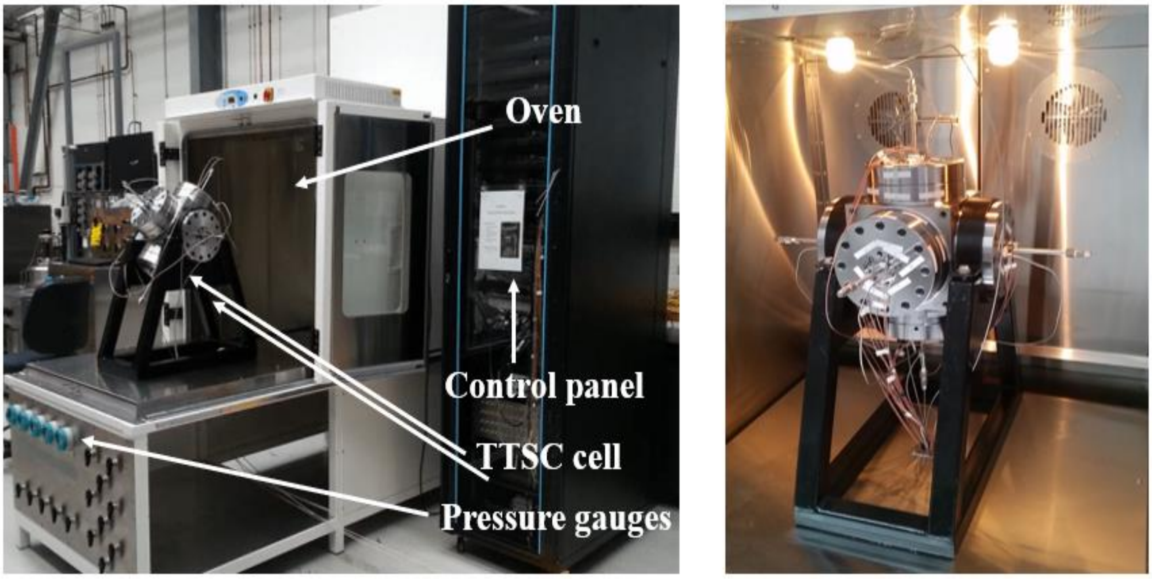

Figure 29: Complete True triaxial cell test setup and oven.

2.5.4 Compressional wave variation due to pore pressure changes

The variation of *Pp* has a significant impact on all types of velocity evaluation (Todd & Simmons, 1972). Deliberate data of the rock's properties as it has been calculated in section 2.5.1 when the sample is subjected to pore pressure variations in the reservoir, benefits cost controllers to lower the cost of excavation (Siggins et al., 2001). Therefore, in this section, we aim to dynamically acquire the properties of the sandstone which mainly involves measuring the deviations of *Vp* as a result of fluid pressure changes along with accurate measurement of Biot's coefficient. Prior to the actual test, the setting (pipeline, and sample) was saturated and filled with synthetic brine with the composition detailed in section 2.2.1 for a day. At first, the sample was hydrostatically stressed at certain pressure under no pore pressure (*Pp*=0) and *Vp* was measured. A similar process was repeated when the pore pressure was increased ranging from 0.7 and 2.1 MPa.

Table 9 shows the *Vp* results in various *Pp* ranges and hydrostatic pressure. Presumably, the confining hydrostatic stress had to be always greater than fluid pressure to minimize the risk of a leak and corresponding errors in the settings. Figure 30 provides the *Vp* results which range between 3000 and 3500 m/s with an accuracy of 2%. According to the figure, pore pressure has a large impact on the growth of *Vp*. Higher the *Pp* the higher *Vp* when is compared with the no pore pressure test. The difference in *Vp* signifies why at a certain pore pressure, *Vp* is growing.

Table 9: Vp against pore pressure (Salemi et al., 2020).

Pc (MPa)	**Compressional wave velocity (m/s)**			
	P_p=0 (MPa)	**P_p=0.7 (MPa)**	**P_p=1.4 (MPa)**	**P_p=2.1 (MPa)**
0.7	3017			
1.4	3038	3022		
2.1	3047	3074	3047	3020
2.8	3056	3126	3098	3071
3.4	3066	3178	3150	3121
4.1	3114	3220	3196	3172
4.8	3162	3262	3243	3223
5.5	3210	3304	3289	3274
6.2	3258	3346	3319	3293
6.9	3306	3387	3350	3312
7.6	3325	3403	3367	3330
8.3	3344	3419	3384	3349
9	3364	3434	3401	3368
9.7	3383	3450	3414	3378
10.3	3402	3466	3427	3388

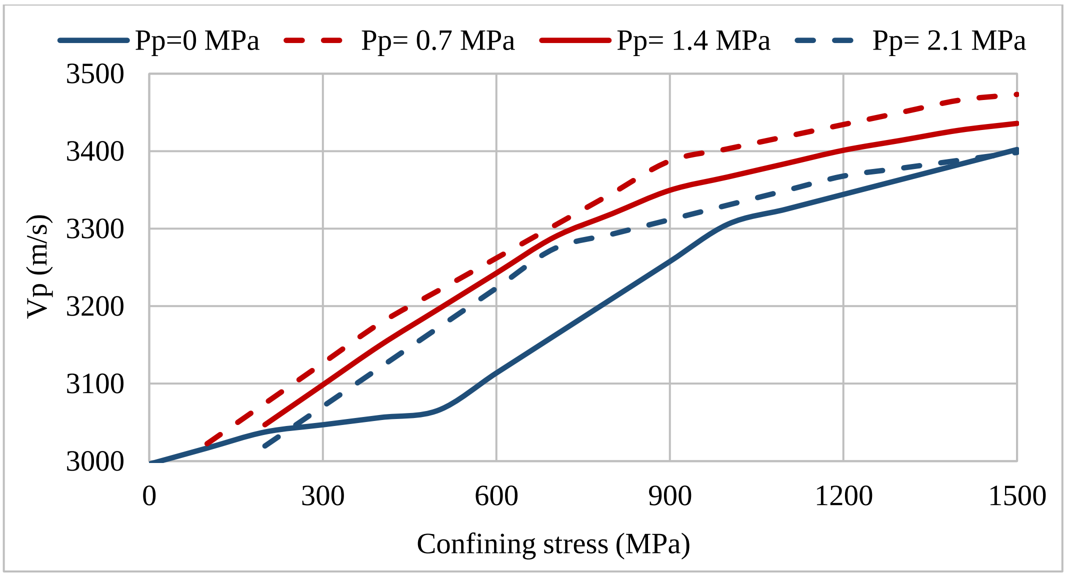

Figure 30: The variation of Vp against Pc and Pp.

2.5.5 Discussion

The *Vp* measurement at this point is employed to calculate Biot's coefficient. Equation 20 derived previously by Todd and Simmons (1972) is taken into account for the calculations. As shown in Figure 31, under various pore pressure the Biot's coefficient ranged between 0.92 and 0.98. It is also seen through the results that the coefficient of Biot decreases with higher hydrostatic *Pc*. The calculated dynamic results is within the range of most of the laboratory investigations carried out by other researchers (Salemi et al., 2018). Additionally, the outcome of our study is for a series of chosen confining and pore pressures. Note that when pore pressure is fixed to be 0.7 MPa, the Biot's coefficient stayed the same throughout the test in comparison to when higher pore pressures were used.

In this work, the dynamic poroelastic and elastic properties (e.g., Biot's coefficient, Shear, Bulk and Young modulus) were calculated using acoustic velocity values using the cubic Gosford sandstone specimen. This knowledge about dynamic values of the rocks, ascertain a broad understanding in regards to the dynamic response of the rock samples when undergoing the TTSC test. Besides, it delivers a benchmark for future true triaxial experiments when poroelastic measurements are needed to be carried out.

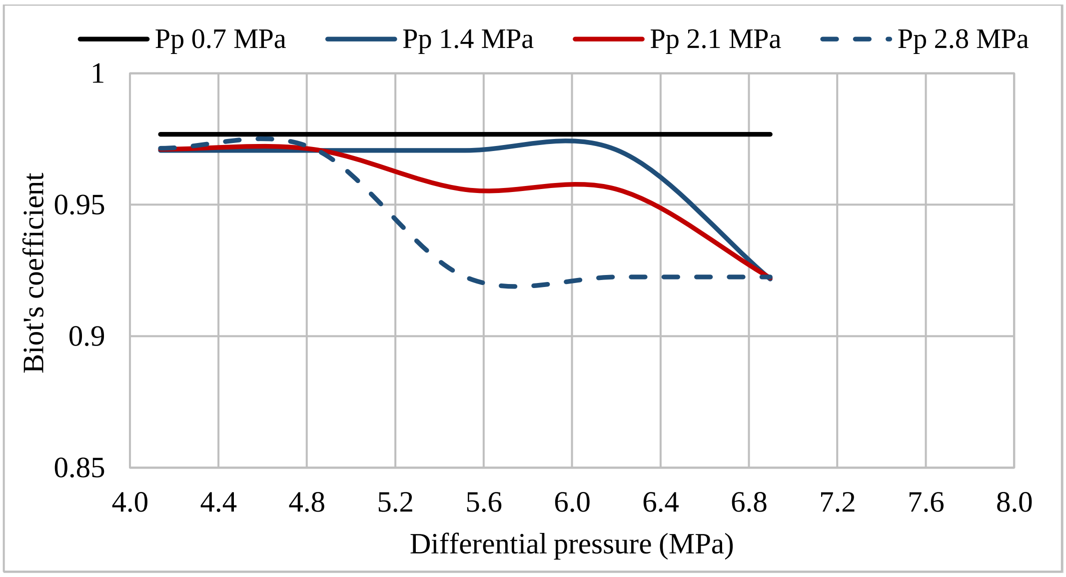

Figure 31: Entire Biot's coefficient results Vs. differential pressure.

2.6 Conclusions

This chapter has reviewed the importance of Biot's coefficient and provided a broad overview of the origin and the application of the coefficient within the petroleum industry. Some of the hydro-mechanical techniques suggested by the literature were been put into practice. This was accompanied by the introduction of a new dynamic approach to measuring the coefficient of Biot.

It was found that the integrity of the reservoir formation and stability of injection and production wells could be deliberately assessed via accurate *Pp* and stress interconnection measurements. Various type of stress analysis in this regard must be investigated both analytically and numerically, which mainly leads to poroelastic parameters measurements, such as Biot's coefficient. Hence, an attempt was made to calculate these parameters using sandstone samples. Consolidating existing methods, four distinguishable approaches were undertaken in laboratory-based practice to estimate Biot's coefficient. The dynamic method exhibited somewhat larger values than the other methods. Although some differences were shown, all methods showed similar tendencies. Assessments executed using laboratory-based scales require thorough checking, as tools and apparatus have the potential to cause inaccurate results. Chapter 3 will now introduce a unique and promising technique to measure Biot's constant via X-ray micro-computed tomography (XRCT). This will be accompanied by uses of the constant volumetric deformation tests explained above to justify the XRCT results.

Chapter 3

3. Accurate estimation of Biot's coefficient using X-ray micro-computed tomography

3.1 Introduction

This chapter reviews the relevant literature and introduces a unique method to calculate Biot's quantity via X-ray micro-computed tomography (XRCT). The proposing technique enables us to accurately measure Biot's coefficient in three orthogonal directions and thus fully appreciate its anisotropy. Results are validated with conventional Biot's coefficient measurement experiments. This chapter concludes with the validation of XRCT results via constant volumetric deformation tests explained previously in chapter 2.

Biot's theory and Biot's coefficient can describe the hydromechanical behaviour of a porous medium (Chen et al., 2004). Accurate estimation of this coefficient leads engineers to better optimization of drilling and hydraulic fracturing, production recovery, and mainly reservoir and wellbore stability. Poroelastic (elastic deformation of porous rock) theory was developed to explain the ways this change may occur. For instance, the theory can explain the degree of compaction/subsidence during and after hydrocarbon production from a reservoir (Streit & Hillis, 2004). Kumpel (1991) has discussed a comprehensive list of the associated poroelastic parameters including the compressibility of grain and pore spaces, Biot's coefficient, Skemption ratio (parameter of *Pp*), Darcy conductivity, and hydraulic diffusivity). Based on his extensive investigation of the poroelastic behaviour of a different type of rock, *Pp* changes have a profound impact in regards to the magnitude and pattern of effective in-situ stress alteration. Biot's coefficient, on which we focus here, is vital for the magnitude of pore pressure influence on effective stress (Addis et al., 1998; Geertsma, 1957; Laurent et al., 1993; Roshan & Rahman, 2011; Streit & Hillis, 2004; Todd & Simmons, 1972). Some researchers have correlated Biot's coefficient with the consolidation degree of the rocks; thus the Biot coefficient is assumed constant for each rock type (Nermoen et al., 2013; Roever, 1951). In contrast, other researchers found it mainly depends on the degree of applied stresses, porosity, and rock permeability (Franquet & Abass, 1999; He et al., 2016; Nermoen et al., 2013; Qiao et al., 2012; Salemi et al., 2018; Skempton, 1961).

The development of XRCT methods allows digital imaging exploration at the pore scale. Image processing techniques (IPT) are a widely recognized application in the petroleum industries to measure the petrophysical and poroelastic properties of several types of rocks (Borges et al., 2018). In terms of micro-CT analysis and the purpose of this investigation, there have been few studies and analysis conducted and most lack accuracy, or they indirectly measure Biot's coefficient. Some of the earliest micro-CT image processing attempts in rock physics were carried out by Arns et al. (2002), Keehm et al. (2001) and Knackstedt et al. (2009). In their work, they discussed and described the combination of 3D imaging tools and data applied to more conventional petrographic analysis to obtain the mineralogy of rocks and ascertain the correlation between the structure of reservoir rocks and the petrophysical properties of porous rock. Their analysis led to the identification of parameters such as the types of the rock (grain size distribution), as well as pore structure. Within the petroleum sector, the Biot's coefficient can be measured via digital rock technology where Ahmed et al. use 3D images of rocks associate with numerical simulation (Ahmed et al., 2017). Ahmed et al. (2018) measured drained bulk modulus and bulk moduli of the soil pack with IPT techniques. Utilizing Equation 3 (chapter 1), with having the bulk moduli of solid and the fluid-filled rock, it is achievable to indirectly measure Biot's coefficient. Despite the fact, their analysis is only conducted for contactless grains in a sand pack where the resultant Biot's coefficient was close to 1, their investigation opens the avenue to rock analysis. Similarly, Mukunoki et al. (2016) used image processing technology to measure pore diameters in a 3D setup, which enables us to measure mechanical properties of rock specimens.

The applied stresses are carried through both the grain's interfaces and the existing fluid within the rock framework, which significantly reduces the total applied force on the solid particles. Therefore, the exchanged force between the pore fluids and grains is equal to the contact area of fluid, and grains multiplied with the existing pressure within the pores. Consequently, Biot's number can be measured by calculating the ratio of grain-to-grain contacts to the full cross-sectional area of the rock. This approach here is used at a micrometre level using x-ray micro-computed tomography, where the total cross-section of the sample and the grain-to-grain contact area across an arbitrary plane can be measured (Iglauer et al., 2014).

Here in this section, we first discuss the underpinning principles and then describe the micro-CT scanning procedure. Subsequently, we validate the micrometre-scaled results with independent measurements performed on standard cores using a standard Biot-measurement methodology carried out by Salemi et al. (2018). The results are then discussed, and the implications of this work are outlined.

3.2 Analytical model development

From the geotechnical point of view, a large number of studies have focused on the relation between rock's internal fluid pressure and applied loads considering the strain variations. While the applied stresses transmit through the solid particles, existing fluids within the grains decrease the magnitude of external forces. Considering the influence of fluid pressure, Biot theory justifies the possibilities of monitoring the degree of consolidation while a rock is subjected to external stresses. Due to the vast number of techniques available in the industry, most of them are very time-consuming methods and allow for many human and heterogeneity errors (Franquet & Abass, 1999; Josh et al., 2012; Nermoen et al., 2013; Omdal et al., 2009; Peksa et al., 2015; Qiao et al., 2012). For example, Ling et al. (2016) carried out a series of tests to measure the Biot coefficient using Bakken formation rocks. They used three promising techniques (bulk and matrix compressibility method, permeability-variation-with-pressure method, and constant deformation method) to evaluate the difference between them and to calculate absolute and relative errors. Despite the fact, they found constant deformation techniques more reliable; they also suggest that to have high-quality results all three methods must be implemented to avoid lab and human errors. To evade such complex procedures, we propose a unique and new methodology to calculate the Biot coefficient. This approach is based on images obtained through micro-CT scanning examinations of reservoir rocks, which enable us to acquire a large number of results in any direction. Thus, this method might be an ideal approach for anisotropic rock formations.

It can be supposedly evidenced that a body in a definite configuration *B* (body of the sample) is in mechanical equilibrium if the resultant force and resultant torque acting on any fixed point vanish for every subset of the body (Figure 32). The subsets may be considered solid and fluid. Therefore, the following two terms may be stated (Gonzalez & Stuart, 2008):

$$\mathrm{r}[\Omega_\mathrm{t}] = \int_{\Omega_\mathrm{t}} \rho(\mathrm{x},\mathrm{t})\mathrm{b}(\mathrm{x},\mathrm{t})\mathrm{dV}_\mathrm{x} + \int_{\partial\Omega_\mathrm{t}} \mathrm{t}(\mathrm{n},\mathrm{x},\mathrm{t})\mathrm{dA}_\mathrm{x} = 0 \tag{25}$$

$$\tau[\Omega_t] = \int_{\Omega_t} x \times \rho(x)b(x)dV_x + \int_{\partial\Omega_t} x \times t(n,x)dA_x = 0 \tag{26}$$

Where r and τ are resultant applied force and torque, respectively and $\rho(x,t)$ is showing density based on the variables of x (space) and t (time). The applied traction $t(n,x,t)$ depends on the unit normal vector n and $b(x,t)$ is the body force. Additionally, Ω_t indicates a subset of body B and $\partial\Omega_t$ is the surface of this subset. The volume element dV_x and the areal element dA_x converge with zero. By assuming a Cauchy stress field, equation 27 can be stated as:

$$t(n,x) = S(x)n \tag{27}$$

Where S (in this chapter denotes stress) stands for the Cauchy stress field and "n" denotes the unit length of the direction vector.

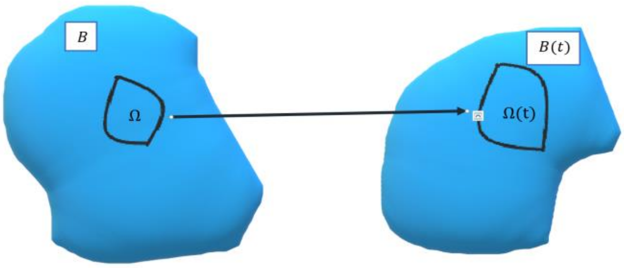

Figure 32: Evolution of a body and its subset. The left image shows the body at its initial equilibrium state, and the right image shows the deformed body at time t. The subset,Ω is a part of the body considered.

As shown in Figure 32, when the body undergoes deformation with time and points in the reference configuration B, denoted by X= (X1, X_2, X_3) will be transformed to the deformed configuration B', which we here denoted by x= (x1, x2, x3). This deformation may be mapped using a function $\varphi: B \to B'$ that maps each point $X \in B$ to a point $x = \varphi(X) \in B'$. The deformation gradient may be also used to quantify the strain, as in:

$$\text{“}F(X) = \nabla\varphi(X)\text{”} \tag{28}$$

Where $F(X)$ stands for the deformation gradient and $\nabla\varphi(X)$ is calculated and shown in equation 29:

$$\nabla\varphi(X) = \frac{\partial\nabla\varphi(X)}{\partial x}\vec{\imath} + \frac{\partial\nabla\varphi(X)}{\partial y}\vec{\jmath} + \frac{\partial\nabla\varphi(X)}{\partial z}\vec{k} \tag{29}$$

Here, $\vec{\zeta}$ is defined as the unit vector where $\zeta = x, y, z$. Equation 28 applies to the transformation of volume and surface integrals. Let $f(X,t)$ and $f(x,t)$ be arbitrary spatial functions defined on the configuration and its deformation, respectively. $g(X,t)$ and $g(x,t)$

are assumed to be arbitrary spatial second-order tensors on a specific body and its deformation (Gonzalez & Stuart, 2008), then:

$$\int_{\Omega_t} f(x,t)dV_x = \int_{\Omega} f(X,t)\det\big(F(X,t)\big)\,dV_X \tag{30}$$

$$\int_{\partial\Omega_t} g(x,t)n(x)dA_x = \int_{\partial\Omega} g(X,t)\det\big(F(X,t)\big)F(X,t)^{-T}\,N(X)dA_X \tag{31}$$

Where $N(X)$ represents the unit outward normal field on $\partial\Omega$. Hence, by considering the deformation and assumption of the Cauchy stress field, the resultant forces can be restated as follows:

$$\begin{aligned} r[\Omega_t] = \int_{\Omega} (\det F(X,t))\rho(\varphi(X,t),t)b(\varphi(X,t),t)\,dV_X + \\ \int_{\partial\Omega} (\det F(X,t))S(\varphi(X,t),t)F(X,t)^{-T}N(X)dA_X \end{aligned} \tag{32}$$

Here, the reference configuration and the deformed one can be expressed as a union of the solid subset and fluid subset.

$$B' = \Omega_{s(t)} \cup \Omega_{f(t)} \tag{33}$$

$$B = \Omega_s \cup \Omega_f \tag{34}$$

For an ideal fluid, the Cauchy stress field may be described using its pressure (Holzapfel, 2002):

$$S(x,t) = -p(x,t)I \tag{35}$$

Where P is fluid pressure expressed as a function of space and time and I is the identity matrix. Finally, the resultant forces for solid, fluid and the body are obtained and shown in equations 36, 37, and 38 as below:

$$\begin{aligned} r_s[\Omega_t] = \int_{\partial\Omega_s} (\det F_s(X,t))S_s(\varphi_s(X,t),t)F_s(X,t)^{-T}N_s(X)dA_{s_X} + \\ \int_{\Omega_s}(\det F_s(X,t))\rho_s(\varphi_s(X,t),t)b_s(\varphi_s(X,t),t)\,dV_{s_X} = 0 \end{aligned} \tag{36}$$

$$\begin{aligned} r_f[\Omega_t] = \int_{\partial\Omega_f} (\det F_f(X,t))p_f(\varphi_f(X,t),t)IF_f(X,t)^{-T}N_f(X)dA_{f_X} + \\ \int_{\Omega_f}(\det F_f(X,t))\rho_f(\varphi_f(X,t),t)b_f(\varphi_f(X,t),t)\,dV_{f_X} = 0 \end{aligned} \tag{37}$$

$$\begin{aligned} r_B[\Omega_t] = \int_{\partial\Omega_B} (\det F_B(X,t))S_B(\varphi_B(X,t),t)F_B(X,t)^{-T}N_B(X)dA_{B_X} + \\ \int_{\Omega_B}(\det F_B(X,t))\rho_s(\varphi_B(X,t),t)b_s(\varphi_B(X,t),t)\,dV_{B_X} = 0 \end{aligned} \tag{38}$$

Here, the subscripts *s*, *f*, and *B* represent the solid, fluid, and body, respectively. Taking into account equations 36, 37, and 38, as the resultant forces of solid (r_s) and fluid $\left(r_f\right)$ are equal to the resultant body force (r_f), and knowing that the source of a body force is mainly gravity, the summation of the body forces in fluid and solid is equal to body forces in the body. Hence,

$$\begin{aligned}&\int_{\partial\Omega_B}(\det F_B(X,t))S_B(\varphi_B(X,t),t)F_B(X,t)^{-T}N_B(X)dA_{B_X} = \\ &\int_{\partial\Omega_f}(\det F_f(X,t))p_f(\varphi_f(X,t),t)IF_f(X,t)^{-T}N_f(X)dA_{f_X} + \\ &\int_{\partial\Omega_s}(\det F_s(X,t))S_s(\varphi_s(X,t),t)F_s(X,t)^{-T}N_s(X)dA_{s_X}\end{aligned} \tag{39}$$

As the forces applied to the body are vertical here, the left side of the equation changes to equation 40.

$$\begin{aligned}&\int_{\partial\Omega_B}(\det F_B(X,t))S_B(\varphi_B(X,t),t)F_B(X,t)^{-T}N_B(X)dA_{B_X} = \\ &(\det F_B(X,t))S_B\left(\varphi_B(X,t),t\right)F_B(X,t)^{-T}A_B = S(x,t)A_B(t)\end{aligned} \tag{40}$$

From the fluid subset, the pressure acts vertically on the solid surface. Hence, it is possible to write;

$$\begin{aligned}&\int_{\partial\Omega_f}(\det F_f(X,t))p_f(\varphi_f(X,t),t)IF_f(X,t)^{-T}N_f(X)dA_{f_X} = \\ &(\det F_f(X,t))p_f(\varphi_f(X,t),t)IF_f(X,t)^{-T}N_f(X)A_{f_X} = p_f(x,t)IA_f(t)\end{aligned} \tag{41}$$

Therefore, it can be concluded that:

$$S(x,t)A_B(t) = \int_{\partial\Omega_s}(\det F_s(X,t))S_s(\varphi_s(X,t),t)F_s(X,t)^{-T}N_s(X)dA_{s_X} + p_f(x,t)IA_f(t) \tag{42}$$

Here, for convenience, equation 42 is re-stated and written as:

$$S(x,t) = S_{solid}(x,t) + \frac{p_f(x,t)A_f(t)}{A_B(t)} = S_{solid}(x,t) + \frac{p_f(x,t)(A_B(t)-A_s(t))}{A_B(t)} \tag{43}$$

In equation 43, the term defined by the ratio of the total area (A_B) minus the grains contact surface areas (A_s) divided by A_B is the Biot's coefficient as shown in equation 44.

$$\alpha = \frac{A_B - A_S}{A_B} \tag{44}$$

Essentially, the total stress (*S*) acts equally on all particles and pore space from every direction. Part of the total stress is carried by the fluid in the pore space. The remaining stress is carried through the grains, at their points of contact (particles surface contact points). The dashed line in Figure 33 represents a path where the grain-to-grain contact points carry the remaining stress. If we assume forces applied on the dashed line are vertically applied to the particle contacts, the sum of contact point areas A_S ($A_{1, 2, 3, 4, 5, 6}$) through the path over the cross-sectional area

A_C will be the resultant effective stress. Therefore, along with that path, the total stress (S) will be effective stress (S') added to the P_f. Consequently, the total stress will be;

$$S = S' + P_f \times (A_c - A_s)/A_c \tag{45}$$

Here, Biot's coefficient is the ratio of pore space occupied by brine (*Ac*-*As*) divided by the equivalent cross-sectional area (*Ac*). As in this study we are dealing with 2-dimensional calculation, the length area of contact surfaces will be substituted by the projected grain to grain contact length on its equivalent axis.

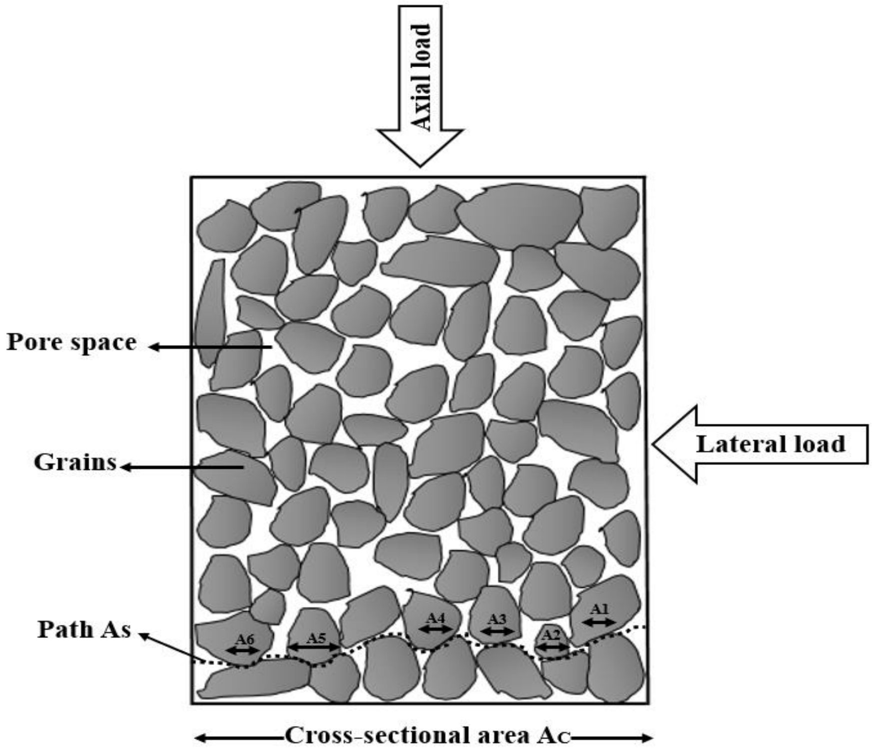

Figure 33: Schematic view of the grain's contact points and their lengths along the chosen path for Biot's effective stress coefficient calculation.

3.3 Experiment set up and procedure

3.3.1 Sample characteristics

Three different types of samples were chosen for a higher range of accuracy and comparison for this experimentation and their original 3D constructed micro-Ct images were recorded via Aviso software. The first sample used for this study is Bentheimer sandstone where the majority of contacts are bridged by cementation resulting in its homogeneity (Peksa et al., 2015). This specific formation has almost isotropic physical properties and is very porous and permeable (Yalaev et al., 2016). It is composed of quartz (wt 95%) with small quantities of

Kaolinite (wt 3%) and Orthoclase (wt 2%), with interconnected pores ranging from 50 to 500 µm (Klein et al., 2001) in size. By placing the 3.81 cm in diameter and 5.08 cm long sample into an AP-608 porosimeter-permeameter and applying various confining stresses up to 25 MPa, we were able to measure the porosity and air permeability versus effective stress. Porosity values ranged from 23.8 to 22.9%. Rock mechanical properties of the sample were also measured via triaxial tests, from which a Poisson's ratio and UCS (uniaxial compressive strength are 0.25 and 38.9 MPa respectively; Young modulus of 14.7 GPa was obtained elsewhere (Peksa et al., 2015; Roshan et al., 2016).

The next sample used for this study is Savonnieres limestone. This sample is cored from Eastern France and mainly contains porous Oolitic limestone (Fronteau et al., 2010). The petrophysical and material properties of carbonate samples are more unpredictable than those of sandstone samples. The main reason behind this is that the carbonate grains within the rocks tend to interact with the fluid both physically and chemically, which mainly changes the elastic properties of the rock. Therefore, it has a complex microstructure and is very heterogeneous. This carbonate is composed of two main minerals of calcite (wt. 97%) and biotite (wt. 3%) (Zhang et al., 2018).

The porosity measured for this sample ranged from 28 to 31% (Mikhaltsevitch et al., 2014). The last sample tested was cored from the Harvey-3 well, which is drilled in the SWH area. Rock mechanical properties of the several identical Savonnieres sample were also measured, the UCS ranged between 11 and 16 MPa and Young modulus of 13 and 14.5 GPa.

Table 10: Porosity of Bentheimer sandstone, Savonnieres limestone, and Harvey Sandstone sample under different confining effective stresses.

Effective stress (MPa)	Bentheimer	Savonnieres	Harvey
5	23.771	29.294	0.131
10	23.592	29.252	0.128
15	23.45	29.193	0.121
20	23.373	29.156	0.115
25	23.192	29.106	0.091

As it will be explained in the numerical simulation section in chapter 4, the Harvey area is the target formation for carbon dioxide injection in the SWH area. This is an important geological foundation for the Harvey project as it is the likely zone of carbon dioxide injection. This formation has previously been the subject of several studies to understand its depositional setting, distribution, and porosity/permeability. Harvey sandstone is cored via Harvey-3 exploration well from Wonnerup Member of the Lesueur Formation which contains quartz (wt 73%), calcite (wt 3%), kaolinite (wt 13%), and K-feldspar (wt 11%). The average porosity measured for the Harvey sandstone sample chosen for this test ranged between 9 to 13% tested by (Glubokovskikh et al., 2015). Table 10 summarizes the porosity of the chosen three samples for this study against different effective stresses (Lebedev et al., 2017; Mikhaltsevitch et al., 2014; Nourifard et al., 2020; Zhang et al., 2017).

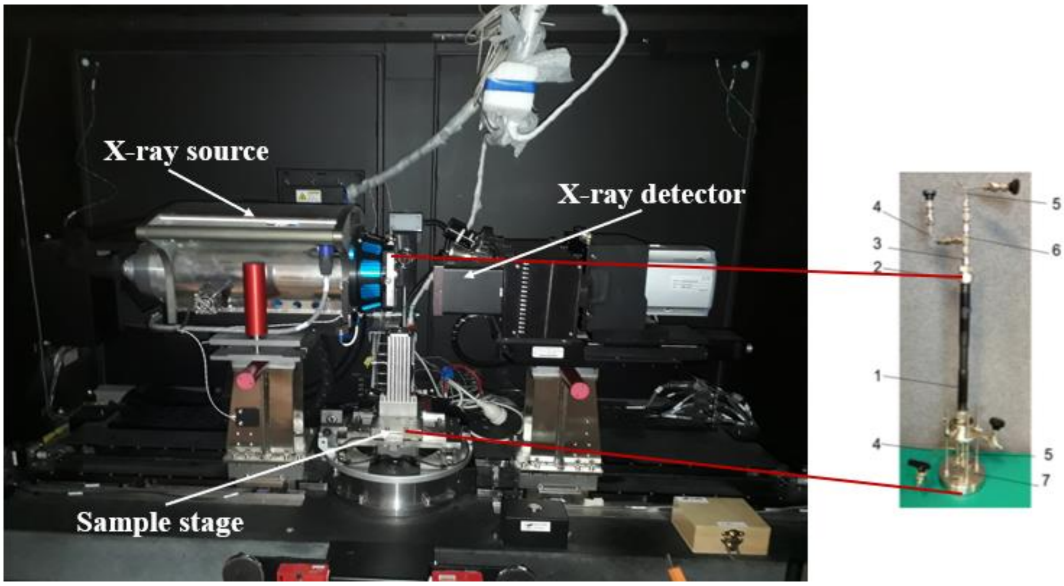

Figure 34: Micro-ct flooding setup and pressure cell for 5 mm cylindrical sample; transparent pipe (1), nut with ferrule (2), unions (3), confining stress input line (4), pore pressure input line (5), tees union (6) and sample stage to be fixed (7).

3.3.2 XRCT and image analysis

XRCT approach is a technique (non-destructive) that allows the acquisition of high-resolution 3D images of the interior of the rock, also at reservoir conditions (Lebedev et al., 2017). For this study, a very tiny core (5 mm diameter by 10 mm length) is cored and placed inside the X-ray transparent micro-CT cell (Figure 34), which is integrated with a core-flooding system that can be subjected to the pre-defined confining and pore pressures. Note that the micro-CT cell is capable of maintaining high pressure (45 MPa) and high-temperature (80 °C) conditions (Zhang et al., 2017). X-ray scanning is performed with the “3D X-ray microscope VersaXRM 500 (XRadia-Zeiss)”, with a beam energy of 60 keV under 20 MPa confinement pressure and 14 MPa pore pressure.

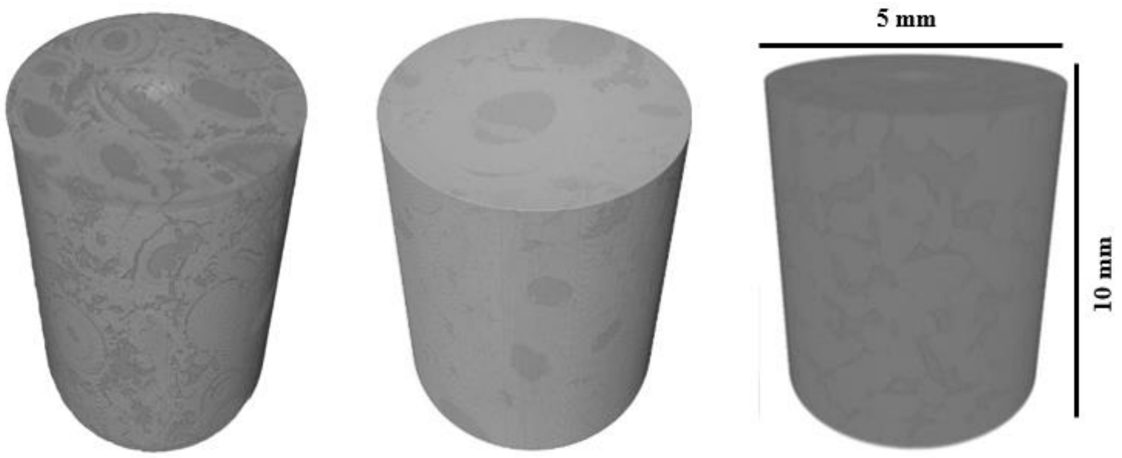

(a) **(b)** **(c)**

Figure 35: Original 3D constructed Micro CT image of Savonnieres limestone (a), Harvey sandstone (b) and Bentheimer sandstone (c).

A total number of 5001 radiographic images were acquired for each sample and reconstructed into a 3D volume with the internal Zeiss-XRadia software (Figure 35). The 3D volume is comprised of 972 × 1012 × 1007 voxels with a resolution of 1.59 µm. The obtained 3D volume was subjected to image analysis with Avizo Fire 9.5 software (FEI Thermo Fisher Scientific). The Non-Local Means filter module has been applied to the constructed 3D volume to reduce noises and remove image artefacts (Huang et al., 2014). The watershed algorithm was then implemented to perform image segmentation applying Roshan et al. (2016) techniques to separate grains from the pore space (Figure 36a).

(a) **(b)** **(c)**

Figure 36: 3D tomographic volume of Bentheimer sandstone; raw 3d volume with the labelled grains with skin effect(a), segmented 3D volume (b), cropped and grains labelled cubic volume (c).

In the sequence, a 3D binary image showing the grain's locations and the contacts was attained, and individual grains were separated from each other using the “separate objects” module and labelled with a unique ID (Figure 36b). Subsequently, the contacts between the grains were segmented using the “label interfaces” module. This procedure allows the segmentation of individual grain contacts so that their geometry can be analysed. The segmented volume was cropped (X = 600 × Y = 600 × Z = 800 pixels) to remove cone-beam artefacts and to obtain a cubic volume (Huang et al., 2014). It also helped to cut the non-clear images at the end/top of each side and to have a rectangular prism of the 3D volume. The cropped image was labelled to locate the position of each grain (Figure 36c) in order to calculate the contact interfaces and the projected length on the adjacent axis.

In order to calculate Biot’s coefficient, a set of 2D images sliced through different planes (XY, XZ, and YZ) were extracted. Figure 37a represents slice number 500 on the XY plane within the 3D volume of the entire grain’s interfaces. Figure 37b also shows the entire slices chosen for this study (orange lines). Once the 2D image had been extracted using the extraction module, by applying the label analysis module, we could measure the projected length of the grain’s contact on an equivalent axis. In addition, the best and most parallel paths to the adjacent axis amongst the vast number of available paths have been selected and manually drawn. Meanwhile, the selection of non-parallel paths had no impacts on the results as only the projected length and directions are measured for calculations. Therefore, the coefficient of Biot is the ratio of the subtraction of cross-sectional length or the length of the parallel axis (L_C) from projected interfaces length along the chosen path (L_B) over the cross-sectional length (Equation 46).

$$\alpha = \frac{L_C - L_B}{L_C} \tag{46}$$

As an example, the systematic procedure for the acquisition of the Biot’s coefficient of Bentheimer is given below for slice 500 in the XY plane (Figure 37).

- Grains contact area (length) are manually calculated and obtained by performing an arithmetic module via Aviso. Noting that, the best and most parallel paths to the adjacent axis are chosen amongst the vast number of available paths. Each contact length has its unique ID and length.

- The bounding box of the object and each grain's contact points (length) were extracted using the "label analysis" module. The label analysis generates an individual index number for each line and its related bounding box length in any directions.
- The length of the projected contact's length is calculated for each line (path).
- The position of the lines is chosen and drawn manually considering they should cover the whole length of the sample.
- Sensitivity analysis on the number of the lines and their positions to ensure Biot does not change more than 9 % when a new line (S) with a random position is (are) added.
- Then, Biot's coefficient was calculated along each of these lines (dotted white lines (X1, X2, X3, Y1, Y2, and Y3) in Figure 37c).
- Each line goes through specific contact lines and the total effective area of the path was recognized. Using the total bounding box of path X1 (summation of the projected length of grain's interfaces) and the cross-sectional area of the path (the number of voxels (600) in X direction multiplied by pixel resolution (1.59 μm)), we calculated α using equation 28.

Table 11 summarizes Biot's coefficient calculation for the Bentheimer sandstone sample for the slice 500 on the XY plane and Z direction.

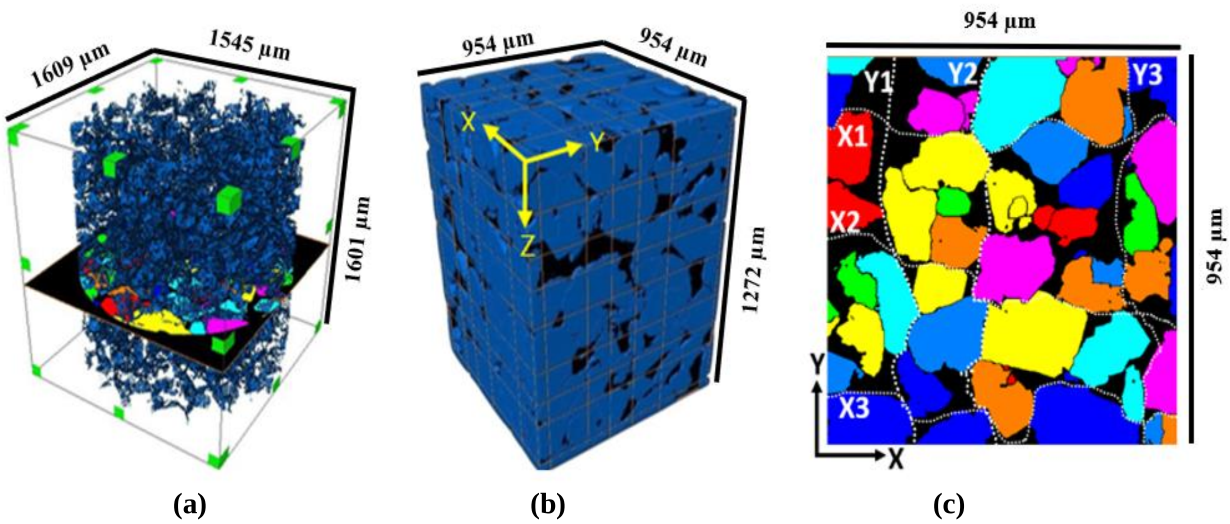

Figure 37: Schematic view of entire chosen slices of Bentheimer sandstone sample (a), 3d schematic view of slice 500 within grains surfaces inside the cubic frame (b) and slice 500 through the XY plane showing the paths (dotted white lines) chosen for the calculation of the Biot coefficient (c).

Table 11: Summary of Biot's coefficient calculations for the slice 500 on the X-Y directions (Bentheimer sandstone).

Path direction ID	X1	X2	X3	Y1	Y2	Y3
Projected contact length (μm), L_B	315.5	182.3	240.9	163.3	249.9	183.9
Cross-sectional length (μm), L_C	954	954	954	954	954	954
Biot's Coefficient	0.67	0.80	0.74	0.83	0.69	0.81

3.4 XRCT implementations and results

Eight slices on the XZ, XY, and ZY planes were randomly chosen to calculate Biot's coefficient with a total of 144 paths. The histogram of Biot's coefficient for the planes XY, XZ, and YZ and each direction are plotted and illustrated in Figure 38, Figure 39 and Figure 40. Note that Biot's coefficient may vary in different directions (He et al., 2016). The average calculated Biot coefficient for Savonniers limestone is 0.54 with a standard deviation of ± 0.19, Bentheimer sandstone is 0.69 with a standard deviation of ± 0.09, and Harvey sandstone is 0.78 with a standard deviation of ± 0.12.

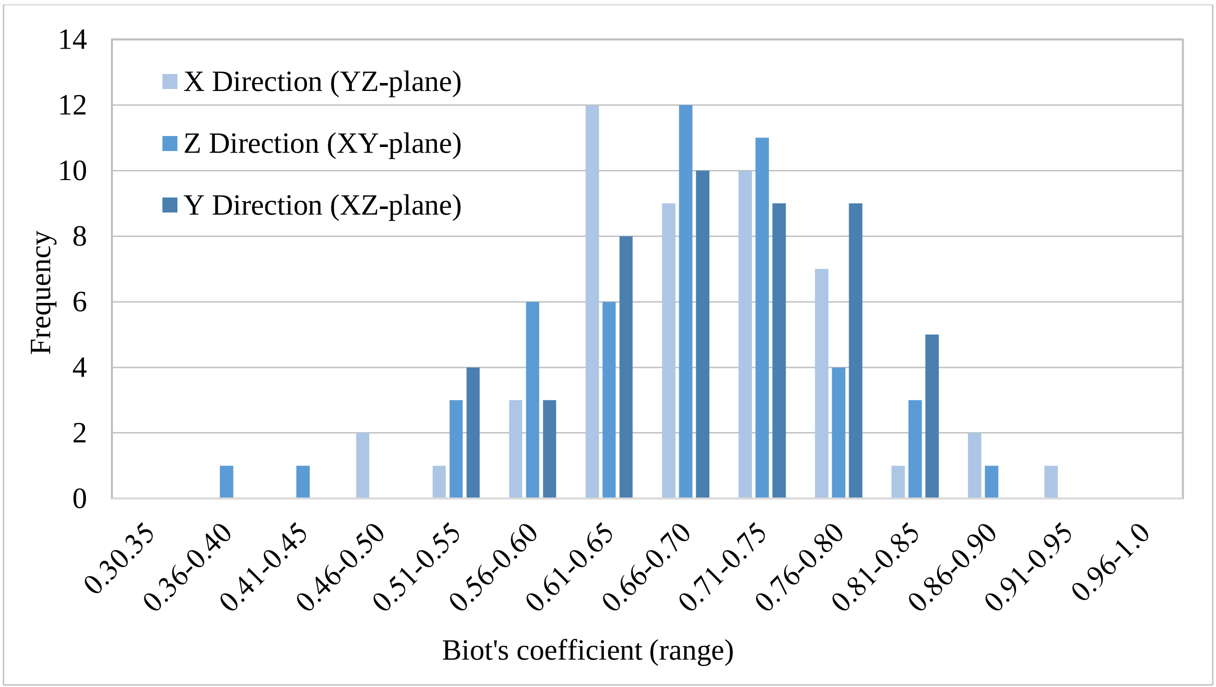

Figure 38: Histogram of entire Biot's coefficient results for 48 slices in each direction for Bentheimer sandstone for all slices and 144 individual paths in all directions.

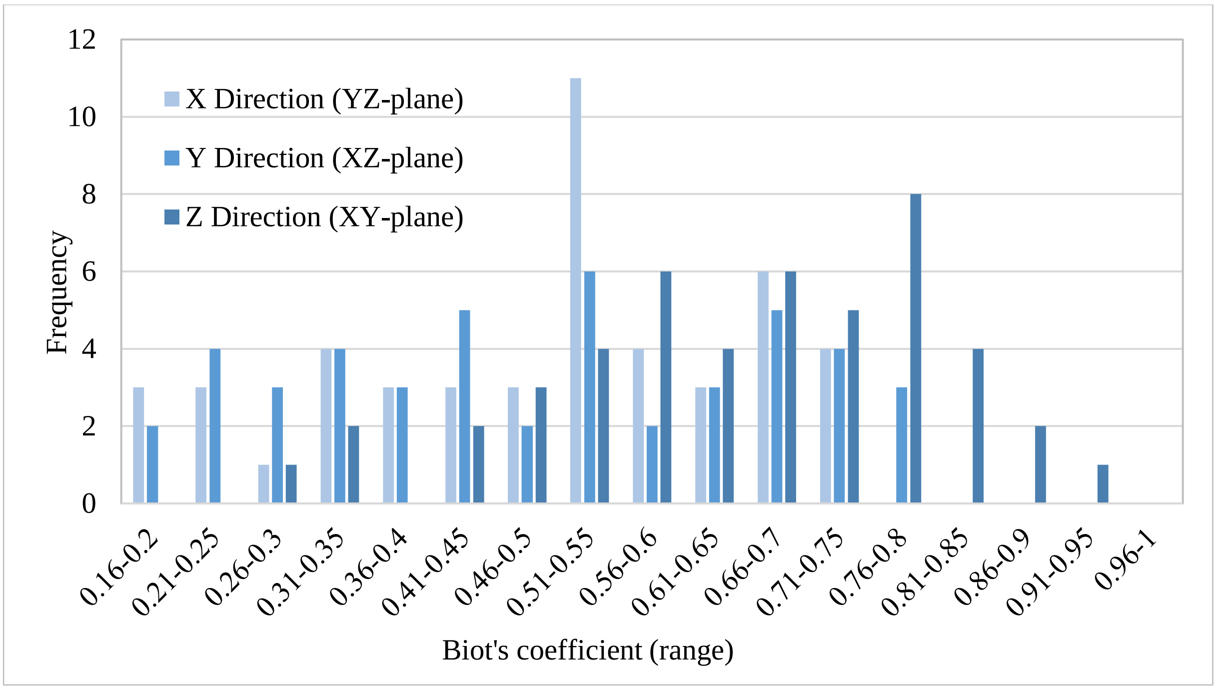

Figure 39: Histogram of entire Biot's coefficient results for 48 slices in each direction for Savonnieres limestone for all slices and 144 individual paths in all directions.

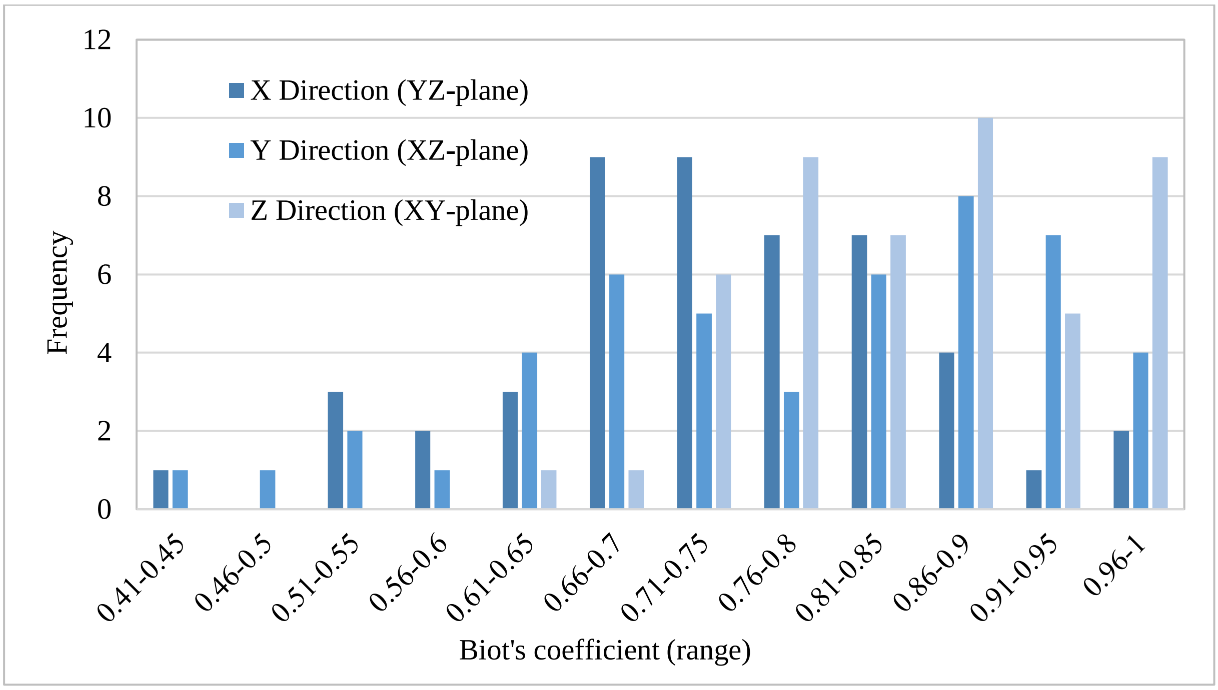

Figure 40: Histogram of entire Biot's coefficient results for 48 slices in each direction for Harvey sandstone for all slices and 144 individual paths in all directions.

It is seen from three histograms along with different directions that the mean values along different direction across many 2D tomographs are very similar. For the Bentheimer sample, the higher number of the results are in the range of 0.65 to 0.8 in the Y direction, 0.65 to 0.75

in the Z direction and 0.6 to 0.8 in the X-direction. For the Savonnieres sample, the most frequent results are between 0.5 and 0.6 for all directions. Also, for the Harvey sample, the higher number of the results are in the range of 0.75 and 0.9 in the Y direction, 0.81 and 0.9 in the Z direction and 0.65 and 0.8 in the X-direction.

There is slight microscopic anisotropy of the Biot’s coefficient amongst slices is observed It is clear that the porosity values have a great impact on the results as lower porosity resulted in higher Biot’s value which is in agreement with similar investigations (Blöcher et al., 2014; van Dalen et al., 2010). Slight microscopic anisotropy of the Biot’s coefficient amongst slices is observed. Very slight variation as mentioned before is believed to be linked to the image resolution.

3.4.1 Laboratory validation applying hydro-mechanical tests

To validate the image processing results, we have carried out the laboratory investigation applying the constant deformation technique on Bentheimer sandstone and Savonnieres limestone for comparison. Figure 41 and Figure 42 show the laboratory outcome. As shown in the micro-CT section 4.3, there is a strong agreement between the average calculated Biot’s coefficient for the Bentheimer sample in the 3D directions (i.e., average Biot’s coefficient for the planes XY, XZ, and YZ are 0.68, 0.69 and 0.7, respectively) and the experimental (0.69) result. A similar trend has also been seen for Savonnieres limestone where under approximately 20 MPa confining stress the constant deformation laboratory result (0.52) matches the image analysis (i.e., average Biot’s coefficient values for the planes XY, XZ and YZ are 0.45, 0.67, and 0.49, respectively).

In regards to image analysis and referring to what identified in this study, Biot’s coefficient is acquired by measuring fluid to solid contact surface length by the total cross-sectional area when projected on an arbitrary plane. Therefore, the quality of the images and accurate estimation of particle contact surfaces as well as choosing the correct path are the main parameters to be dealt with in this technique.

Despite some microscopic scale anisotropy throughout the chosen paths, the average value appears to be consistent. This is due to the consolidation degree of the grains while under external forces and internal fluid pressure. This highlights the capability of the technique to not only estimate the Biot coefficient but also to recognize its anisotropy at multiple scales. Consequently, when the same sample with the same mechanical, petrophysical properties, and similar test condition (*Pc* = 20 MPa, *Pp* =14 MPa) is tested in the laboratory (constant volumetric technique), the results match very closely. Although the representative volume for micro-CT analysis is very small (5 mm by 10 mm) comparing to the experiment's specimen (diameter 38 mm and length 64 mm), the results match very well. Related to other proposed techniques, our direct technique requires future validation and repetition for any further commercial use.

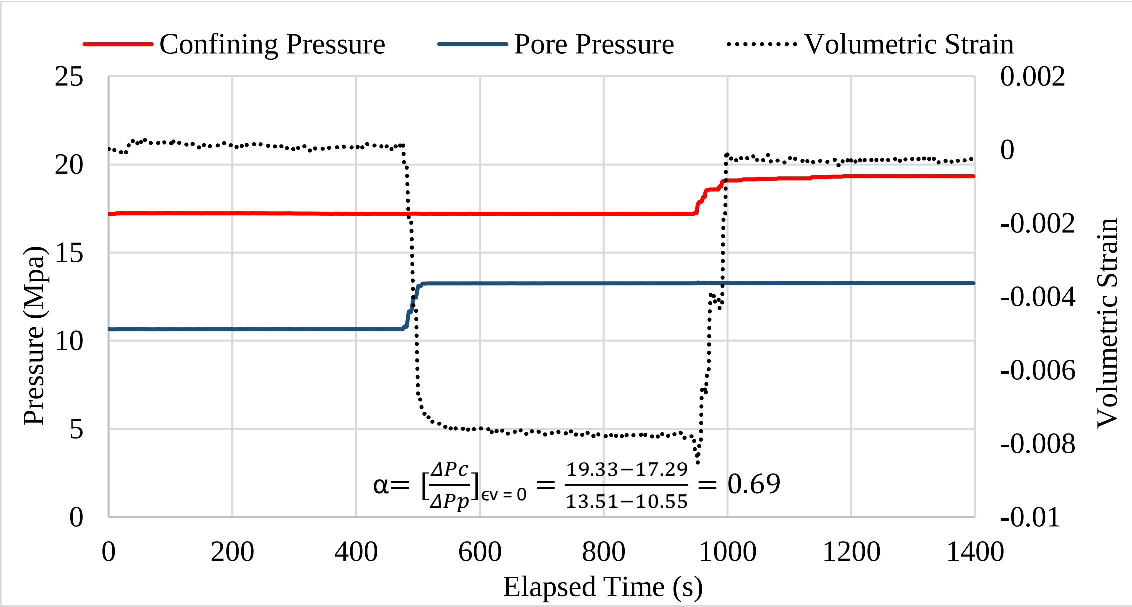

Figure 41: Parameters measured in the zero-constraint deformation experiment on Bentheimer sandstone specimen.

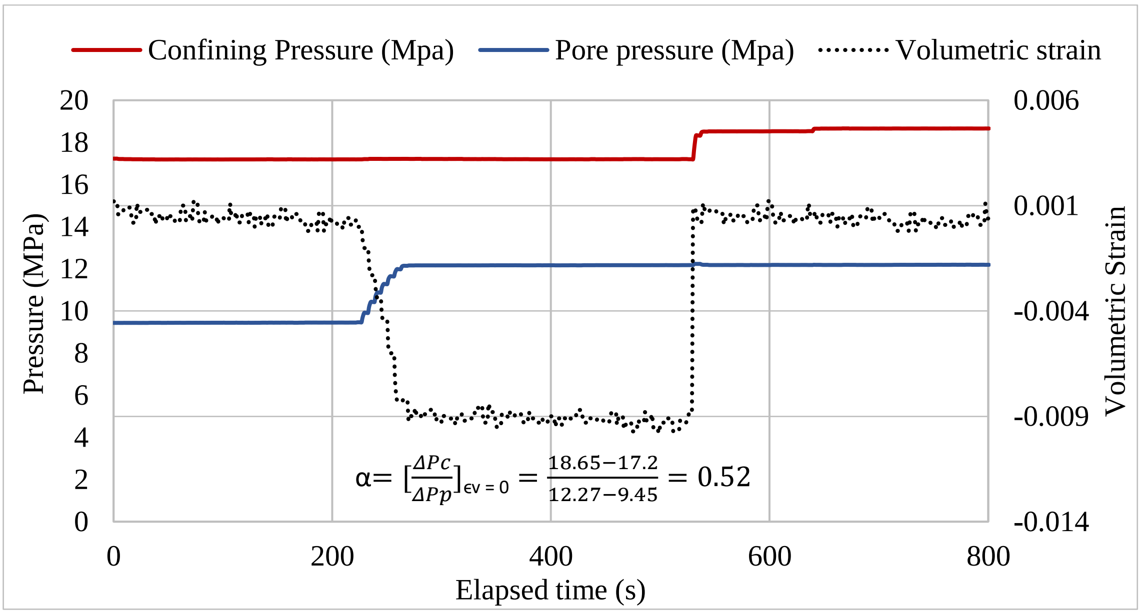

Figure 42: Parameters measured in the zero-constraint deformation experiment on Savonnieres limestone specimen.

3.4.2 Micro-CT validation using unconsolidated sand

In order to assess the performance of our technique, it is considered the higher limit of the Biot's coefficient where it approaches unity and becomes Terzaghi effective stress. An unconsolidated sand pack underwent external load and imaged using XRCT. For this investigation, we managed to collect beach white sand from Esperance city located in the south of Western Australia which consists of mostly quartz and grain size of 106 to 256 µm (Ahmed & Lebedev, 2019). As stated by Ahmed and Lebedev (2019) the porosity of the sand pack ranged between 39 % and 0.42 % and the Klinkenberg corrected permeability that we measured ranged from 7200 mD to 7380 mD. They also supplied us the CT-scan images of the sand pack which was placed in the rubber sleeve of the CT cell with 10 mm length and 5 mm diameter and stressed to 25 MPa for the scan. Similar to the procedure explained for the sandstone sample, the Biot coefficient was calculated along a different direction at different slides.

To capture images, we first dried the sample and then apply a confining pressure of 25 MPa. The apparatus for this test is the same as the one used for other specimens explained in section 3.3 (Figure 34). Straight after images are captures with the help of Avizo Fire 9.5 software (FEI Thermo Fisher Scientific) the 3D image of the entire sample was formed as it is shown in Figure 43a. Once we constructed the 3D volume, segmentation (Figure 43b) and labelling (Figure 43c) is applied to the volume to see the status of the grain contacts interfaces.

To be able to calculate the Biot's coefficient via applying equation 46, the cross-sectional length (L_C) of the 2D extracted image is required along with the length of the chosen path length (L_B) in any direction. Therefore, the 3D cylindrical volume is cropped (Figure 44a) and few 2D images (slices) in all directions were extracted. To manifest the calculation vividly, slice 482 in the XY plane is shown within the entire 3D volume grain's interfaces as shown in Figure 44b along with slice 482 in XY direction which is presented in Figure 44c.

As shown in Figure 44c and randomly drawn paths of X1, X2, Y1, and Y2 there is little contact being observed within the grains, therefore, the projected bounding length will be zero. Minimal contact was identified between grains showing that the Biot coefficient (using equation 46) returns 1.0 i.e., L_B is negligible. This is intuitive as the Biot end effect in Terzaghi law is 1.0 for samples with no skeleton (soil). The results from our image analysis, therefore, agree well with the Biot coefficient of 1.0 for unconsolidated materials. Consequently, in soil mechanics, it is only pore pressure that affects the state of stress. Applying the micro-CT technique to directly measure Biot’s coefficient hence, is a novel and trustworthy approach for future investigation and also toward accurate estimation in three orthogonal directions.

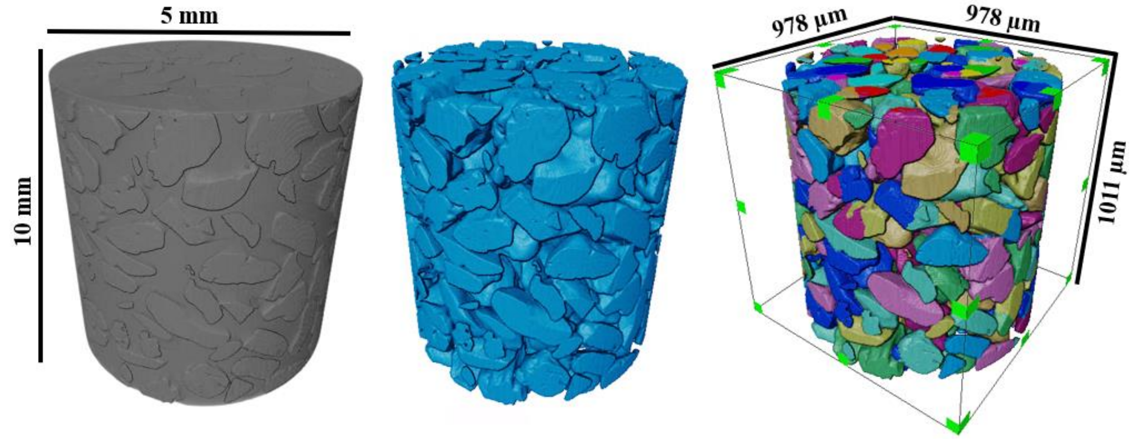

(a) **(b)** **(c)**

Figure 43: Raw rendered image of Esperance sand (a), segmented (b) and grains labelled 3d volume (c)

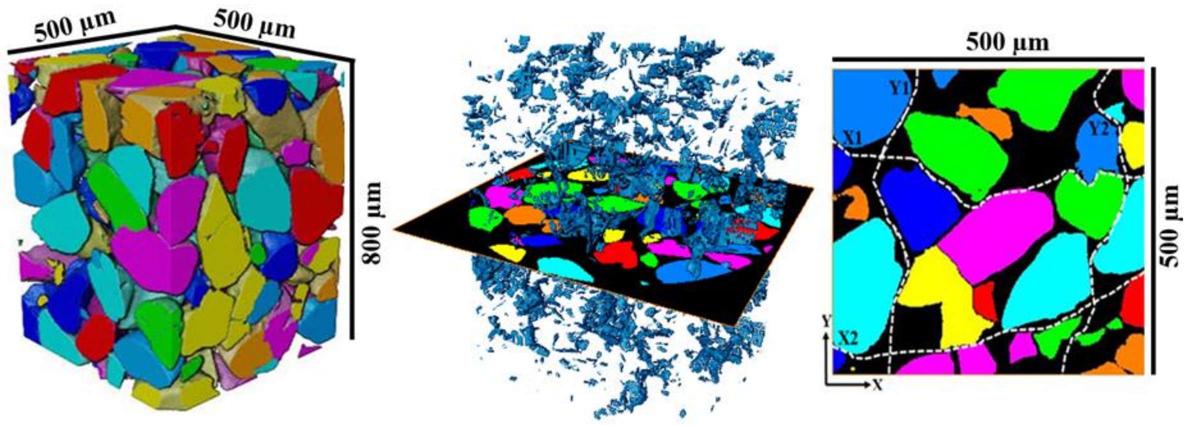

(a) **(b)** **(c)**

Figure 44: The cropped and labelled 3d volume (a), slice 482 from XY plane within grain’s interfaces (b), and the randomly and manually chosen paths for the Biot’s coefficient calculation on slice 482 in the XY plane (c).

3.4.3 Discussion

In this work, a new application (image processing technique) is presented associated with laboratory validation. The micro-CT tests were carried out in hydrostatic conditions with pore pressure and confinement stress under no stress anisotropy. Three different types of homogeneous and isotropic samples were chosen to maximize the similarities between the micrometre and centimetre scales. Concerning image analysis and referring to what here is identified, the coefficient is calculated by measuring the length of fluid to solid contact area by the total cross-section area when projected onto an arbitrary plane. Therefore, the quality of the images and accurate estimation of particle contact surfaces as well as choosing the correct path are the main parameters to be dealt with in this technique. We managed to select the suitable paths visually considering the free movement of the fluid through grain particles. Once the constructed 3D volume is processed, we divided our result into three planes (XY, YZ, and XZ). Moreover, in each randomly chosen slice, three paths were picked to monitor the variation of the Biot coefficient. In each plane, a total number of 64 paths from 8 slices (each slice 3 paths) were gone under detailed calculation. In the XY plane, for instance, the minimum value of 0.42 (path X2 in the slice 600 on the XZ plane) and the maximum value of 0.89 (path Y3 in slice 400 and 300 on the YZ plane) has been calculated. This is due to the position and the size of the grains along with the chosen path. For example, in slice 500 the path Y1 is going through a smaller number of grains which corresponds to a less projected contact length of 163.29 μm and resulting in a greater Biot coefficient (0.83).

Different planes and paths also have shown similar variations. Notably, various experimental studies have shown it to be true that the Biot coefficient is mainly dependant on the physical properties of the rocks (porosity, permeability and grain sizes) (Ingraham et al., 2017). Despite some results indicating differences throughout the paths, the average value appears to be relatively constant. This is due to the consolidation degree and the deposition status of grains while under external forces and internal fluid pressure. Surprisingly when the same sample with the same mechanical, petrophysical properties, and corresponding test conditions (confinement hydrostatic stress of 20 MPa and pore pressure of 14 MPa) is tested in the laboratory (constant volumetric technique), the results match very well. Although the representative volume for micro-CT analysis is very low (tiny sample) compared to the experiment’s specimen (diameter 38 mm by length 64 mm), the results are in good agreement. Similar to other new techniques, our approach requires future validation and repetition for any further commercial use.

Hence, this new technique opens up the possibility of measuring Biot’s coefficient relatively quickly and accurately in any direction. Due to time limitations, we were unable to perform laboratory validation on Harvey sandstone, but the outcome of this research presents a great new possibility to expedite the test procedure with less labouring cost and techniques and also superior results in terms of accuracy. In fact, the external force has a large impact on the results.

As the laboratory tests (zero-constraint technique) were performed applying 20 MPa confining load, for better validation the micro-CT images were taken under the same pressure. The laboratory test is a very time-consuming process and at this stage, we are not able to perform the tests again. Various external loads are also recommended for better clarification and justification.

3.5 Conclusions

In this chapter, we performed different sets of poroelastic experiments on high permeable and quartz-rich Bentheimer sandstone, Savonnieres limestone, and Harvey sandstone. In contrast to other experiments, where there was a need to execute different types of experiments for better estimation of the Biot coefficient, our approach provides a fast and straightforward technique.

We measured the Biot coefficient in different directions via micro-CT image analysis. The microtomographic visualization of the grain contacts inside the specimen under certain confining and pore pressure enabled us to acquire thousands of high-quality images. Subsequently, these images were processed to calculate the grain contact's surface areas along an arbitrary path. For this study, we have gone through all three planes from 8 slices and overall, assessed 144 paths. Note that, Biot coefficients were then compared with the experimental results. In the experimental approach (since the preliminary focus was on the mean stress, internal pressure, an accurate estimation of volumetric strain), we only subjected the specimen to hydrostatic conditions, varying the *Pp* and the *Pp* while we managed to maintain zero volumetric strain constraints.

According to the outcome of our investigation for Bentheimer sandstone and Savonnieres limestone with laboratory validation, the Biot coefficient calculation yielded a similar average value in different 3D directions; namely, the Biot coefficient was estimated at 0.69, and 0.54 respectively which was surprisingly close to the average value of the micro-CT results. The presented analysis emphasizes that micro-CT results can successfully provide precise values for Biot's coefficient.

In order to validate the results of the analytical method (chapter 1), the effect of poroelasticity, Biot's coefficient and the pore pressure/stress coupling will undergo investigation using real case study on the carbon sequestration project. As the assumptions of the analytical method have limitations, especially in terms of the reservoir shape, the numerical simulation could lead to more sophisticated results. chapter 4 will now address the numerical approach to poroelasticity via finite element methods (FEM). It will also consider both the numerical (FEM) and analytical method on the carbon storage project on the southwest hub (SWH) reservoir field in Western Australia. The analytical method will be employed to assess some of the results obtained from the numerical investigation.

Chapter 4

4. Analytical/numerical geomechanical evaluation of the South West Hub Western Australia

4.1 Introduction

This chapter reviews the fault characterization, stress regime and geomechanical investigations in regards to the South West Hub (SWH) area which is located in Western Australia as a potential target reservoir for carbon dioxide injection and storage applications.

The main goal is a detailed investigation of the existing faults within the field to grasp an understanding of their tendency, to assess whether it is a suitable target reservoir for carbon dioxide capture and storage plans. The numerical approach is adapted from the end report of the ANLEC Project with the title of "Potential for preferential flow through faults and fractures"(Urosevic et al., 2019). This report is publicly available and accessible through https://anlecrd.com.au/projects/potential-preferential-flow-faults-fractures.

"Potential for preferential flow through faults and fractures" presents a combination of seismic and geological studies on the Harvey area and specifically Harvey 3 well (Urosevic et al., 2019). This report was prepared via Curtin University and CSIRO and submitted to the ANLEC group in January 2019 and the thesis author was involved in the numerical (geomechanical) analysis section. This report mainly covers fault characterization, stress regime and geological and geomechanical investigations in regards to the SWH area. The core goal of this project is a detailed and cohesive investigation of the fracture network and existing faults within the field to grasp an idea of their tendency to act as suitable target reservoirs for carbon storage applications. Numerous authors have theoretically and physically evaluated the possibilities of executing carbon sequestration application in the recent decade (Cao et al., 2020; Foulger et al., 2018; Hawkes et al., 2004; Streit & Hillis, 2004; Wang et al., 2019). Within the energy sector, there have been several pieces of research together with field experiences such as acid gas injection and gas storage in saline formations. Currently, carbon store and underground storage (CCS) is carried out by many operation companies. In order to locate the potential field for CCS, it is vital to have satisfactory geological models to run numerical simulations to analyse how carbon dioxide injection behaves in the subsurface. This type of injection model needs to be simulated to ensure reliable storage integrity during the injection phase together with a prediction of future environmentally risk-related issues.

4.2 South West Hub (SWH)

The SWH is situated in the Harvey area, south of Perth in Western Australia. Four exploration wells have been drilled and cored into the SWH area to evaluate the lithology and mineralogy of the possible reservoirs for carbon dioxide sequestration. At first, in early 2012, Harvey-1 drilled, and then in 2015 the last three wells drilled with the acquisition of cores for further laboratory experiments. The Lesueur sandstones are the dominant form of the most drilled area. Harvey-1 completely fully penetrated the sandstone formations and the remaining exploration wells reached above the base of the Lesueur sandstone (Sharma et al., 2017). The Lesueur is divided into two members, known as being "Yalgroup" and "Wonnerup", with a thickness of approximately 550 to 800 m. Harvey-1 well has entirely drilled to Wonnerup with nearly 1500 thicknesses (Figure 45). The Sabina formation is the deepest mapped formation in the SWH area and only Harvey-1 well managed to reach it. Compared to other members, it has fewer faults and it is moderately homogenous. The Wonnerup formation is the thickest and most faulted unit with a thickness of over 1400 m. Similar to Sabina formation, only Harvey-1 well entirely penetrated to the full depth of the formation. The upper Lesueur member is the Yalgroup which is mainly formed with claystone with a thickness of 700 m (ODIN, 2016).

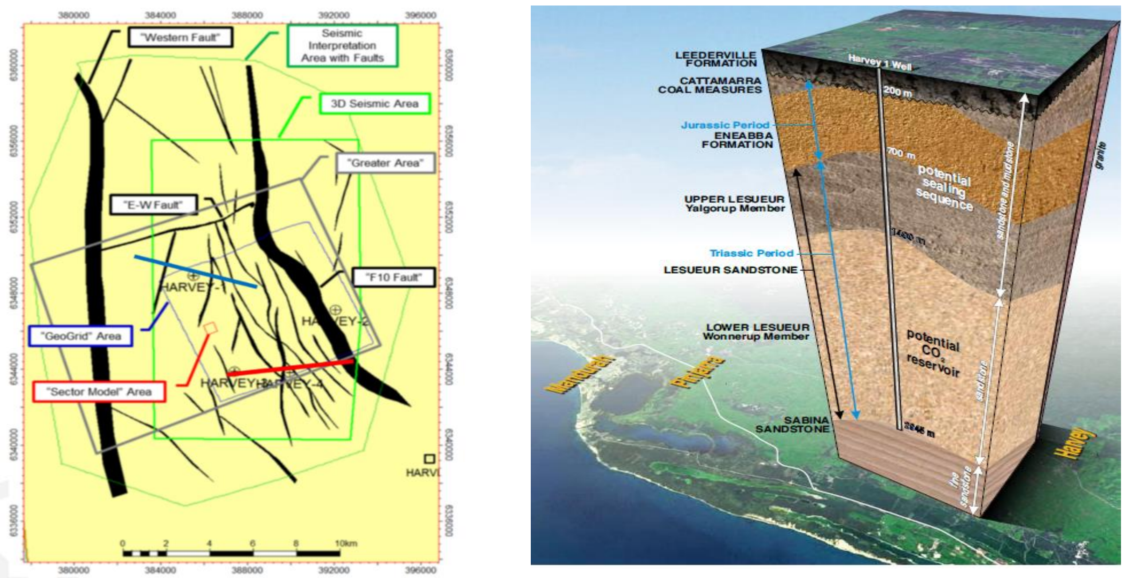

Figure 45: Grey frame highlighted is the study area (Left), onshore southern Perth Basin stratigraphy: Harvey-1 well (Right) (ODIN, 2016).

4.3 Numerical Approach

In chapter 1, the analytical poroelastic model of Rudnicki (1986) was used to illustrate the coupling evolution when gas is injected into a poroelastic full space. The analytical modelling was also used to address the coupling variation by the time in a normal fault regime. In case analytical investigation becomes too complex or validity is required, a numerical approach (finite element method) is taken into consideration. The methodology of the FEM analysis is based on the continuum model subdivided into tiny elements (which is consists of nodes). The FEM is a specific (iterative) numerical solution to solve restricted differential equations for each element. The resolution of the FEM and the element size are the main factors for the better accuracy of the solutions (smaller elements results in better resolution). In this case, the commercial software called Abaqus was used as it provides fully coupled pore pressure and stress analysis, which will be discussed in the first part of this chapter. Abaqus is also used to evaluate the fault reactivation risks of the SWH area and to examine the poroelastic behaviour of rocks (coupling) for a long-time injection procedure (CCS). All the sources and information for the numerical investigation were originally from the reservoir model, which was initially built using SKUA-Gocad 2017 (Figure 46) together with the static and dynamic models which were built using Petrel and CMG respectively. The mechanical and physical properties in terms of the geological storage models are collected from the previous related researches (Langhi et al., 2015; Y. Zhang, L. Langhi, et al., 2015)

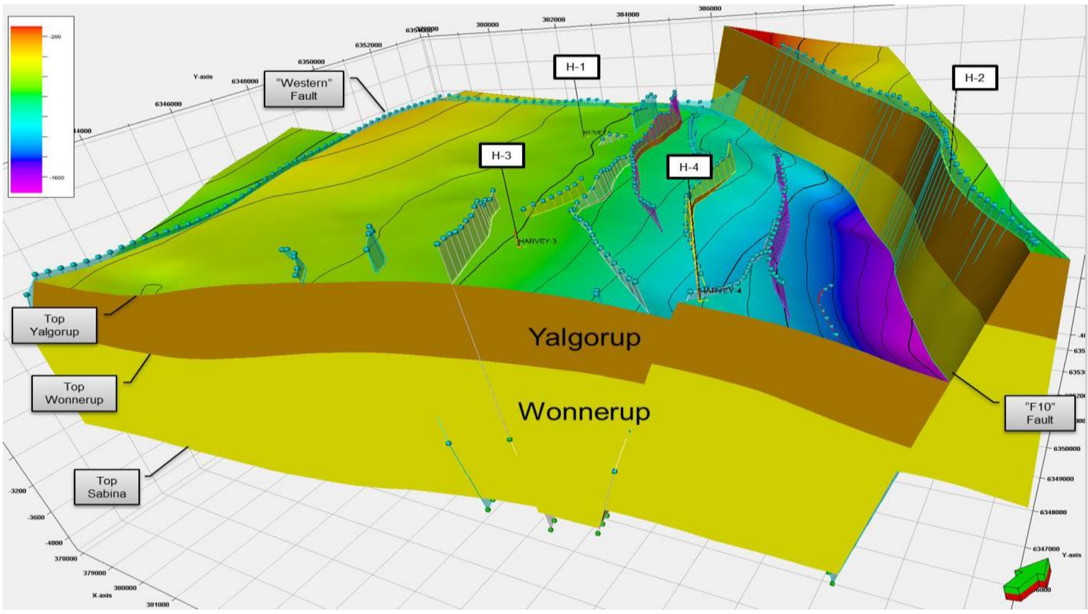

Figure 46: Structural model with well locations in each of the formations-From ODDIN Static model of the Harvey field (ODIN, 2016).

4.3.1 Numerical analysis steps

In this study, a numerical analysis based on the finite element method is taken into account using the software Abaqus. The most time and labour-consuming phase in building a geomechanical FEM model are building the reservoir geometry. To do this, lithostratigraphic horizons and fault surfaces are constructed via seismic interpretation. The research procedure mainly relies on the new advanced feature offered by SKUA-Gocad, which lets us generate and export the geometry models with different boundary conditions, type of mesh, and some other properties that could be used by Abaqus for the mechanical analysis. To generate a geomechanical model, faults and horizons data in the format of surface and interpretations are imported to SKUA-Gocad from the Petrel model (static) built by ODIN in 2016 for the SWH area (the core of the geomechanical model). We also used the CMG dynamic models prepared ODIN to import pore pressure values to SKUA-Gocad geomechanical model (Urosevic et al., 2019). To generate the geometry model, the structural and stratigraphy (SS) workflow is considered by taking on the faults, horizons, and wellbore data exported from Petrel (Figure 47). The SS workflow describes the geological layers, boundaries, and model geometry.

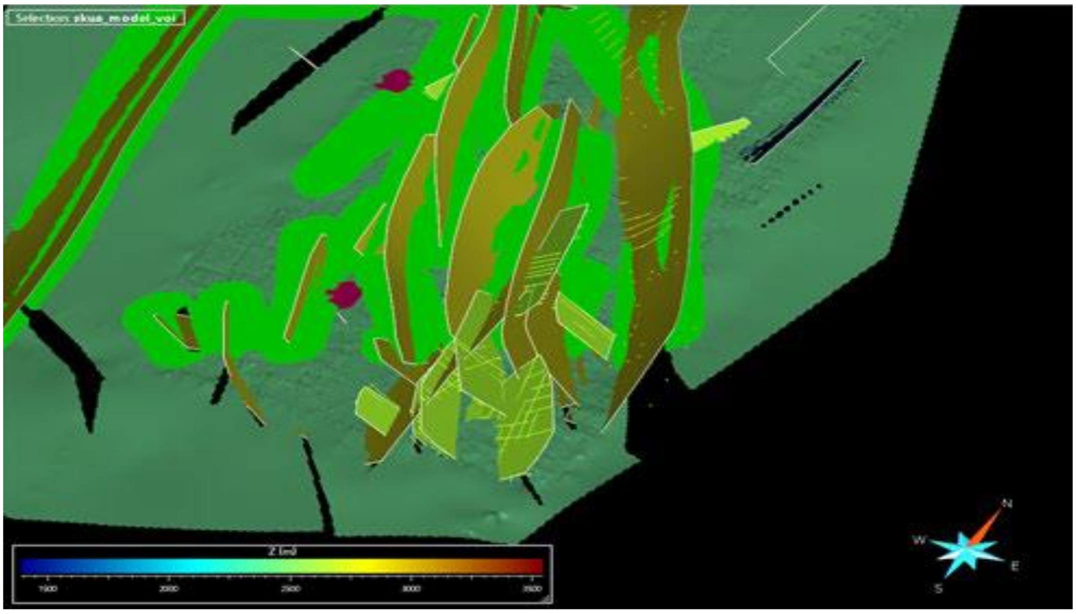

Figure 47: Petrel faults and horizons acquired from the petrel model (ODIN, 2016).

Once the model geometry is built as described above, the FEM workflow is used to generate tetrahedral mesh compatible with Abaqus necessities. However, horizons, as well as fractures in the FEM model, are characterized by zones or regions of the elements. In fact, reservoir geometry has to be reconstructed maintaining the geometrical difficulties of the underground reservoir formations. Therefore, for the numerical analysis and representing faults and horizons to the model and also to simplify the meshing process, they are defined as regions where each of them has its own petrophysical and petrochemical properties (Delle Piane et al., 2017). Therefore, only the fault and horizons surfaces are used to accomplish mesh requirements for the simulation.

4.3.2 Model regions and properties

As it has already been published by Urosevic et al. (2019), two scenarios are proposed to analyze the faults reactivation risks as a result of the CCS project. Perceptibly, once the geomechanical model is being built, the main regions (eight regions) of the model are defined (Figure 48). To define the faults in the tetrahedral model, each fault is defined with apportioned thickness, mechanical behaviour, and distance between the model nodes. Delle Piane et al. (2017) estimated width of 70 m for the fault zones. For over-burden, side burden, and under-burden, the parameters are assigned according to the properties of their dominant formation. These properties are mainly the values assumed by Y Zhang et al. (2015).

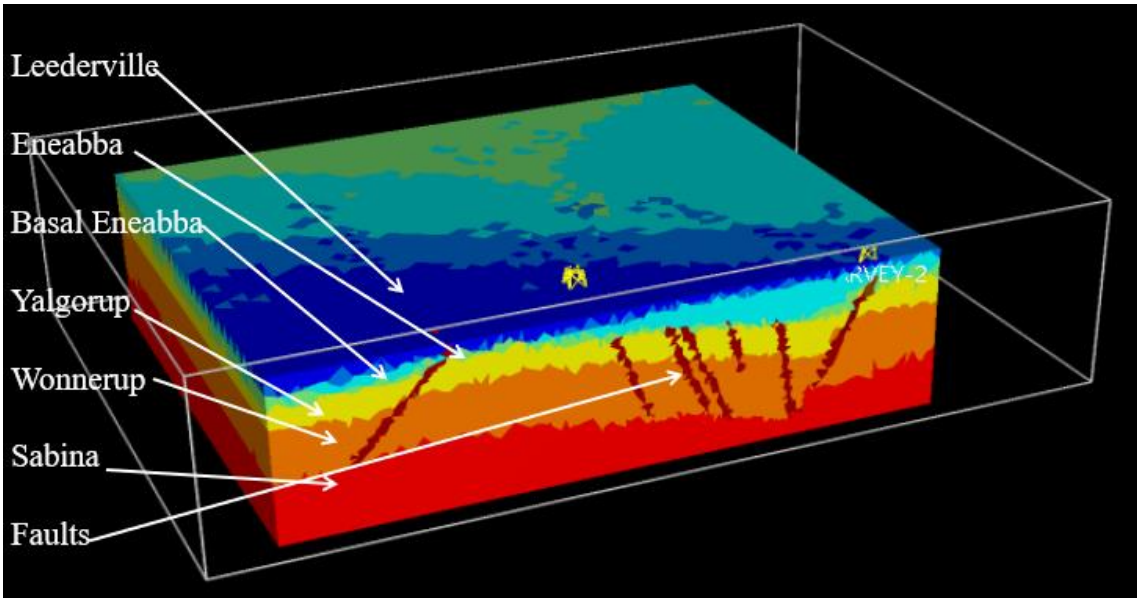

Figure 48: The model regions (Urosevic et al., 2019).

From the CMG dynamic model prepared by ODIN in 2016, the porosity distribution has been exported and populated to the surrounding area in the geomechanical model. The pore pressure values as previously mentioned are taken from the CMG model and interpolated into the reservoir region (Pervukhina et al., 2017). In order to evaluate every aspect of the modelling process including uncertainties regarding faults properties and geometries, two modelling scenarios were introduced and constructed for the numerical analysis. Mechanical and petrophysical properties for each scenario are collected and acquired through the previous related studies as shown in Table 12 and Table 13 with proposing two separate scenarios for the current study (Delle Piane et al., 2013; Pervukhina et al., 2017; Rasouli et al., 2013; Timms et al., 2012). The difference between the two scenarios is highlighted in red and the main difference taken into consideration is the properties of the faults (Urosevic et al., 2019).

Table 12: Scenario 1 for numerical analysis (Urosevic et al., 2019).

Region (Scenario 1)	Density (Kg/m3)	Young's modulus (GPa)	Poisson's ratio	Cohesion (MPa)	Void Ratio	UCS (MPa)	Permeability (m^2)	Friction angle (◦)
Above Leederville	2265	14	0.26	3.1	0.1364	20.2	1.00E-15	22
Leederville	2265	14	0.26	3.1	0.1364	20.8	1.00E-15	22
Eneabba	2300	14	0.26	3.1	3.5	20.8	4.50E-18	22
Basal Eneabba	2125	24	0.35	2.6	0.15	8.2	3.50E-16	22.5
Yalgorup Member	2300	7.9	0.23	5.8	0.01	12.9	1.43E-13	10.8
Wonnerup Member	2450	16.1	0.21	15.5	0.14	50.7	1.43E-13	26.6
Sabina Sandstone	2500	20	0.20	8.8	0.17	50.7	4.50E-18	30
Fault	2125	20	0.35	2.6	0.01	5.2	4.50E-18	30

Table 13: Scenario 2 for numerical analysis (Urosevic et al., 2019).

Region (Scenario 2)	Density (Kg/m3)	Young modulus (GPa)	Poisson's ratio	Cohesion (MPa)	Void ratio	UCS (MPa)	Permeability (m^2)	Friction angle (◦)
Above Leederville	2265	14	0.26	3.1	0.136 4	20.2	1.00E-15	22
Leederville	2265	14	0.26	3.1	0.136 4	20.8	1.00E-15	22
Eneabba	2300	14	0.26	3.1	3.5	20.8	4.50E-18	22
Basal Eneabba	2125	24	0.35	2.6	0.15	8.2	3.50E-16	22.5
Yalgorup member	2300	2.1	0.22	5.8	0.01	12.9	3.45E-16	10.8
Wonnerup Member	2450	16.1	0.21	15.5	0.14	50.7	1.41E-13	26.6
Sabina Sandstone	2500	20	0.20	8.8	0.17	50.7	4.50E-18	30
Fault	2125	40	0.30	28.0	0.01	5.2	4.50E-18	30

4.4 Numerical analysis and results

The workflow of the Abaqus analysis consists of pre-processing, importing input files, run analysis, quality control investigation, post-processing, and exporting the results. Prior to importing input files (from SKUA-Gocad), the pre-processing stage involves defining initial model conditions, material properties, and state of stress. Pore pressure initial values and void ratios are already included in the geomechanical model and exported from SKUA-Gocad, so they do need to be added at this phase. The run analysis stage includes defining the time step and nature of the analysis. The period of analysis for each phase is based on the CMG dynamic model as well as initial, maximum, and minimum time increments. Once all the parameters are manually defined and after arranging each phase, the pore pressure values supplied by SKUA are linked with each parameter. Once the run analysis stage is completed, the results of pore pressure, stress, and deformation evolution for a specified period are exported and interpreted.

The key goal of this study is to identify the variation of *Pp* and mean stress for a period of before, one month, and 1000 years after carbon dioxide injection at chosen points. Also, it sets out to verify the coupling impact on the existing faults in Yalgroup and Wonnerup members. The initial stress condition, *Pp* and physical properties for the two formations are summarized in Table 14 (Pervukhina et al., 2017).

Table 14: Petrophysical properties and stress data of two target formations for the CCS project (Urosevic et al., 2019).

Formation	Depth (m)	σhmax (MPa)	σhmin (MPa)	σv (MPa)	Pp (MPa)	Friction coefficient
Yalgorup	1300	35.2	24.1	27.7	13.2	0.6
Wonnerup	1700	51.8	31.4	37.1	17.3	0.6

Based on the model size and the capability of the simulation outcomes, four referential points were selected to verify the evolution of *Pp*, yield occurrence and mean effective stress and for the stated time steps. Wonnerup formation near Harvey-1 well, Yalgroup formation near Harvey-4 well, Eastern and Western faults are the referential points.

4.4.1 Pore pressure evolution results

Table 15 illustrates the measured end values of *Pp* changes as a result of carbon dioxide injection within the predefined time-steps. It shows that there are no significant *Pp* changes in either scenario within all referential points. For all members, near Harvey-4 and Harvey-1 well the pore pressure changes display no considerable variations with the time. This verifies that the reservoir faces an insignificant pressure drop in 1000 years after injection which appears to be trivial for the stability calculations. A similar trend occurs in eastern and western faults with no considerable pore pressure variation.

Table 15: Pore pressure changes in the beginning, 1 month and 1000 years of injection.

Pore pressure (MPa)	Before	1 month	1000 years
Wonnerup unit (Scenario 1)	16.39	17.38	17.44
Wonnerup unit (Scenario 2)	16.4	17.38	17.44
Yalgroup unit (Scenario 1)	14.57	13.69	13.58
Yalgroup unit (Scenario 2)	14.57	13.8	13.72
Western fault (Scenario 1)	11.55	12.16	12.21
Western fault (Scenario 2)	11.55	12.16	12.21
Eastern fault (Scenario 1)	24.56	25.17	25.25
Eastern fault (Scenario 2)	24.57	25.17	25.24

Table 16: Effective stress changes at the referential point within four observation points before injection, 1 month, and 1000 years after injection.

Mean effective stress (MPa)	Before	1 month	1000 years
Wonnerup unit (Scenario 1)	22.51	22.11	22.07
Wonnerup unit (Scenario 2)	21.18	20.81	20.77
Yalgroup unit (Scenario 1)	22.48	22.47	22.47
Yalgroup unit (Scenario 2)	19.48	19.48	19.48
Western fault (Scenario 1)	19.76	19.27	19.24
Western fault (Scenario 2)	31.69	30.92	30.89
Eastern fault (Scenario 1)	45.5	45.51	45.51
Eastern fault (Scenario 2)	48.09	48.06	48.05

4.4.2 Mean effective stress evolution results

As can be seen from Table 16, there is no considerable effective stress variation is observed in our four referential points. In Wonnerup formation and near Harvey-1 well, the mean effective stress in both scenarios faces a slight drop, whereas in Yalgroup formation near Harvey-4 well there is no variation is observed. Similarly, neither fault around the target reservoir look as if to encounter no mean effective stress changes.

4.4.3 The occurrence of yield analysis

No occurrence of yield is verified at our chosen referential point (near Harvey-1 well in Wonnerup formation and near Harvey-4 well in Yalgroup formation), considering two scenarios. Also, at our referential points, no plastic failure is seen by the stated planned injection volume and flow rate (Figure 49). The presence of yield is seen for a few elements on the edges of the 3D model. This possibly occurs due to model boundary settings, not the *Pp*.

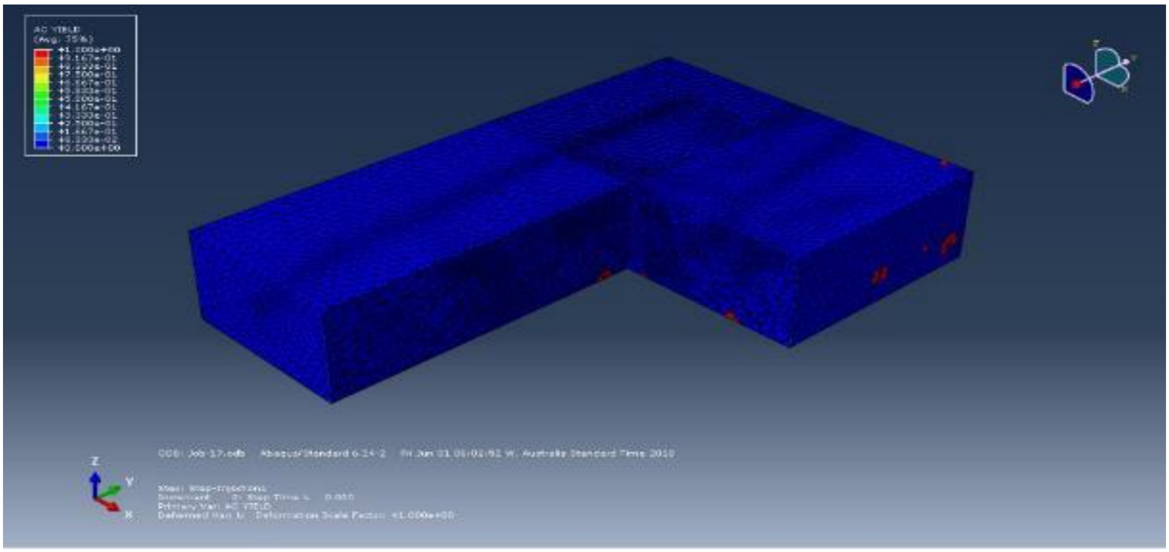

Figure 49: Yield occurrence at our chosen referential point (Urosevic et al., 2019).

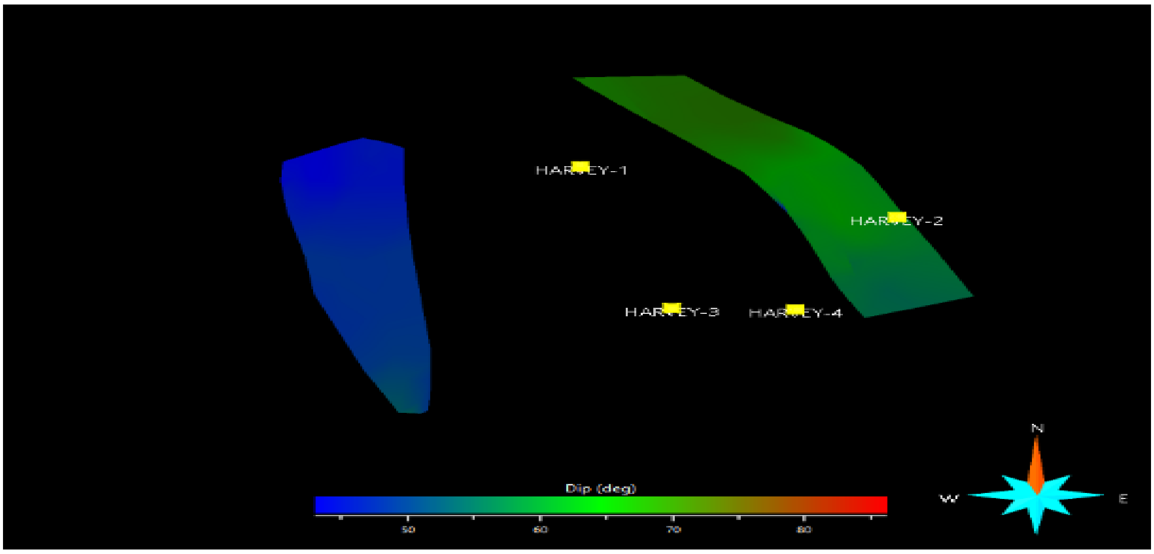

Figure 50: Distance and location of the faults (Western and Eastern faults) to the exploratory wells (Urosevic et al., 2019).

4.4.4 Estimating of fault reactivation as a result of poroelasticity

Here an attempt was made to analyse fault reactivation possibility in two referential points in the Western fault and Eastern fault as shown in Figure 50. According to the outcomes of the numerical investigation, only 40% of the injection pressure affects the effective stress on the two injection points.

Based on the calculation and considering the fault properties mentioned earlier in the two scenarios for weaker and stronger faults, and also knowing the strike-slip faulting regime is dominant in the SWH area, pore pressure is not increasing enough to reactivate the western fault. It is almost 10 times higher pore pressure needed to activate the Western fault. Considering the poroelastic effect (Biot's coefficient of 0.78) it is less possible that the fault could be reactivated as the size of the Mohr circle tend to be smaller and away from the failure envelope (Figure 51).

Applying the same analysis on the Eastern fault, it is extremely unlikely that the pore pressure evolution causes fault reactivation. It is nearly a pore pressure increase of 45 times the one is already calculated required to reactivate the fault. Considering the same poroelastic coefficient the same scenario happens as the western fault (Figure 52).

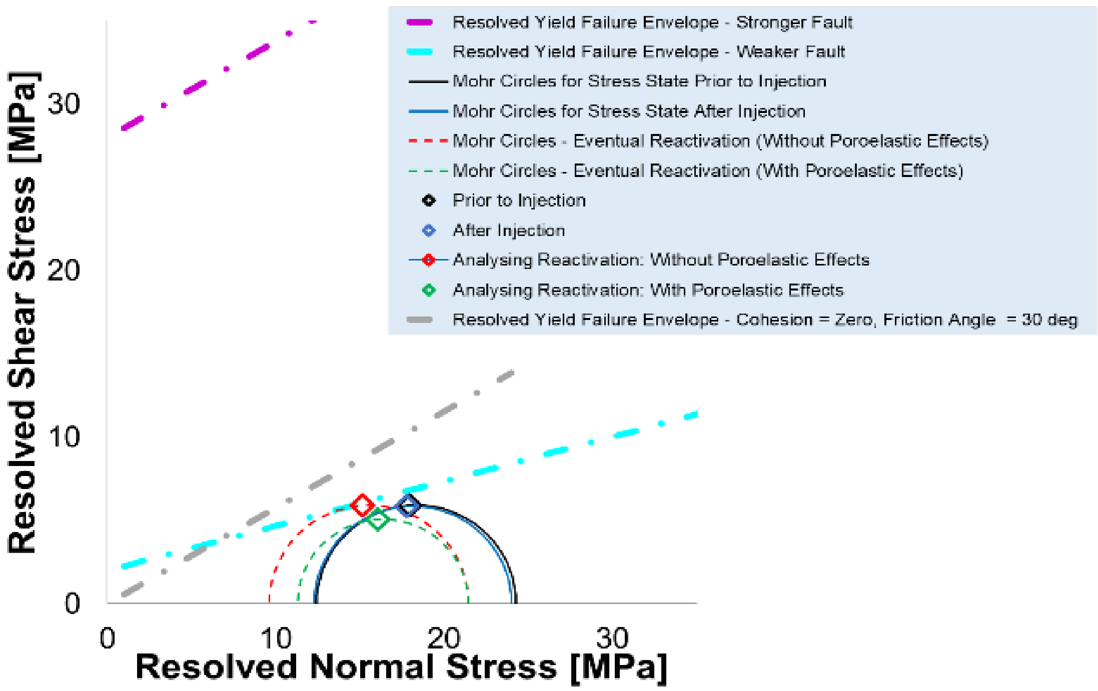

Figure 51: Main Western fault analysis on fault reactivation (Urosevic et al., 2019).

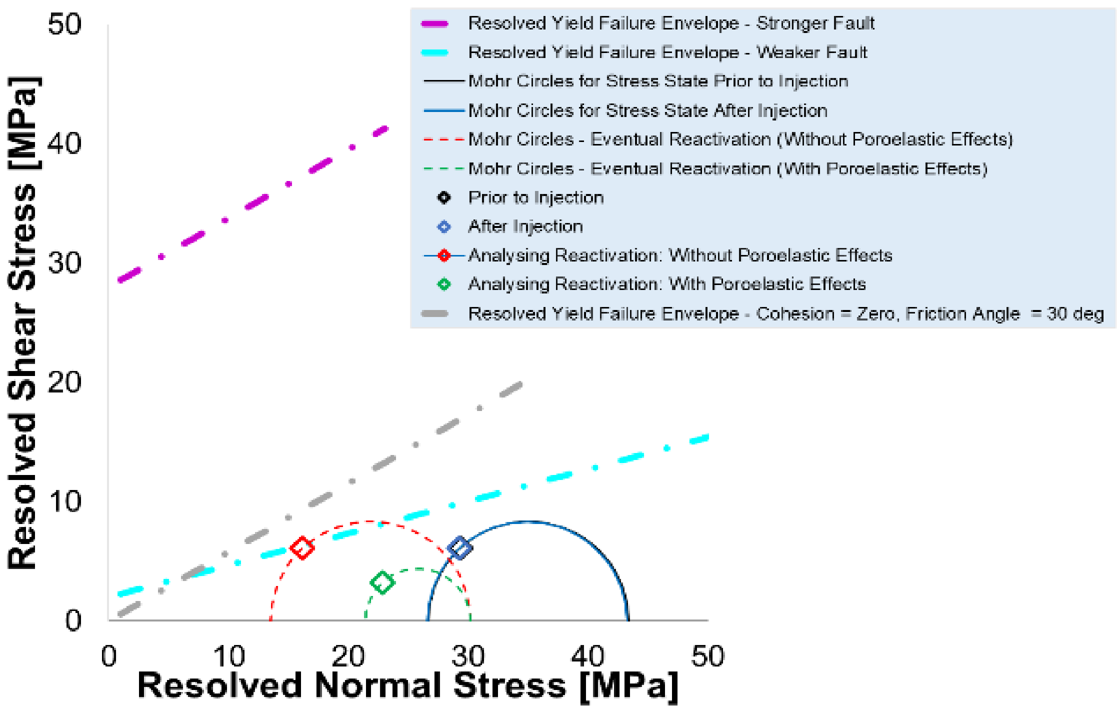

Figure 52: Main Eastern fault analysis on fault reactivation (Urosevic et al., 2019).

4.4.5 Findings

Based on the data available for this numerical investigation and the scenarios relating to the referential points, the findings confirm the minimum effect of *Pp* on the fault stability in the region as well as faults near chosen injection points. The significant finding relating to the yield occurrence outcome is that no spread of yield has been observed in the fault regions. Note that the chosen weak and strong fault properties for this investigation resulted in no significant deformation occurring in the model and the fault regions. The results also corroborate previous study results such as Smith et al. (2007) and the analytical results presented earlier in this report (Urosevic et al., 2019).

4.5 Analytical approach to SWH Project

The objective of this section is to analytically calculate the *Pp* and stress alterations (variation) due to carbon dioxide. Besides, the coupling between *Pp* and σh will be investigated along with its impact on geological stability. As discussed in chapter 1, the impact of *Pp* variation on the in-situ stresses depends greatly on the location of the injection points and the tectonic regimes. Therefore, in this part of the study, we will analytically validate the numerical results considering the coupling effect. Noting that, the analytical approach is for the time when one injection source is assumed or in the case of individual well effect is under investigation. We assumed two observation points located on Eastern and Western faults within the radius of 100 m in order to study the faults' reactivation possibilities. Additionally, we assessed how pore pressure and other stress components vary in both Wonnerup and Yalgroup formations concerning the observation's points. To show the evolution of *Pp*, two equations of Rudnicki (equations 14 and 15) will be used.

To better assess the link between carbon dioxide injection rates (*Q*) and the *Pp* evolution in the SWH area, the material properties similar to what has been used for the numerical modelling were selected. It is also considered the permeability of 100 mD in the Wonnerup and Yalgroup. based on Table 14 (stress data), the strike-slip stress regime is identified as the dominant stress regime in the region.

Table 17 shows the material properties used for the *Pp* and stresses calculations as well as coupling values. Consequently, ΔPp and radial/tangential stress changes will be plotted assuming the injection period (1000 years) for 100 m (*r*) from the referential point.

Table 17: Material properties applied for the fluid pressure and radial/tangential stress calculations.

Field injection rate (Tons/year)	**800,000**
Compressibility (m^2/s)	0.006
Dynamic Young modulus (GPa)	38.06
Number of wells	9
Poisson's ratio	0.2
Static Young modulus (GPa)	14.544
Fluid density (Kg/m^3)	1890
Biot's coefficient	0.78
Distance (m)	100
Injection period (years)	1000

4.5.1 Stress and fluid pressure distribution in Wonnerup member

This section investigates the temporal variation of *Pp* and σ in the Wonnerup member. Figure 53 shows the changes within 100 m from the injection origin. Straight after the opening of injection, σr starts to rise at the referential point, whereas for *Pp* and σt it takes longer to increase.

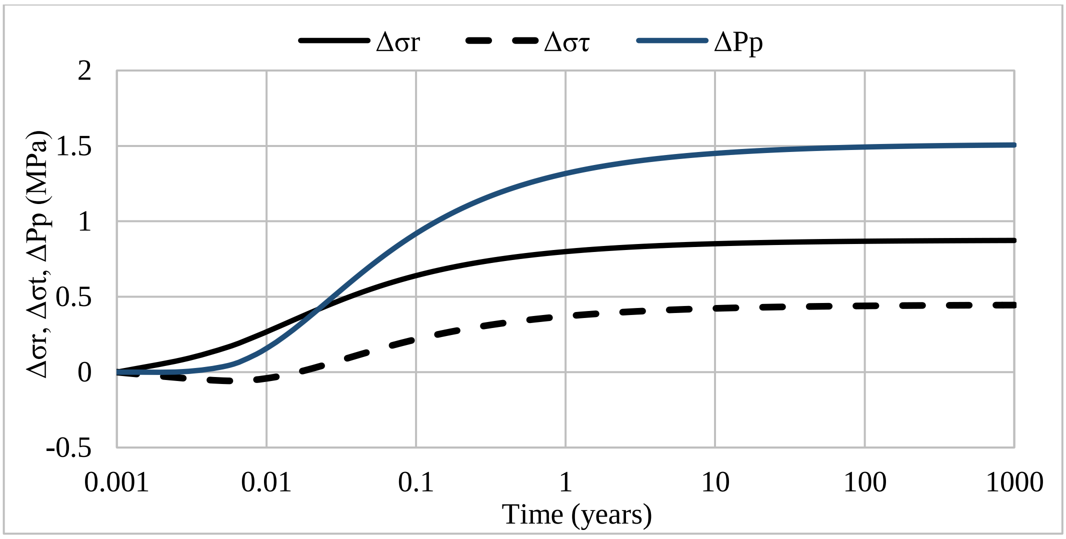

Figure 53: Fluid pressure and radial/tangential stress variation within Wonnerup formation for 1000 years after injection at a distance of 100 m from the injection point.

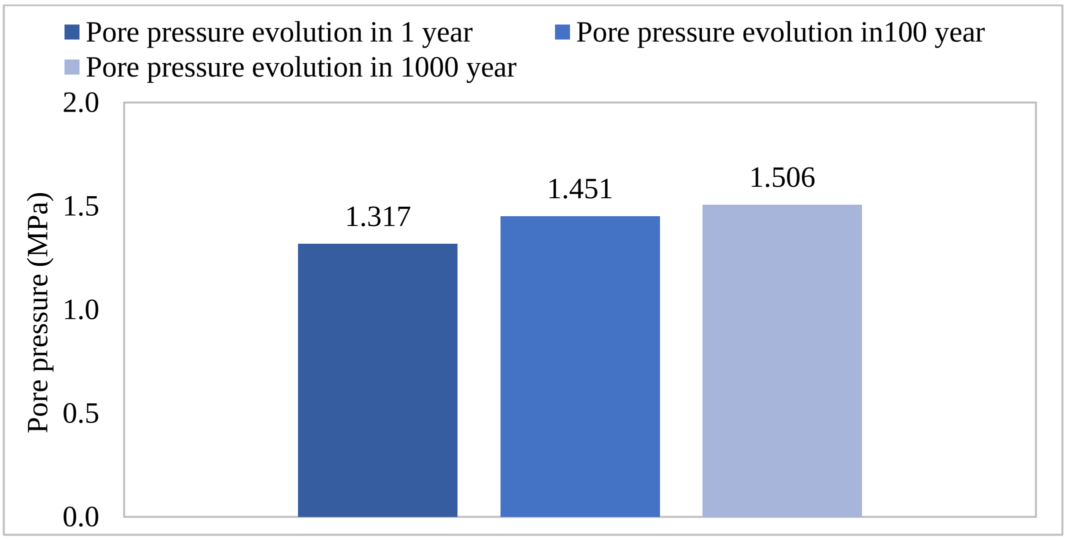

Figure 54: Pore pressure variation in 1 year, 100 years, and 1000 years within Wonnerup formation.

In fact, σr is increasing and diffusing by the inner structure of the porous medium whereas Pp is spreading out within the porous medium. Therefore, at the beginning of the injection period, $\Delta\sigma r$ is higher than ΔPp. Figure 53 shows that it takes 100 years for stress and Pp changes to become stable and for no significant changes to occur in time. The maximum ΔPp acquired in Wonnerup member is nearly 1.506 MPa (Figure 54) and $\Delta\sigma r$ and $\Delta\sigma t$ is 0.85 MPa and 0.48 MPa respectively. The coupling ratios are measured and is illustrated in Figure 55. When pore pressure starts to vary, more time is required than the other two stresses to reach the referential point; one year after injection the coupling values approach zero.

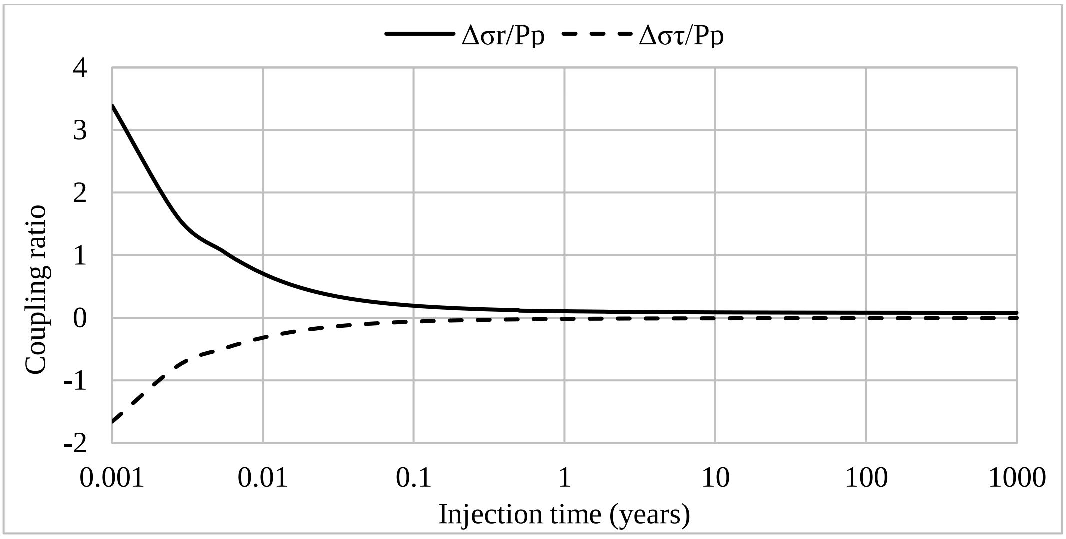

Figure 55: Coupling ratio for 1000 years after injection (Wonnerup formation).

4.5.2 Stress and fluid pressure distribution in Yalgroup member

The variation of pore pressure and stress in Yalgroup member was analysed (1300 m deep) and a referential point is chosen to be 100 m to the injection origin. Figure 56 demonstrates the ΔPp, $\Delta\sigma t$ and $\Delta\sigma r$ for 1000 years. Immediately after the start of injection, the changes of radial stress start to increase at the referential point, whereas for pore pressure and radial stress it takes slightly longer to increase. In this formation, pore pressure changes appear to be much higher than two other stresses. As shown in Figure 56, it takes about 100 years for stress and pore pressure changes to reach steady condition and no significant changes are observed after this.

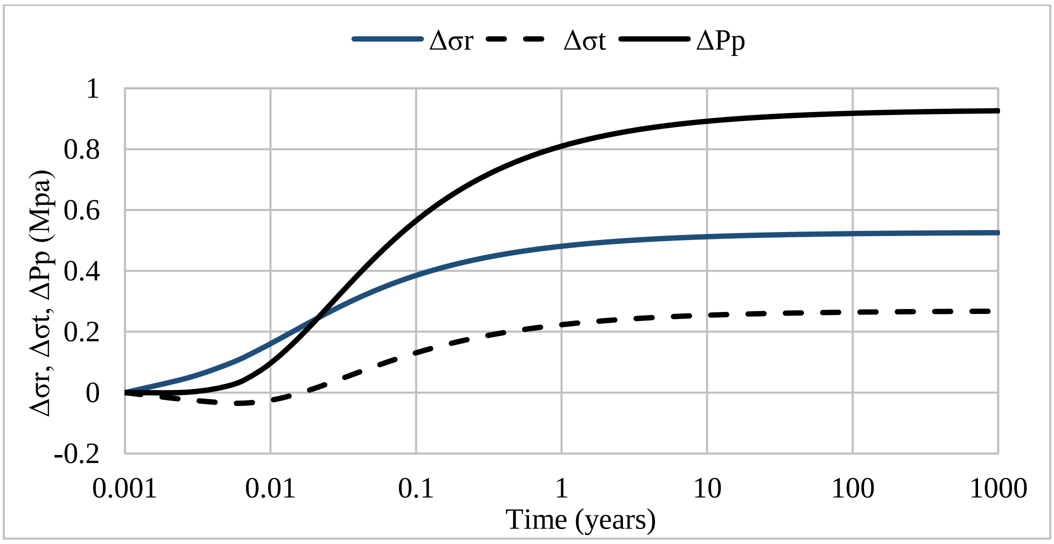

Figure 56: Fluid pressure and radial/tangential stress variation within Yalgroup formation for 1000 years after injection and 100 m from the injection origin.

The maximum ΔPp calculated in Yalgroup member is nearly 0.93 MPa (Figure 57) and radial and tangential stresses are 0.52 MPa and 0.27 MPa respectively. The values are less than those calculated for the Wonnerup member because of the difference in the rock properties and the anisotropy of the formations. Relatively, the stress state of the rocks in both members could be affected by the ΔPp. It must be considered that there is no restriction in regards to Pp diffusivity in the formations (except faults and regardless of the injection process), so Pp may change frequently as a result of injection boundary conditions. The coupling ratio was measured and is shown in Figure 58. Similar to the Wonnerup member, the pore pressure changes require more time than the other two stresses to reach the referential point. Therefore, the coupling values approach zero 1 year after injection.

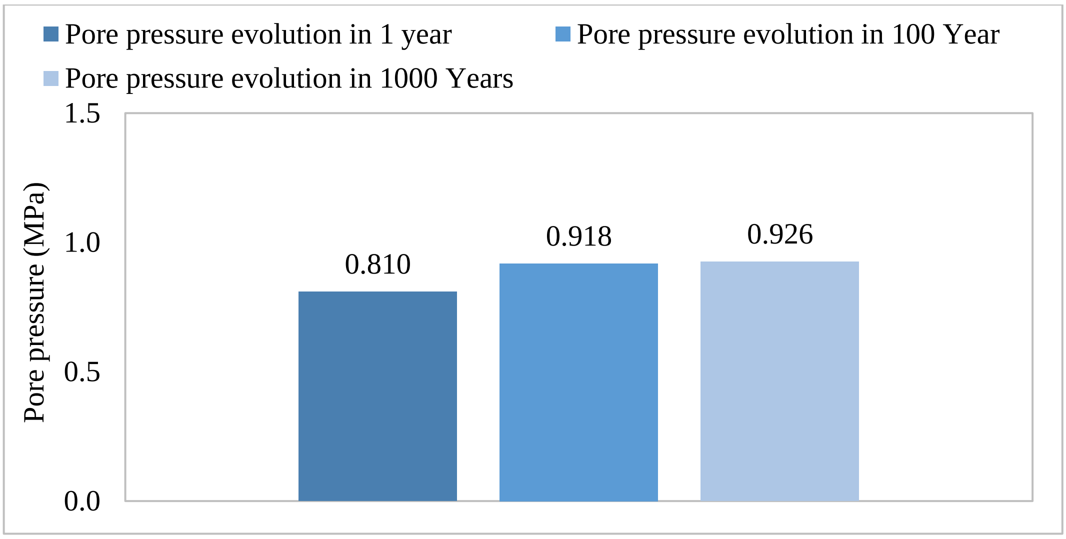

Figure 57: Pore pressure variation in 1 year, 100 years, and 1000 years within Yalgroup formation.

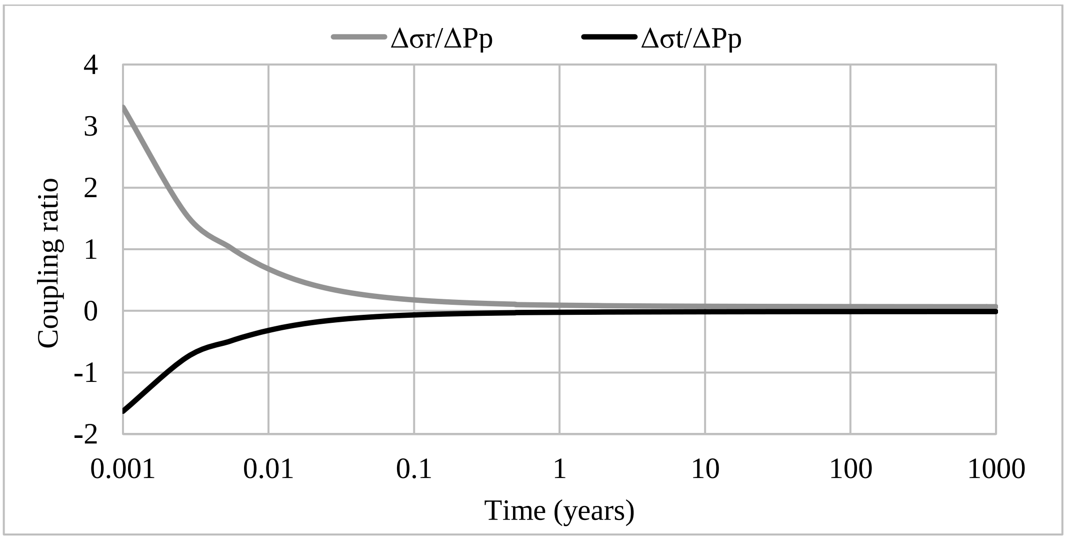

Figure 58: Coupling ratio for 1000 years after injection (Yalgroup member).

4.5.3 SWH faults reactivation analysis

The reactivation assessment of neighbouring faults within the two target reservoirs and seal is evaluated applying all the previous petrophysical and geological data from numerical analysis. Fault stability investigation is conducted analytically firstly to evaluate the structures of the most susceptible as a result of induced pore pressures during and after the carbon dioxide injection process and secondly to validate the numerical results from the previous part. The outcome of the previous part is used here to obtain a geological model and platform to precisely assess the effect of ΔPp and $\Delta\sigma$ on the stability of faults. Variation of *Pp* may affect the position of the Mohr diagram as the increase in *Pp* will shift the Mohr circle toward the failure line or reduce the effective stress. The above approach can be predicted relying on the accurate measurement of the effective stress under the influence of the coupling. Due to coupling impact maximum horizontal stress is prone to increase during injection as *Pp* increases which opens the possibility of the rocks becoming unstable.

Based on the stress map data (Table 14), the strike-slip regime ($\sigma H > \sigma v > \sigma h$) is identified in the region for fault reactivation analysis (Wonnerup reservoir). In a strike-slip type of fault, σH and σh are similarly imposed by the coupling which supports the idea that coupling has no impact on the differential stress and the Mohr diameter. As the observation point is in the σH direction, σh becomes σt and σH becomes σr the and in the event when observation point is in the σh direction, σh becomes σr *and* σH is the σt. In the following sections, the result of faults (main Western and Eastern faults) stability in both formations under two observation points of σH and σv axis will be discussed.

4.5.4 Western fault in Yalgroup member (100 m from injection source for 1000 years)

When the observation point is considered along the direction of σH, the radial stress is σH and tangential stress is σh. Additionally from the analytical approach of Rudnicki (1986), we manage to calculate the value of these stresses along with pore pressure for 1000 years. Table 18 illustrates ΔPp, $\Delta\sigma t$ and $\Delta\sigma r$ in 1000 years.

Table 18: Fluid pressure and radial/tangential stress change in 1000 years in Yalgroup formation in the orientation of σH.

Injection time	$\Delta\sigma r = \Delta\sigma H$	$\Delta\sigma\tau = \Delta\sigma h$	ΔPp
1000 Years	0.526 MPa	0.268 MPa	0.926 MPa

Carbon dioxide injection increases the *Pp* (Table 18) and causes the Mohr circle to move toward the failure envelope. *Pp* increase causes effective stress to decline and leads the Mohr circle to shift toward the failure line. As seen from the Table, in this case, the tangential stress is less than the radial. Thus, the minimum effective stress is decreasing less than the maximum one which slightly increases the size of the Mohr diameter as a result of the coupling effect. When the coupling effect is plotted and included in the analysis as of Figure 59, more effective stress and *Pp* are required to bring the fault closer to the line of failure. Therefore, the cohesionless Western fault with a friction coefficient of 0.6 is most likely to become reactivated if the observation point is the direction of σH. At least an increase of 7 MPa in pore pressure is required to observe instability in rocks which in this case is rare. This confirms little risk related to the reactivation within the Yalgroup member for the carbon dioxide injection project.

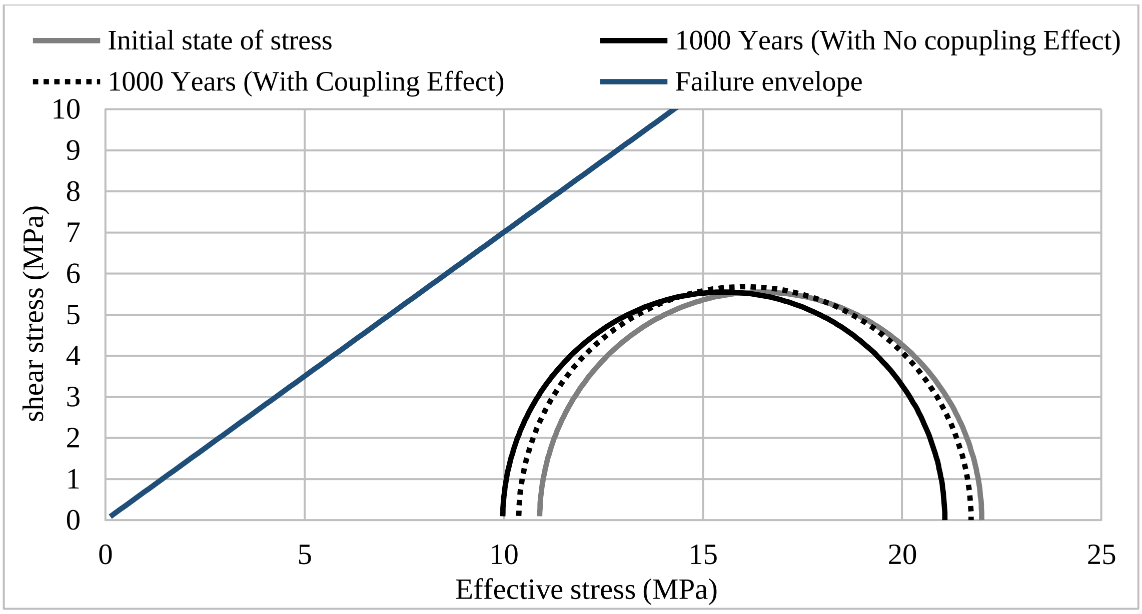

Figure 59: When the observation point is on the orientation of σH, carbon dioxide injection causes the Mohr diagram to shift toward the failure line in Yalgroup formation in the event of no coupling considered (black-solid line) and in the event coupling effect is included in the calculations (black-dashed line).

If the referential point is assumed to be in the direction of σh, the $\Delta\sigma r$ is σh and $\Delta\sigma t$ is σH. Table 19 shows $\Delta\sigma r$, $\Delta\sigma t$ *and* ΔPp after 1000 years from the injection process. Carbon dioxide injection increases the pore pressure by 0.93 MPa in 1000 years and causes the Mohr circle to shift toward the line of failure. In this circumstance, the tangential stress is more than the radial, thus, the minimum effective stress is increasing less than the maximum effective stress which slightly decreases the size of the Mohr diameter as a result of the coupling effect. As seen from Figure 60 when the coupling effect is considered in the rock stability analysis, more effective stress is required to bring the fault closer to the failure envelope. Therefore, the Western fault is least likely to become reactivated in the event that the referential point is in the direction of σh. Similar to the previous section, an almost 7.5 MPa increase in Pp is needed to detect instability in a fault. This proves a small threat of fault reactivation within the potential top seal Yalgroup member. Taking into the account poroelastic effect (coupling magnitude), the occurrence of reactivation is less feasible.

Table 19: Fluid pressure and radial/tangential stress change in 1000 years in Yalgroup formation in the orientation of σh.

Injection time	Δστ = Δσh	Δσr = ΔσH	ΔPp
1000 Years	0.526 MPa	0.268 MPa	0.926 MPa

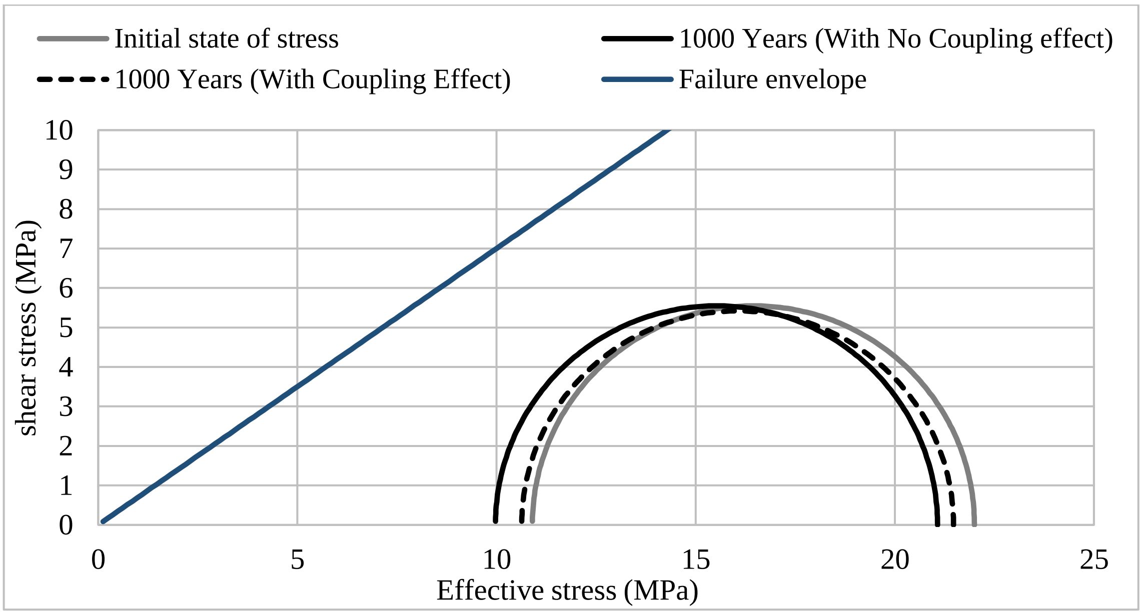

Figure 60: When the observation point is on the orientation of σh, carbon dioxide injection causes the Mohr diagram to shift toward the failure line in Yalgroup formation in the event of no coupling considered (black-solid line) and in the event coupling effect is included in the calculations (black-dashed line).

4.5.5 Eastern fault in Wonnerup member (100 m from injection source at 1000 years)

When the observation point is considered along the σH-axis, the radial stress is σH and tangential stress is σh. The location of the Eastern fault is shown in Figure 50 and the referential point (injection source) is considered to be 100 m away from the fault, so as to better analyse any possible activity within the geological formations in Wonnerup member. Additionally, from the analytical approach of Rudnicki (1986), the variation of the effective stresses along with pore pressure for 1000 years is calculated. Table 20 shows the $\Delta\sigma r$, $\Delta\sigma t$ *and* ΔPp in 1000 years.

Table 20: Fluid pressure and radial/tangential stress change in 1000 years in Wonnerup formation in the orientation of σH.

Injection time	Δσr = ΔσH	Δστ = Δσh	ΔPp
1000 years	0.87 MPa	0.45 MPa	1.51 MPa

As σH is the σr, it is increased to almost double the σr as a result of 1000 years after injection. Therefore, effective $\Delta\sigma H$ is decreasing less than the effective $\Delta\sigma H$. As shown in Figure 61, the effect of fault destabilization during carbon dioxide injection in our faulting regime is increased due to effective differential stress increases caused by coupling, if a point in the direction of σH is assumed. Moreover, when the poroelastic behaviour of the rock (coupling magnitude) is considered, more effective stress is needed to bring the fault nearer to the line of failure. Therefore, the cohesionless assumed Eastern fault with the friction coefficient of 0.6 is least likely to become reactivated when the observation point is considered to be in the direction of σh. An almost four times increase in pore pressure must be seen to observe instability in the Eastern fault. This proves a small risk of fault reactivation within the potential Wonnerup formation. Taking into account the poroelastic effect, the occurrence of reactivation is much less probable. In the case when the observation points considered to be along the σh-axis, σr is becoming σh and σt is σH. Table 21 shows the $\Delta\sigma r$, $\Delta\sigma t$ *and* ΔPp in 1000 years

Table 21: Fluid pressure and radial/tangential stress change in 1000 years in Wonnerup formation in the orientation of σh.

Injection time	Δσr = Δσh	Δστ = ΔσH	ΔPp
1000 Years	0.87 MPa	0.45 MPa	1.51 MPa

Right after the injection period an increase in the Pp occurs which reaches 1.51 MPa in 1000 years. This leads the Mohr circle to shift toward the failure line as well as a minor change in the Mohr-circle's diameter as shown in Figure 62. In this case, σt is half the amount of σr. Relatively, the minimum effective stress is changing (decreasing) more than the maximum effective stress which causes Mohr diameter to be slightly bigger as a result of poroelasticity. Moreover, when the pore pressure and stress coupling concept is included in the calculations and the rock stability analysis, more effective stress is needed to take the fault nearer to the line of failure. Therefore, the Eastern fault is less likely to become reactivated when the observation point is considered to be in the direction of σh. As previously, almost 4.5 times more pore pressure increments must be achieved to observe fault reactivation.

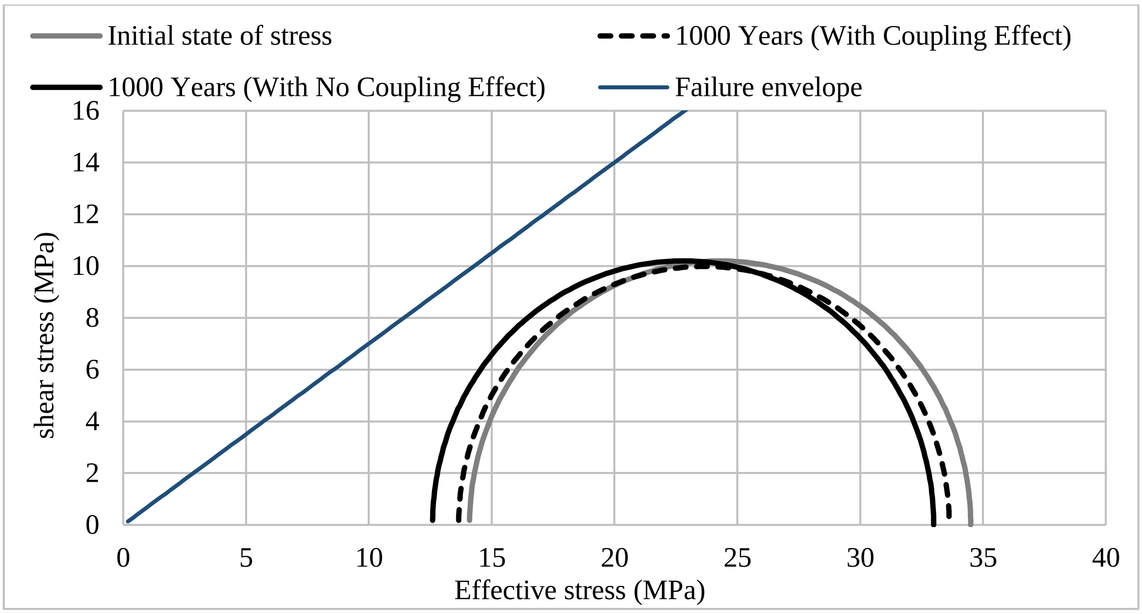

Figure 61: When the observation point is on the orientation of σH, carbon dioxide injection causes the Mohr diagram to shift toward the failure line in Wonnerup formation in the event of no coupling considered (black-solid line) and in the event coupling effect is included in the calculations (black-dashed line).

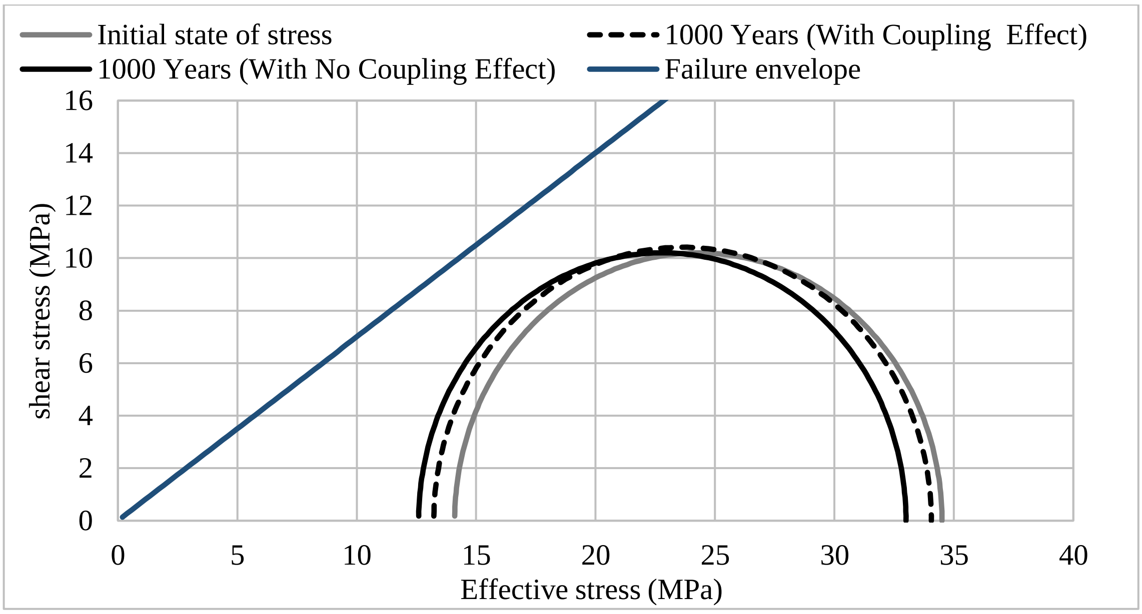

Figure 62: When the observation point is on the orientation of σh, carbon dioxide injection causes the Mohr diagram to shift toward the failure line in Wonnerup formation in the event of no coupling considered (black-solid line) and in the event coupling effect is included in the calculations (black-dashed line).

It should be stated that the cohesionless fault with 30 degrees of friction angle assumed in this analysis, is still considered more applicable compared to the measures most commonly used by geological researchers to obtain the risk analysis of the faults (cohesion of 5 MPa and friction angle of 15 degrees). If such properties are assumed, a lower risk of fault reactivation is predicted, applying uncertainties relevant to the 3D analytical and numerical modelling method that has been presented in this current work and also to the existing data. Based on the current analytical results, the current understanding of stress condition and faults and formation properties, Eastern and Western faults in either Wonnerup and the Yalgorup members are not likely to be reactivated using the injection rate shown in Table 17.

4.6 Conclusions

For the SWH, the main conclusion is that there is little risk of significant strain or failure of Wonnerup seals as a result of the Yalgorup structure being subject to the foreseen pressure alterations. To assess the worst-case conditions, two scenarios were generated to analyse the condition where any of the models would show evident yield or strain failure. Based on the modelling settings and also the information presented at the beginning of the 3D numerical study, the results show that there is a negligible impact of the planned *Pp* on the mechanical stability of both faults. This conclusion confirms that no overspread yield is observed in the vicinity of the faults – in other words, there is no indication of noteworthy fault instability or even significant deformation in the model. The results also validate previous investigation results obtained by Smith et al. (2007) and Y. Zhang, P. M. Schaubs, et al. (2015) as well as the analytical results presented in the second part of chapter 4.

It is believed the analytical 3D modelling in chapter 1 aimed to validate the results of the Bergermeer gas field in the Netherlands. The results of our investigations showed very good agreements with the numerical investigation performed by the other researchers (Hager & Toksoez, 2009; Muntendam-Bos et al., 2008; Orlic & Wassing, 2012; Orlic et al., 2013). Therefore, we have used a similar approach for the SWH carbon storage project. However, in this work analytical investigation was carried from a different perspective to provide more supporting fact. For instance, it is found that the pore pressure and stress variation are not affecting the fault stability when a higher rate of injection is proposed. Also, the location of injection points differed from numerical studies to assess how close the injection sources could be to the weaker faults. All these accomplishments as well as the estimation of the coupling ratio for a long-term carbon dioxide injection provides additional realities to the field.

Chapter 4 has reviewed the risks and protective aspects of carbon dioxide injection into the SWH area and has assessed the parameters causing fault instability. The significant finding of this chapter was to determine that there is a low risk of substantial strain within Wonnerup formation when the Yalgorup formation is subjected to the forecasted alterations in pressure. This result was obtained by applying the worst-case conditions and introducing two scenarios to better analyse the state where any of the models show apparent yield or strain failure.

Chapter 5

5. Summary

The deformation process of the stressed rocks filled with fluid (coupling) is mostly ignored in the oil and gas sector or not fully implemented into the analysis, but considering this phenomenon (the fluid pressure influence on rock deformation) is quite vital in various engineering calculations and designs. Including this physical process offers engineers the required awareness to identify the poroelastic effect for their calculation especially regarding the geological issues. Poroelasticity is a key role in different areas such as petroleum engineering and field developments applications where the real control and management of fluid injection into the ground depends on the reliable assessment of the subsidence, compaction of the upper layer of target reservoirs and ground surface, fault reactivation and wellbore instabilities. Nevertheless, poroelastic errors which can be manifested via analytical or numerical approaches are restricted due to the importance of poroelastic parameters such as Biot’s coefficient. Largely, for fault reactivation analysis, there are plenty of analytical approaches that have been industrialized with ideal assumptions such as assuming Biot’s constant of unity. Accordingly, problems with complex and inaccurate poroelastic, elastic, material properties and geometries. In reality, to solve and validate analytical issues, numerical solutions must be taken into consideration with a lower number of assumptions and complexity if possible.

This thesis focus was on the importance of the main parameters affecting reservoir geomechanics and its related environmental issues. The key purposes of my work are to investigate the pore pressure/stress coupling behaviour of the reservoir rocks and their influence on various fault regimes. Moreover, to estimate the evolution of pore pressure and stress as a result of continuous carbon dioxide injection into a poroelastic full space. We have also carried out a different set of laboratory tests to obtain the main parameters of poroelasticity associated with introducing a unique technique to verify the commercial laboratory approaches. As many parameters must be considered for the carbon sequestration process, Upscaling is very vital. For example, we almost have 40 samples from Harvey 1 well and was very difficult to find 5 similar samples which indicate the importance of upscaling. Hence, we managed to have all the elements of upscaling in this thesis such as laboratory, numerical and analytical approaches.

5.1 Concluding viewpoints

5.1.1 Analytical

The coupling magnitude varies within reservoir layers and rocks as it mainly depends on the location and time of observation. Therefore, we analytically contrived to achieve the process of this physical phenomenon and evaluate its importance on the environmental response of the target reservoir for the carbon dioxide injection process. The analytical method was based on the solution for changes of pore pressure and stresses as a result of continuous fluid injection in an infinite homogeneous poroelastic full space solved by Rudnicki (1986). For the purpose of this investigation, two case studies were chosen to evaluate the effect of carbon dioxide injection on the state of stress and pore pressure. Accordingly, the application of the fault reactivation process via applying Biot's linear poroelasticity and coupling process in full space has undergone examination for both cases. For the Bergermeer Gas field, it was found that the degree of coupling has a great influence on fault instability predictions as well as fault regimes. Note that the fault regime of this case study is found to be normal. An accurate assessment of the coupling ratio displayed that the injection point could be as close as 150 m to the Central fault and yet no reactivation occurs. This provides better understandings of the geological response of the Bergermeer gas field in the case of cushion gas injection. We also managed to measure the evolution of stress and pore pressure for a certain time (seasonal injection scenarios), taking into account the distance of the injection source. In fact, numerical analysis has been validated via analytical methods.

A similar approach has been implemented in the Harvey area, which is the target reservoir for the carbon storage project in Western Australia. The main conclusion is that there is a slight risk of noteworthy failure of both target formations of Wonnerup and Yalgroup seals due to the future alterations of pressure. Applying two scenarios to assess the worst-case scenarios, the findings showed that there is a negligible effect of the estimated pore pressure over the main faults and the other geological formations, considering that the fault regime is strike-slip, and based on the literature. We found that Biot's coefficient is one of the main principal characteristics in coupling analysis and fault instability studies. In other words, the strength of the coupling is observed to be insensitive to changes in this coefficient. Consequently, higher injection volume or stretched injection time causes failure initiation when low coupling strength is calculated. Therefore, the Biot's coefficient can be identified on retrieved samples using different laboratory settings such as the hydro-mechanical approach.

5.1.2 Numerical

In the analytical poroelastic model of Rudnicki (1986), the influence of gas injection into a poroelastic full space has been studied for both normal stress regime and strike-slip regime. To manifest the analytical investigation or validate the results, the numerical methods have been taken into account. We used Abaqus simulation software which represents fully coupled *Pp* and stress scenarios, as well as also assessing the fault instability risks of the Harvey area. Based on the proposed two scenarios and the referential points, the results illustrate a low effect of the *Pp* build-up on the faults in the region. The important outcome is no spread of yield in the fault regions is observed. We also found that Biot's coefficient is one of the principal characteristics for coupling analysis and fault instability studies. In other words, the strength of the coupling is observed to be insensitive to changes in this coefficient. Consequently, higher injection volume or stretched injection time causes failure initiation when low coupling strength is calculated. Therefore, the Biot's coefficient can be identified using different laboratory settings such as the hydro-mechanical approach.

5.1.3 Experimental

Poroelasticity is of significant importance in petroleum science and engineering as it controls many processes, from reservoir compaction to sand production and wellbore stability. Biot coefficient is the critical factor in the poroelastic formulation. With the increase in the use of XRCT in petroleum science, the opportunity to extract Biot coefficients from already existing data thus offers an important opportunity. Relatively, the effective stress model is very important to address and predict poroelastic rock performance. The key parameter in this approach is Biot's constant, for forecasting pore pressure and stress evolution within the geological structure. We have carried out various testing arrangements to precisely compute this valuable coefficient. We also have tried some of the commercial techniques presented in the industry, which end up as failures. Zero deformation or hydro-mechanical tests were performed on 5 Gosford samples. The Biot's coefficients for all samples were inside the range of matching samples with similar petrophysical properties. The Zero-deformation test has its ups and downs. The main advantage of the test is that it only needs a one-step procedure, and the drawback is that the maintenance of zero volumetric conditions requires very precise and permanent supervision. The second test we carried out was the acoustic test on cubic samples using TTSC cells. This test has rarely been carried out in the industry and still requires extra validation and work. But the findings showed very close-matching results compared to similar tests on cylindrical samples.

To simplify the complex experimental works, we have presented an innovative procedure with which Biot's coefficient can be calculated via X-ray Micro-CT. We also have validated the results with conventional tests. The micro-Ct test allowed us to calculate the coefficient in three orthogonal directions.

5.2 Future investigation's notions

The followings are the key recommendation for the 3D modelling of our work:

- Evaluate the pore pressure impact on the orientation of stress near existing faults, which could affect the movement of fluid within porous medium and reservoir layers.
- Include the chemical interaction between the fault and reservoir formation with the injecting fluid.

In regards to the laboratory work, due to the time limits and the very time-consuming process of our tests, we were unable to perform laboratory validation on Harvey specimens. It is recommended that further samples be tested to deliver a broad understanding of the reservoir simulation and response to coupling issues. We have performed further analysis of the technique on a sand pack. It is, however, noted that our XRCT driven Biot coefficient works based on the principle of solid contact. The grain contacts of extremely low permeability rocks such as mudrocks cannot be differentiated from XRCT analysis as previously pointed out in the thesis. Besides, using nano-scale CT scanning will have limitations both in terms of the pores they can resolve, as well as the challenge in defining a REV for comparison with large-scale experiments.

References

Aadnøy, B., & Looyeh, R. (2011). Chapter 7 - Porous Rocks and Effective Stresses. In B. Aadnøy & R. Looyeh (Eds.), *Petroleum Rock Mechanics* (pp. 77-105). Gulf Professional Publishing. https://doi.org/https://doi.org/10.1016/B978-0-12-385546-6.00007-3

Addis, M. A. (1997, 1997/1/1/). *The Stress-Depletion Response Of Reservoirs* https://doi.org/10.2118/38720-MS

Addis, M. A., Choi, X., & Gunning, J. (1998, 1998/1/1/). *The Influence Of The Reservoir Stress-Depletion Response On The Lifetime Considerations Of Well Completion Design* https://doi.org/10.2118/47289-MS

Ahmed, S., Müller, T., Madadi, M., & Calo, V. (2018). Drained pore modulus determination using digital rock technology. *ASEG Extended Abstracts, 2018*, 1. https://doi.org/10.1071/ASEG2018abP055

Ahmed, S., Müller, T. M., Liang, J., Tang, G., & Madadi, M. (2017). Macroscopic Deformation Moduli of Porous Rocks: Insights from Digital Image Pore-Scale Simulations. In *Poromechanics VI* (pp. 815-821). https://doi.org/doi:10.1061/9780784480779.101

Ahmed, Z., & Lebedev, M. (2019). Elastic properties of sands, Part 2: Implementation of contact-based model to determine the elasticity of the grains from ultrasonic measurements. *Geophysical Prospecting*, *67*(4), 745-760. https://doi.org/10.1111/1365-2478.12743

Altmann, J. B. (2010). *Poroelastic effects in reservoir modelling* Karlsruhe Institute of Technology].

Altmann, J. B., Müller, B. I. R., Müller, T. M., Heidbach, O., Tingay, M. R. P., & Weißhardt, A. (2014). Pore pressure stress coupling in 3D and consequences for reservoir stress states and fault reactivation. *Geothermics*, *52*, 195-205. https://doi.org/http://dx.doi.org/10.1016/j.geothermics.2014.01.004

Amadei, B. (2013). *Rock stress and its measurement*. Springer.

Arns, C. H., Knackstedt, M. A., Pinczewski, W. V., & Garboczi, E. J. (2002). Computation of linear elastic properties from microtomographic images: Methodology and agreement between theory and experiment. *GEOPHYSICS*, *67*(5), 1396-1405. https://doi.org/10.1190/1.1512785

Atefi Monfared, K. (2015). *Geomechanics of Fluid Injection in Geological Reservoirs* [Doctor of Philosophy, University of Waterloo]. http://hdl.handle.net/10012/9608

Barla, G. (1972). Rock Anisotropy. In L. Müller (Ed.), *Rock Mechanics* (pp. 131-169). Springer Vienna. https://doi.org/10.1007/978-3-7091-4109-0_8

Bell, M. L., & Nur, A. (1978). Strength changes due to reservoir-induced pore pressure and stresses and application to Lake Oroville. *Journal of Geophysical Research: Solid Earth*, *83*(B9), 4469-4483. https://doi.org/10.1029/JB083iB09p04469

Berentsen, C., de Pater, C., & Nieuwland, F. (2019). Geomechanical Model of a Gas Field for Seismic Risk Analysis.SPE Europec featured at 81st EAGE Conference and Exhibition,

Biot, M. A. (1941). General Theory of Three-Dimensional Consolidation. *Journal of Applied Physics*, *12*(2), 155-164. https://doi.org/doi:http://dx.doi.org/10.1063/1.1712886

Biot, M. A. (1954). Theory of stress-strain relations in anisotropic viscoelasticity and relaxation phenomena. *Journal of Applied Physics*, *25*(11), 1385-1391. https://doi.org/10.1063/1.1721573

Biot, M. A. (1962). Mechanics of Deformation and Acoustic Propagation in Porous Media. *Journal of Applied Physics*, *33*(4), 1482-1498. https://doi.org/doi:http://dx.doi.org/10.1063/1.1728759

Biot, M. A., & Willis, D. G. (1957). The Elastic Coefficients of the Theory of Consolidation. *Journal of Applied Mechanics*, *24*, 594-601. https://doi.org/citeulike-article-id:9228504

Blöcher, G., Reinsch, T., Hassanzadegan, A., Milsch, H., & Zimmermann, G. (2014). Direct and indirect laboratory measurements of poroelastic properties of two consolidated sandstones. *International Journal of Rock Mechanics and Mining Sciences*, *67*(Supplement C), 191-201. https://doi.org/https://doi.org/10.1016/j.ijrmms.2013.08.033

Booker, J. R., & Randolph, M. F. (1984). Consolidation of a cross-anisotropic soil medium. *The Quarterly Journal of Mechanics and Applied Mathematics*, *37*(3), 479-495. https://doi.org/10.1093/qjmam/37.3.479

Borges, J. A. R., Pires, L. F. R., Cássaro, F. A. M., Roque, W. L., Heck, R. J., Rosa, J. A., & Wolf, F. G. (2018). X-ray microtomography analysis of representative elementary volume (REV) of soil morphological and geometrical properties. *Soil & Tillage Research*, *182*, 112-122.

Cao, Z., Deng, J., Zhou, S., & He, Y. (2020). Research on the feasibility of compressed carbon dioxide energy storage system with underground sequestration in antiquated mine goaf. *Energy Conversion and Management*, *211*, 112788. https://doi.org/https://doi.org/10.1016/j.enconman.2020.112788

Chen, Q., & Nur, A. (1992). Pore fluid pressure effects in anisotropic rocks: Mechanisms of induced seismicity and weak faults. *pure and applied geophysics*, *139*(3-4), 463-479. https://doi.org/10.1007/BF00879947

Chen, Z., Lyons, S., & Qin, G. (2004). *The mechanical behavior of a poroelastic medium saturated with a newtonian fluid* (Vol. 1).

Cheng, A. H. D., Abousleiman, Y., & Roegiers, J. C. (1993). Review of some poroelastic effects in rock mechanics. *International Journal of Rock Mechanics and Mining Sciences & Geomechanics Abstracts*, *30*(7), 1119-1126. https://doi.org/https://doi.org/10.1016/0148-9062(93)90081-N

Christensen, N. I., & Wang, H. F. (1985). The Influence of pore pressure and confining pressure on dynamic elastic properties of Berea sandstone. *GEOPHYSICS*, *50*(2), 207-213. https://doi.org/10.1190/1.1441910

de Pater, C. J., Berentsen, C., & Martens, H. (2020). Compaction Seismicity: What Determines Seismic vs. Non-Seismic Behavior in Dutch Gas Fields?SPE Europec,

Delle Piane, C., Bourdet, J., Dautriat, J., & Esteban, L., et al.,. (2017). *The Lesueur: Deposition, Rocks, Facies, Propertie*.

Delle Piane, C., Olierook, H. K. H., Timms, N. E., Saeedi, A., Esteban, L., Rezaee, R., Mikhaltsevitch, V., & Lebedev, M. (2013). *Facies-based rock properties distribution along the Harvey 1 stratigraphic well.*

Detournay, E., & Alexander, H.-D. C. (1993). *Fundamentals of Poroelasticity* (Vol. 2). Pergamon Press.

Detournay, E., & Cheng, A. H. D. (1988). Poroelastic response of a borehole in a non-hydrostatic stress field. *International Journal of Rock Mechanics and Mining Sciences & Geomechanics Abstracts*, *25*(3), 171-182. https://doi.org/https://doi.org/10.1016/0148-9062(88)92299-1

Engelder, T., & Fischer, M. P. (1994). Influence of poroelastic behavior on the magnitude of minimum horizontal stress, Sh in overpressured parts of sedimentary basins. *Geology*, *22*(10), 949-952. https://doi.org/10.1130/0091-7613(1994)022<0949:iopbot>2.3.co;2

Fjær, E., Holt, R. M., Horsrud, P., Raaen, A. M., & Risnes, R. (2008). Chapter 12 Reservoir geomechanics. In R. M. H. P. H. A. M. R. E. Fjær & R. Risnes (Eds.), *Developments in Petroleum Science* (Vol. Volume 53, pp. 391-433). Elsevier. https://doi.org/http://dx.doi.org/10.1016/S0376-7361(07)53012-8

Foulger, G. R., Wilson, M. P., Gluyas, J. G., Julian, B. R., & Davies, R. J. (2018). Global review of human-induced earthquakes. *Earth-Science Reviews*, *178*, 438-514. https://doi.org/https://doi.org/10.1016/j.earscirev.2017.07.008

Franquet, J. A., & Abass, H. H. (1999, 1999/1/1/). *Experimental evaluation of Biot's poroelastic parameterThree different methods*

Fronteau, G., Thomachot-Schneider, C., Chopin, E., Barbin, V., Mouze, D., & Pascal, A. (2010). Black-crust growth and interaction with underlying limestone microfacies. *Geological Society, London, Special Publications*, *333*, 25-34. https://doi.org/10.1144/SP333.3

Geertsma, J. (1957). The Effect of Fluid Pressure Decline on Volumetric Changes of Porous Rocks.

Geertsma, J. (1966, 1966/1/1/). *Problems of Rock Mechanics In Petroleum Production Engineering*

Glubokovskikh, S., Gurevich, B., Lebedev, M., Mikhaltsevitch, V., & Tan, S. (2015). Effect of asperities on stress dependency of elastic properties of cracked rocks. *International Journal of Engineering Science*, *98*. https://doi.org/10.1016/j.ijengsci.2015.09.001

Gonzalez, O., & Stuart, A. M. (2008). *A first course in continuum mechanics*. Cambridge University Press.

Goulty, N. R. (2003). Reservoir stress path during depletion of Norwegian chalk oilfields. *Petroleum Geoscience*, *9*(3), 233-241. https://doi.org/10.1144/1354-079302-545

Grigoli, F., Cesca, S., Rinaldi, A. P., Manconi, A., López-Comino, J. A., Clinton, J. F., Westaway, R., Cauzzi, C., Dahm, T., & Wiemer, S. (2018). The November 2017 M_w 5.5 Pohang earthquake: A possible case of induced seismicity in South Korea. *Science*, *360*(6392), 1003-1006. https://doi.org/10.1126/science.aat2010

Hager, B. H., & Toksoez, M. N. (2009). *Technical Review of Bergermeer Seismicity Study TNO Report 2008-U-R1071/B*. MIT, Cambridge, MA (United States); Department of Earth, Atmospheric and Planetary Sciences, Massachusetts Institute of Technology MIT, Cambridge, MA 02139 (United States).

Haimson, B. C. (1975). Deep in-situ stress measurements by hydrofracturing. *Tectonophysics, 29*(1–4), 41-47. https://doi.org/http://dx.doi.org/10.1016/0040-1951(75)90131-6

Han, G., & Dusseault, M. B. (2003). Description of fluid flow around a wellbore with stress-dependent porosity and permeability. *Journal of Petroleum Science and Engineering, 40*(1), 1-16. https://doi.org/https://doi.org/10.1016/S0920-4105(03)00047-0

Hawkes, C. D., McLellan, P. J., Zimmer, U., & Bachu, S. (2004, 2004/1/1/). *Geomechanical Factors Affecting Geological Storage Of Co2 In Depleted Oil And Gas Reservoirs: Risks And Mechanisms* Gulf Rocks 2004, the 6th North America Rock Mechanics Symposium (NARMS), Houston, Texas. https://doi.org/

He, J., Rui, Z., & Ling, K. (2016). A new method to determine Biot's coefficients of Bakken samples. *Journal of Natural Gas Science and Engineering, 35*, 259-264. https://doi.org/https://doi.org/10.1016/j.jngse.2016.08.061

Hillis, R. (2000). Pore pressure/stress coupling and its implications for seismicity. *Exploration Geophysics, 31*(2), 448-454. https://doi.org/http://dx.doi.org/10.1071/EG00448

Hilterman, F. (1970). Three-Dimensional Seismic Modeling. *Geophysics, 35*(6), 1020-1037.

Hoek, E., & Brown, E. T. (2019). The Hoek–Brown failure criterion and GSI – 2018 edition. *Journal of Rock Mechanics and Geotechnical Engineering, 11*(3), 445-463. https://doi.org/https://doi.org/10.1016/j.jrmge.2018.08.001

Holzapfel, G. A. (2002). Nonlinear solid mechanics: a continuum approach for engineering science. *Meccanica, 37*(4), 489-490.

Huang, Y., Wang, X., & Schuster, G. T. (2014, 2014/10/29/). *Non-Local Means Filter for Trim Statics* 2014 SEG Annual Meeting, Denver, Colorado, USA. https://doi.org/https://doi.org/10.1190/segam2014-0352.1

Iglauer, S., Sarmadivaleh, M., Geng, C., & Lebedev, M. (2014, 2014/1/19/). *In-situ Residual Oil Saturation And Cluster Size Distribution In Sandstones After Surfactant Flooding Imaged With X-ray Micro-computed Tomography* International Petroleum Technology Conference, Doha, Qatar. https://doi.org/10.2523/IPTC-17312-MS

Ingraham, M. D., Bauer, S. J., Issen, K. A., & Dewers, T. A. (2017). Evolution of permeability and Biot coefficient at high mean stresses in high porosity sandstone. *International Journal of Rock Mechanics and Mining Sciences, 96*, 1-10. https://doi.org/https://doi.org/10.1016/j.ijrmms.2017.04.004

Josh, M., Esteban, L., Delle Piane, C., Sarout, J., Dewhurst, D. N., & Clennell, M. B. (2012). Laboratory characterisation of shale properties. *Journal of Petroleum Science and Engineering, 88–89*, 107-124. https://doi.org/http://dx.doi.org/10.1016/j.petrol.2012.01.023

Kaliakin, V. N. (2017). Chapter 10 - Example Problems Related to Shear Strength of Soils. In V. N. Kaliakin (Ed.), *Soil Mechanics* (pp. 419-439). Butterworth-Heinemann. https://doi.org/https://doi.org/10.1016/B978-0-12-804491-9.00010-0

Keehm, Y., Mukerji, T., & Nur, A. (2001). Computational rock physics at the pore scale: Transport properties and diagenesis in realistic pore geometries. *The Leading Edge, 20*(2), 180-183. https://doi.org/10.1190/1.1438904

Kim, K.-H., Ree, J.-H., Kim, Y., Kim, S., Kang, S. Y., & Seo, W. (2018). Assessing whether the 2017 M_w 5.4 Pohang earthquake in South Korea was an induced event. *Science, 360*(6392), 1007-1009. https://doi.org/10.1126/science.aat6081

Klein, E., Baud, P., Reuschlé, T., & Wong, T. f. (2001). Mechanical behaviour and failure mode of bentheim sandstone under triaxial compression. *Physics and Chemistry of the Earth, Part A: Solid Earth and Geodesy, 26*(1), 21-25. https://doi.org/https://doi.org/10.1016/S1464-1895(01)00017-5

Knackstedt, M. A., Latham, S., Madadi, M., Sheppard, A., Varslot, T., & Arns, C. (2009). Digital rock physics: 3D imaging of core material and correlations to acoustic and flow properties. *The Leading Edge, 28*(1), 28-33. https://doi.org/10.1190/1.3064143

Kraaijpoel, D., Nieuwland, D., & Dost, B. (2013). *Microseismic Monitoring and Subseismic Fault Detection in an Underground Gas Storage*. https://doi.org/10.3997/2214-4609.20142354

Kümpel, H.-J. (1991). Poroelasticity: parameters reviewed. *Geophysical Journal International, 105*(3), 783-799. https://doi.org/10.1111/j.1365-246X.1991.tb00813.x

Labuz, J. F., & Zang, A. (2012). Mohr–Coulomb Failure Criterion [journal article]. *Rock Mechanics and Rock Engineering, 45*(6), 975-979. Labuz2012. https://doi.org/10.1007/s00603-012-0281-7

Langhi, L., Zhang, Y., Ciftci, B., Delle Piane, C., Strand, J., Dewhurst, D., Stalker, L., & Michael, K. (2015). Preliminary Analysis of Containment Integrity for Geological Storage of CO2 at the South West Hub Project, Western Australia. https://doi.org/https://doi.org/10.3997/2214-4609.201414052

Laurent, J., Bouteca, M. J., Sarda, J.-P., & Bary, D. (1993). Pore-Pressure Influence in the Poroelastic Behavior of Rocks: Experimental Studies and Results. https://doi.org/10.2118/20922-PA

Lebedev, M., Zhang, Y., Mikhaltsevitch, V., Inglauer, S., & Rahman, T. (2017). Residual Trapping of Supercritical CO2: Direct Pore-scale Observation Using a Low Cost Pressure Cell for Micro Computer Tomography. *Energy Procedia*, *114*, 4967-4974. https://doi.org/https://doi.org/10.1016/j.egypro.2017.03.1639

Ling, K., He, J., Pei, P., Wang, S., & Ni, X. (2016, 2016/6/26/). *Comparisons of Biot's Coefficients of Bakken Core Samples Measured by Three Methods* 50th U.S. Rock Mechanics/Geomechanics Symposium, Houston, Texas. https://doi.org/

Ljunggren, C., Chang, Y., Janson, T., & Christiansson, R. (2003). An overview of rock stress measurement methods. *International Journal of Rock Mechanics and Mining Sciences*, *40*(7), 975-989. https://doi.org/https://doi.org/10.1016/j.ijrmms.2003.07.003

Mcnamee, J., & Gibson, R. E. (1960). PLANE STRAIN AND AXIALLY SYMMETRIC PROBLEMS OF THE CONSOLIDATION OF A SEMI-INFINITE CLAY STRATUM. *The Quarterly Journal of Mechanics and Applied Mathematics*, *13*(2), 210-227. https://doi.org/10.1093/qjmam/13.2.210

Mikhaltsevitch, V., Lebedev, M., & Gurevich, B. (2014). *A Laboratory Study of Elastic and Anelastic Properties of Savonnieres Limestone*. https://doi.org/10.3997/2214-4609.20141302

Mukunoki, T., Miyata, Y., Mikami, K., & Shiota, E. (2016). X-ray CT analysis of pore structure in sand. *Solid Earth Discussions*, 1-36. https://doi.org/10.5194/se-2016-16

Muntendam-Bos, M. D. A. G., Wassing, M. D. B. B. T., Geel, D. C. R., Louh, I. M., & Thienen-Visser, M. D. K. v. (2008). *Bergermeer Seismicity Study* (034.82130).

Nermoen, A., Korsnes, R., Christensen, H. F., Trads, N., Hiorth, A., & Madland, M. V. (2013, 2013/1/1/). *Measuring the Biot Stress Coefficient and is Implications on the Effective Stress Estimate* 47th U.S. Rock Mechanics/Geomechanics Symposium, San Francisco, California.

Nourifard, N., Pervukhina, M., Urosevic, M., & Lebedev, M. (2020). The effects of stress and fluid on the anisotropy of reservoir rock: case study of a sandstone from the harvey 3 CCS site, Western Australia. *Exploration Geophysics*, 1-12. https://doi.org/10.1080/08123985.2019.1704363

Nur, A., & D. Byerlee, J. (1971). *An Exact Effective Stress Law for Elastic Deformation of Rock with Fluids* (Vol. 76). https://doi.org/10.1029/JB076i026p06414

ODIN. (2016). *Dynamic Modelling of CO2 Sequestration in the Harvey Area – A Report by ODIN Reservoir Consultants for Department of Mines and Petroleum*.

Omdal, E., Madland, M. V., H, B., E, N., Korsnes, R., Hiorth, A., & G, K. (2009). *Experimental Investigation of the Effective Stress Coefficient For Various High Porosity Outcrop Chalks*.

Orlic, B., & Wassing, B. B. T. (2012, 2012/1/1/). *Modeling Stress Development And Fault Slip In Producing Hydrocarbon Reservoirs Overlain By Rock Salt Caprocks*

Orlic, B., Wassing, B. B. T., & Geel, C. R. (2013, 2013/1/1/). *Field Scale Geomechanical Modeling for Prediction of Fault Stability During Underground Gas Storage Operations in a Depleted Gas Field in the Netherlands*

Peksa, A. E., Wolf, K.-H. A. A., & Zitha, P. L. J. (2015). Bentheimer sandstone revisited for experimental purposes. *Marine and Petroleum Geology*, *67*, 701-719. https://doi.org/https://doi.org/10.1016/j.marpetgeo.2015.06.001

Pervukhina, M., Esteban, L., Müller, T., Zhang, Y., & Schaubs, P. (2017). *The Lesueur, SWH: Advanced well log analysis, constraints for the stress field and geomechanical modelling of CO2 injection*.

Prasad, M., & Manghnani, M. H. (1997). Effects of pore and differential pressure on compressional wave velocity and quality factor in Berea and Michigan sandstones. *GEOPHYSICS*, *62*(4), 1163-1176. https://doi.org/10.1190/1.1444217

Qiao, L. P., Wong, R. C. K., Aguilera, R., & Kantzas, A. (2012). Determination of Biot's Effective-Stress Coefficient for Permeability of Nikanassin Sandstone. https://doi.org/10.2118/150820-PA

Rasouli, V., Pervukhina, M., Müller, T. M., & Pevzner, R. (2013). In-situ stresses in the Southern Perth Basin at the GSWA Harvey-1 well site. *Exploration Geophysics*, *44*(4), 289-298. https://doi.org/https://doi.org/10.1071/EG13046

RezaGholilou, A., Salemi, H., Tarom, N., Behnoudfar, P., & Sarmadivaleh, M. (2019). Experimental investigation of fluid thermal effects on fracture brittleness. *The APPEA Journal*, *59*(1), 457-463. https://doi.org/https://doi.org/10.1071/AJ18269

Rice, J. R., & Cleary, M. P. (1976). Some basic stress diffusion solutions for fluid-saturated elastic porous media with compressible constituents. *Reviews of Geophysics*, *14*(2), 227-241. https://doi.org/10.1029/RG014i002p00227

Risnes, R., Bratli, R. K., & Horsrud, P. (1982). Sand Stresses Around a Wellbore. *Society of Petroleum Engineers Journal*, *22*(06), 883-898. https://doi.org/10.2118/9650-PA

Roever, K. (1951, 1951/1/1/). *Laboratory Studies of Transient Elastic Waves* Proceedings of the ThirdWorld Petroleum Congress, 537–545, in D. A. Ebrom, and J. A. McDonald, eds., 1994, Seismic Physical Modeling: SEG, 103–111.,

Roshan, H., Masoumi, H., & Hagan, P. C. (2016, 2016/6/26/). *On Size-Dependent Uniaxial Compressive Strength of Sedimentary Rocks in Reservoir Geomechanics* 50th U.S. Rock Mechanics/Geomechanics Symposium, Houston, Texas. https://doi.org/

Roshan, H., & Rahman, S. S. (2011). A Fully Coupled Chemo-Poroelastic Analysis of Pore Pressure and Stress Distribution around a Wellbore in Water Active Rocks [journal article]. *Rock Mechanics and Rock Engineering*, *44*(2), 199-210. Roshan2011. https://doi.org/10.1007/s00603-010-0104-7

Rudnicki, J. W. (1986). Fluid mass sources and point forces in linear elastic diffusive solids. *Mechanics of Materials*, *5*(4), 383-393. https://doi.org/http://dx.doi.org/10.1016/0167-6636(86)90042-6

Ruistuen, H., Teufel, L. W., & Rhett, D. (1999). Influence of Reservoir Stress Path on Deformation and Permeability of Weakly Cemented Sandstone Reservoirs. https://doi.org/10.2118/56989-PA

Rutqvist, J., Rinaldi, A. P., Cappa, F., Jeanne, P., Mazzoldi, A., Urpi, L., Guglielmi, Y., & Vilarrasa, V. (2016). Fault activation and induced seismicity in geological carbon storage – Lessons learned from recent modeling studies. *Journal of Rock Mechanics and Geotechnical Engineering*, *8*(6), 789-804. https://doi.org/https://doi.org/10.1016/j.jrmge.2016.09.001

Salemi, H., Iglauer, S., Rezagholilou, A., & Sarmadivaleh, M. (2018). Laboratory measurement of Biot’s coefficient and pore pressure influence on poroelastic rock behaviour. *The APPEA Journal*, *58*(1), 182-189. https://doi.org/https://doi.org/10.1071/AJ17069

Salemi, H., Nourifard, N., Iglauer, S., & Sarmadivaleh, M. (2020). Acoustic Approach to Determine Biot Effective Stress Coefficient of Sandstone Using True Triaxial Cell (TTSC).54th U.S. Rock Mechanics/Geomechanics Symposium,

Salemi, H., Rezagholilou, A., Asadi, S., Iglauer, S., & Sarmadivaleh, M. (2017, 2017/8/28/). *Poroelastic Effects of Pore Pressure-Stress Coupling on Fault Reactivation Risks During Gas Injection* 51st U.S. Rock Mechanics/Geomechanics Symposium, San Francisco, California, USA. https://doi.org/

Scholz, C. H. (2019). *The Mechanics of Earthquakes and Faulting* (3 ed.). Cambridge University Press. https://doi.org/DOI: 10.1017/9781316681473

Schön, J. H. (2011). Chapter 7 - Geomechanical Properties. In J. H. Schön (Ed.), *Handbook of Petroleum Exploration and Production* (Vol. 8, pp. 245-271). Elsevier. https://doi.org/https://doi.org/10.1016/S1567-8032(11)08007-4

Segall, P. (1989). Earthquakes triggered by fluid extraction. *Geology*, *17*(10), 942-946. https://doi.org/10.1130/0091-7613(1989)017<0942:etbfe>2.3.co;2

Sharma, S., Van Gent, D., Burke, M., & Stelfox, L. (2017). The Australian South West Hub Project: Developing a Storage Project in Unconventional Geology. *Energy Procedia*, *114*, 4524-4536. https://doi.org/https://doi.org/10.1016/j.egypro.2017.03.1569

Siggins, A. F., Dewhurst, D. N., & Tingate, P. R. (2001, 2001/1/1/). *Stress Path, Pore Pressure and Microstructural Influences on Q in Carnarvon Basin Sandstones* https://doi.org/10.4043/13043-MS

Skempton, A. W. (1961). Effective Stress in Soils, Concrete and Rocks. In *SELECTED PAPERS ON SOIL MECHANICS* (pp. 106-118). https://doi.org/10.1680/sposm.02050.0014

Smith, T., Rana, R. S., Missiaen, P., Rose, K. D., Sahni, A., Singh, H., & Singh, L. (2007). High bat (*Chiroptera*) diversity in the Early Eocene of India. *Naturwissenschaften*, *94*, 1003-1009. https://doi.org/10.1007/s00114-007-0280-9

Soltanzadeh, H., & Hawkes, C. D. (2008). Semi-analytical models for stress change and fault reactivation induced by reservoir production and injection. *Journal of Petroleum Science and Engineering*, *60*(2), 71-85. https://doi.org/https://doi.org/10.1016/j.petrol.2007.05.006

Streit, J. E., & Hillis, R. R. (2004). Estimating fault stability and sustainable fluid pressures for underground storage of CO2 in porous rock. *Energy*, *29*(9), 1445-1456. https://doi.org/https://doi.org/10.1016/j.energy.2004.03.078

Suckale, J. (2009). Chapter 2 - Induced Seismicity in Hydrocarbon Fields. In *Advances in Geophysics* (Vol. 51, pp. 55-106). Elsevier. https://doi.org/https://doi.org/10.1016/S0065-2687(09)05107-3

Tarn, J.-Q., & Lu, C.-C. (1991). Analysis of subsidence due to a point sink in an anisotropic porous elastic half space. *International Journal for Numerical and Analytical Methods in Geomechanics*, *15*(8), 573-592. https://doi.org/10.1002/nag.1610150805

Teatini, P., Ferronato, M., Franceschini, A., Frigo, M., Janna, C., Zoccarato, C., & Isotton, G. (2019). Gas Storage in Compartmentalized Reservoirs: A Numerical Investigation on Possible “Unexpected” Fault Activation.53rd U.S. Rock Mechanics/Geomechanics Symposium,

Terzaghi, K. (1923). The Invention of Soil Mechanics. In (pp. 71-83). https://doi.org/doi:10.1061/9780784403648.ch06

Terzaghi, K. (1943). *Theoretical soil mechanics*. J. Wiley and Sons, Inc.; Chapman and Hall, Limited.

Teufel, L. W., Rhett, D. W., & Farrell, H. E. (1991, 1991/1/1/). *Effect of Reservoir Depletion And Pore Pressure Drawdown On In Situ Stress And Deformation In the Ekofisk Field, North Sea* The 32nd U.S. Symposium on Rock Mechanics (USRMS), Norman, Oklahoma. https://doi.org/

Timms, N., Corbel, S., Olierook, H., Wilkes, P., Delle Piane, Claudio; Sheldon, Heather; Alix, Remi; Horowitz, Frank; Wilson, Moyra; Evans, Katy A.; Griffiths, Cedric; Stutenbecker, Laura; Israni, Shankar; Hamilton, Joseph; Esteban, Lionel; Cope, Patricia; Evans, Cody; Pimienta, Lucas; Dyt, Chris; Huang, Xiu; Hopkins, & J; Champion, D. (2012). *Perth Basin Assessment Program*.

Todd, T., & Simmons, G. (1972). Effect of pore pressure on the velocity of compressional waves in low-porosity rocks. *Journal of Geophysical Research*, *77*(20), 3731-3743. https://doi.org/10.1029/JB077i020p03731

Toksöz, P. B. H. H. a. P. M. N. (2009). TECHNICAL REVIEW OF BERGERMEER SEISMICITY STUDY. *Department of Earth, Atmospheric and Planetary Sciences*.

Urosevic, M., Langhi, L., Ricard, L., Strand, J., Yavuz, S., Ziramov, S., Tertyshnikov, K., Pevzner, R., Bona, A., Lebedev, M., Shulakova, V., Pervukhina, M., Kiewiet, M. C. D. N., Sarmadivaleh, M., & Salemi, H. (2019). *Potential for preferential flow through faults and fractures*. *ANLEC R&D, Issue. Curtin University*.

van Dalen, K. N., Ghose, R., Drijkoningen, G. G., & Smeulders, D. M. J. (2010). In-situ permeability from integrated poroelastic reflection coefficients. *Geophysical Research Letters*, *37*(12). https://doi.org/10.1029/2010gl043319

Wang, D., Noguchi, T., & Nozaki, T. (2019). Increasing efficiency of carbon dioxide sequestration through high temperature carbonation of cement-based materials. *Journal of Cleaner Production*, *238*, 117980. https://doi.org/https://doi.org/10.1016/j.jclepro.2019.117980

Wang, H. (2000). *Theory of Linear Poroelasticity with Applications to Geomechanics and Hydrogeology*. Princeton University Press. https://books.google.com.au/books?id=RauGOzaQBRUC

Winkler, K. W., & Nur, A. (1982). Seismic attenuation; effects of pore fluids and frictional sliding. *Geophysics*, *47*(1), 2-16.

Yalaev, T. R., Bayuk, I. O., Tarelko, N. F., & Abashkin, V. V. (2016, 2016/6/26/). *Connection of Elastic and Thermal Properties of Bentheimer Sandstone Using Effective Medium Theory (Rock Physics)* 50th U.S. Rock Mechanics/Geomechanics Symposium, Houston, Texas.

Yin, S., Dusseault, M. B., & Rothenburg, L. (2009). Multiphase poroelastic modeling in semi-space for deformable reservoirs. *Journal of Petroleum Science and Engineering*, *64*(1), 45-54. https://doi.org/https://doi.org/10.1016/j.petrol.2008.12.003

Yu, H.-S. (2000). Underground Excavations and Tunnelling. In *Cavity Expansion Methods in Geomechanics* (pp. 309-359). Springer Netherlands. https://doi.org/10.1007/978-94-015-9596-4_10

Zhang, Y., Langhi, L., Schaubs, P., Delle Piane, C., Dewhurst, D., Stalker, L., & Michael, K. (2015). Geomechanical stability of CO 2 containment at the South West Hub Western Australia: A coupled geomechanical–fluid flow modelling approach. *International Journal of Greenhouse Gas Control*, *37*, 12-23.

Zhang, Y., Langhi, L., Schaubs, P. M., Piane, C. D., Dewhurst, D. N., Stalker, L., & Michael, K. (2015). Geomechanical stability of CO2 containment at the South West Hub Western Australia: A coupled geomechanical–fluid flow modelling approach. *International Journal of Greenhouse Gas Control*, *37*, 12-23. https://doi.org/https://doi.org/10.1016/j.ijggc.2015.03.003

Zhang, Y., Lebedev, M., Al-Yaseri, A., Yu, H., Nwidee, L. N., Sarmadivaleh, M., Barifcani, A., & Iglauer, S. (2018). Morphological evaluation of heterogeneous oolitic limestone under pressure and fluid flow using X-ray microtomography. *Journal of Applied Geophysics*, *150*, 172-181. https://doi.org/https://doi.org/10.1016/j.jappgeo.2018.01.026

Zhang, Y., Schaubs, P. M., Langhi, L., Delle Piane, C., Dewhurst, D. N., Stalker, L., & Michael, K. (2015). Geomechanical Evaluation of Fault Reactivation Potential and Uplift at the South West Hub Geological CO2 Storage Site, Western Australia.49th U.S. Rock Mechanics/Geomechanics Symposium,

Zhang, Y., Zhang, Z., Sarmadivaleh, M., Lebedev, M., Barifcani, A., & Iglauer, S. (2017, 2017/8/28/). *Prediction of Microscale Rock Mechanical Performance From microCT*

Images: Heterogeneous Coal as an Example 51st U.S. Rock Mechanics/Geomechanics Symposium, San Francisco, California, USA.

Zoback, M. D. (2010). *Reservoir Geomechanics*. Cambridge University Press. https://books.google.com.au/books?id=Xx63OaM2JIIC

Zoback, M. D., & Gorelick, S. M. (2012). Earthquake triggering and large-scale geologic storage of carbon dioxide. *Proc Natl Acad Sci U S A, 109*(26), 10164-10168. https://doi.org/10.1073/pnas.1202473109

Zoback, M. D., & Zinke, J. C. (2002). Production-induced Normal Faulting in the Valhall and Ekofisk Oil Fields. In C. I. Trifu (Ed.), *The Mechanism of Induced Seismicity* (pp. 403-420). Birkhäuser Basel. https://doi.org/10.1007/978-3-0348-8179-1_17

Appendix A

Publications from this thesis

- Salemi, Hossein., Rezagholilou, Alireza., Asadi, Sadeq., Iglauer, Stefan., and Sarmadivaleh, Mohammad., "*Poroelastic Effects of Pore Pressure-Stress Coupling on Fault Reactivation Risks During Gas Injection".*

  Paper presented at the 51st U.S. Rock Mechanics/Geomechanics Symposium, San Francisco, California, USA, June 2017.

- Salemi, Hossein., Iglauer, Stefan., Rezagholilou, Alireza., Sarmadivaleh, Mohammad., "*Laboratory measurement of Biot's coefficient and pore pressure influence on poroelastic rock behaviour*".

  The APPEA Journal 58(1) 182-189-2018 https://doi.org/10.1071/AJ17069

- Salemi, Hossein., Iglauer, Stefan., Nourifard, Nazanin., Sarmadivaleh, Mohammad., "*Acoustic Approach to Determine Biot Effective Stress Coefficient of Sandstone Using True Triaxial Cell (TTSC)*".

  Paper presented at the 54th U.S. Rock Mechanics/Geomechanics Symposium, physical event cancelled, June 2020. Paper Number: ARMA-2020-1048

Appendix B

Copyright permissions and attribution statements

1) The APPEA Journal 58(1) 182-189 https://doi.org/10.1071/AJ17069

CSIRO PUBLISHING **Licence to Publish** APPEA Limited

The APPEA Journal **Manuscript No.** AJ17069.R2

Title of the paper/presentation (the 'Work') Laboratory measurement of Biot constant and pore pressure influence on poroelastic rock behaviour/Peer-reviewed Paper

Author(s) Hossein Salemi, Stefan Iglauer, Ali Rezagholilou, Mohammad Sarmadivaleh

The APPEA Journal includes papers submitted to and presented at APPEA Conferences. The purpose of this Licence to Publish is to grant and confirm the grant of exclusive rights to publish the Work in the APPEA Journal.

The APPEA Journal is published by CSIRO Publishing for the Australian Petroleum Production and Exploration Association Limited (APPEA). APPEA Conference papers are made available to delegates to the APPEA Conference and included in the APPEA Journal. The APPEA Journal is a digital, online journal which is sold to subscribers and others.

By submitting this paper, the Author (Authors if a multi-authored paper) represents that they have the right or have obtained authorisation to enter into this Licence and grant the rights granted or contemplated by it.

The Author warrants that:

- Other than as a presentation at an APPEA Conference, the Work (including any abstract) has not been published before.
- The Work is not presently being considered for publication elsewhere.
- The Work does not violate any intellectual property right of any person or entity.
- The Work does not contain any subject matter that contravenes any laws (including defamatory material and misleading and deceptive material.
- The Work meets ethical standards applicable to the research discipline.
- The Work indicates any financial or non-financial interests/relationships that may be interpreted to have influenced the manuscript.
- All Authors have made a significant contribution to the Work and agree to its submission, and
- Permission for any tables or figures or other third party materials included in the Work that have been published elsewhere has been received from the relevant copyright holder and is attributed in the Work.

Terms of the Licence to Publish

1. In consideration for publication of the Work (and without derogating from rights granted in submitting the Work for the Conference), the Author grants to APPEA, through CSIRO Publishing (the 'Publisher'), an exclusive, royalty free, worldwide licence including the right to sub-license, to:
   - Reproduce, publish and communicate the Work, or any part of the Work, to the public in any and all media, whether existing before or after the date of this Licence, for commercial, educational and all other purposes for the full remaining term of the copyright subsisting in the Work in each applicable jurisdiction.
   - Approve fair and reasonable permission requests from third parties to reuse material contained in the Work for the purpose of study, research or subsidiary publication.

   The Author acknowledges that the Publisher is licensed by APPEA to publish and sell the APPEA Journal.

2. In addition to the Author's moral rights in respect of the Work, and subject to third party rights, the Author retains the right to:
   - Use copies of the Work for non-commercial purposes within his/her institution subject to the usual copyright licensing agency arrangements
   - Use the Work for further research and presentations at meetings and conferences
   - Use the illustrations (line art, photographs, figures, plates) and research data in his/her own future works
   - Include the Work in part or in full in a thesis provided it is not published for commercial gain
   - Place his/her pre-publication version of the Work on a pre-print server
   - Place his/her pre-publication version of the Work on a personal website or institutional repository on condition that there is a link to the definitive version on the APPEA Journal site hosted on the Publisher's website.

3. The Author agrees to:
   - Include a link and/or reference to the Work as published by the Publisher on all further uses of the Work or parts of the Work
   - Not reproduce or authorise others to reproduce adaptations of the Work that are substantially identical to the Work for any commercial publication
   - Not permit digital copies of the Work as published by the Publisher to be systematically networked to external users
   - Not use the Work in any way that implies that the Publisher, APPEA, the Journal or the Editors endorse any product or procedure described in the Work.

4. When exercising any of the rights assigned or granted, each party is required to give sufficient acknowledgement of the contribution made by the other party to the published material including a citation to the APPEA Journal.

Works made in the course of employment

5. Where the Work has been made by the Author (or in the case of multiple Authors, by any of them) in the course of employment and their employer owns copyright in the Work, that employer must sign this Licence. The employer has the same rights and obligations and gives the same warranties and licence rights as an Author under this Licence.

2) *American Rock Mechanics Association-ARMA (two publications)*

From: Peter Smeallie <peterhsmeallie@gmail.com>
Sent: Thursday, 25 March 2021 9:20 PM

To: Hossein Salemi <hossein.salemi@postgrad.curtin.edu.au>
Subject: RE: New Message (sent by contact form at American Rock Mechanics Association)

Dear Hossein,

You have **ARMA's permission** to use information from your papers as described below with proper attribution.

Best,

Peter

Peter Smeallie

Executive Director
American Rock Mechanics Association
600 Woodland Terrace
Alexandria, VA 22302
703-683-1808 (office)
703-801-1088 (cell)
www.armarocks.org

From: hossein.salemi@postgrad.curtin.edu.au
Sent: Thursday, March 25, 2021 4:58 AM
To: info@armarocks.org
Subject: New Message (sent by contact form at American Rock Mechanics Association)

Name: Hossein Salemi
Email: hossein.salemi@postgrad.curtin.edu.au
Topic: ARMA symposium
Subject: Copyright of my own work
Message: Dear Peter,

I have two papers published in one Petro through ARMA, I am having a problem getting the copy right permission. Is there any chance you could help?
The papers title:
Poroelastic Effects of Pore Pressure-Stress Coupling on Fault Reactivation Risks During Gas Injection,
Paper Number: ARMA-2017-0356
Acoustic Approach to Determine Biot Effective Stress Coefficient of Sandstone Using True Triaxial Cell,
Paper Number: ARMA-2020-1048

Regards
Hossein Salemi

3) Attribution Statement

Laboratory measurement of Biot’s coefficient and pore pressure influence on poroelastic rock behaviour (APPEA)						
	conception and design	acquisition of data & method	data conditioning & manipulation	analysis & statistical method	interpretation & discussion	Final Approval
Hossein Salemi	X	X	X	X	X	
I acknowledge that these represent my contribution to the above research output.						
Signed.						
Prof. Stefan Iglauer					X	X
I acknowledge that these represent my contribution to the above research output.						
Signed.						
Dr. Alireza Rezagholilou		X	X			X
I acknowledge that these represent my contribution to the above research output.						
Signed.						
Dr. Mohammad Sarmadivaleh	X		X	X	X	X
I acknowledge that these represent my contribution to the above research output.						
Signed.						

Acoustic approach to determine Biot effective stress coefficient of sandstone using true triaxial cell (TTSC) (ARMA 2020)						
	conception and design	acquisition of data & method	data conditioning & manipulation	analysis & statistical method	interpretation & discussion	Final Approval
Hossein Salemi	X	X	X	X	X	
I acknowledge that these represent my contribution to the above research output.						
Signed.						
Prof. Stefan Iglauer			X		X	X
I acknowledge that these represent my contribution to the above research output.						
Signed.						
Dr. Nazanin Nourifard		X	X	X		
I acknowledge that these represent my contribution to the above research output.						
Signed.						
Dr. Mohammad Sarmadivaleh	X		X	X	X	X
I acknowledge that these represent my contribution to the above research output.						
Signed.						

Poroelastic effects of pore pressure-stress coupling on fault reactivation risks during gas injection (ARMA 2017)						
	conception and design	acquisition of data & method	data conditioning & manipulation	analysis & statistical method	interpretation & discussion	Final Approval
Hossein Salemi	X	X	X	X	X	
I acknowledge that these represent my contribution to the above research output.						
Signed.						
Prof. Stefan Iglauer					X	X
I acknowledge that these represent my contribution to the above research output.						
Signed.						
Dr. Alireza Rezagholilou	X	X	X			X
I acknowledge that these represent my contribution to the above research output.						
Signed.						
Dr. Sadeq Asadi	X		X			X
I acknowledge that these represent my contribution to the above research output.						
Signed.						
Dr. Mohammad Sarmadivaleh	X		X	X	X	X
I acknowledge that these represent my contribution to the above research output.						
Signed.						